The influence of remanence and flux trapping on the magnetic shielding properties of mu-metals and superconductors

Tymen Golüke

Research group: EMS
Supervisors:
Prof. dr. ir. H.J.M. ter Brake
Dr. M.M.J Dhallé

Contents

1 Introduction

In this assignment the performance is studied of magnetic shields made from a combination of two materials, a high-μ metal called CryoPerm and the superconductor Nb. These shields are needed to create a low magnetic field environment for the proper functioning of detectors whose performance depends on magnetic field. The shields are usually designed with the aid of numerical models. However, in the design of high-performance shields the effect of remanence is of particular interest for both high μ metal and superconductors, since it can lead to field contributions that are difficult to model. This assignment will be done in two parts. First an experimental validation of finite element and analytical models of relatively complex shield structures is made, especially looking at the effect of remanence compared to the model results. Second, we attempt to set up a model that describes flux trapping in a superconductor while cooling through its transition temperature.

This assignment is carried out in collaboration with the Space Research Organisation Netherlands (SRON) in the frame of the Principle Investigator Preparatory Programme (PPIP) "*Magnetic shielding of TES sensors for Athena/XMS and SPICA/Safari*". For these missions SRON will be using Transition Edge Sensors (TES), for the X-ray spectrometer mounted in the ESA-led space-based Advanced Telescope for High Energy Astrophysics [http://sci.esa.int/ixo/43937instruments] as well as in the far infrared instrument SAFARI to be launched in the JAXA-led SPICA mission [http://www.ir.isas.jaxa.-jp/SPICA/SPICA_HP/index_English.html]. TES detectors are versatile micro-calorimeters that use the resistive transition between the superconducting and normal state to sense the heat deposited by a photon. For this, they require low DC- and AC background magnetic fields (typically <1μT) because these may cause broadening of the transition or instability [1].

The shield assembly proposed by SRON for ESA-Athena mission is shown in Figure 1.1. The validation of this assembly was the direct motivation for this study.

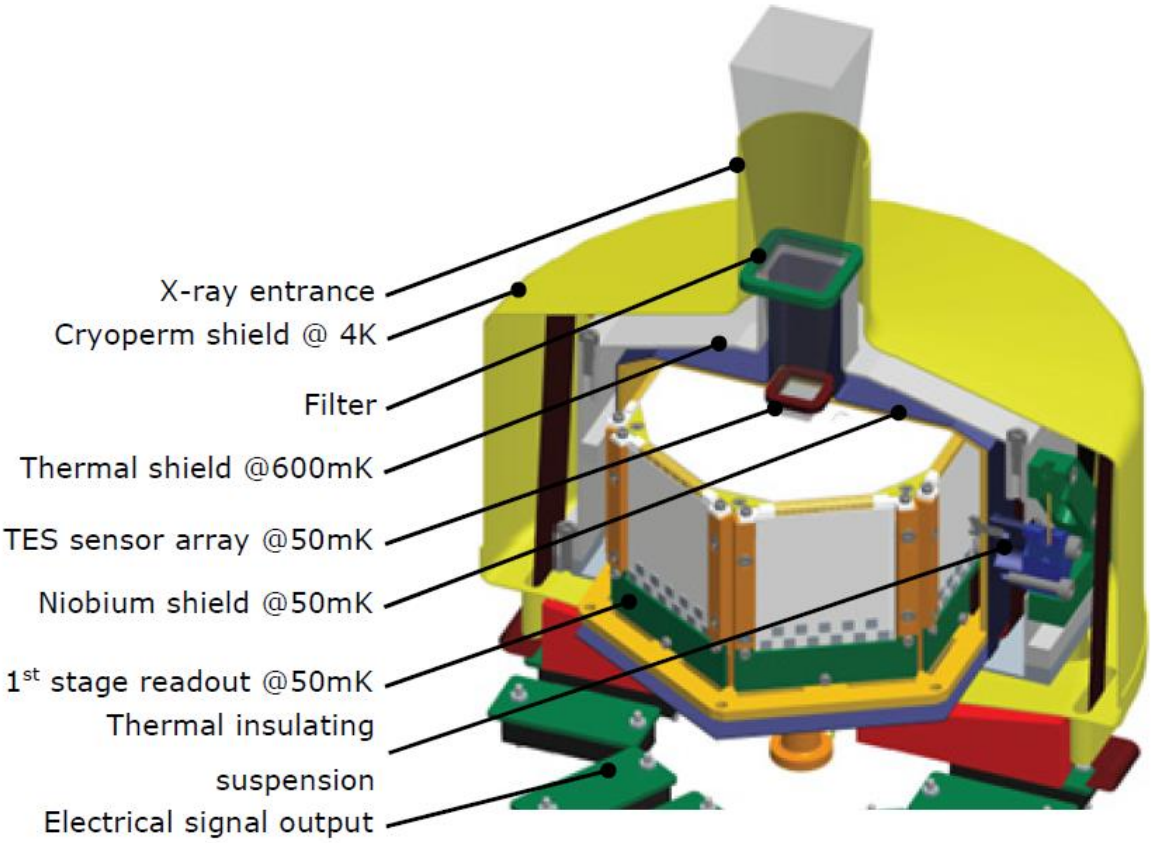

Figure 1.1 Proposed shield assembly for the RES in the Athena mission, with an inner Nb shield surrounded by a CryoPerm one

In general magnetic shielding can be done in 3 ways. The first one is active shielding. Here the background field is measured by a detector and cancelled out with a set of coils. This method is useful for earth-based applications (e.g. SQUID-based medical systems) but it is too bulky and too heavy for use in satellites. The second method is a μ metal shield, made from a material with a high permeability. The magnetization currents of such material force magnetic field lines towards the perpendicular direction outside and towards the parallel direction inside an interface with a low-μ region of space [2]. This means that it kind of "absorbs" the magnetic field lines around it (Figure 1.2a) [3]. The basic principles of μ metal shields are further explained in paragraph 1.1. The third method is a superconducting shield. In the Meissner state, a superconducting material allows no magnetic field inside, so it has a permeability of zero (Figure 1.2b). The basic principles of superconducting shielding are further explained in paragraph 1.2.

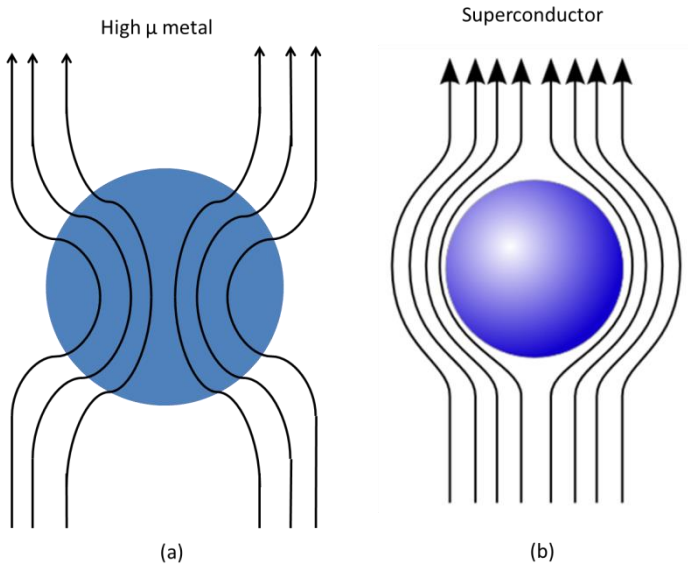

Figure 1.2 illustration permeability effect, black line magnetic field, (a) high μ metal, (b) superconductor (source picture: http://en.wikipedia.org/wiki/Meissner_effect)

1.1 μ metal shield

1.1.1 Maxwell equations

To further explain μ metals, we start from the Maxwell equations. The equations needed are the relation between magnetic induction **B** and current density **J** (Ampère's law equation (1a)) as well as the relation between electric field **E** and magnetic field **B** (Faraday's law equation (1b)). Both equations are in an electrostatic system that means that no alternating electric field is present.

$$\mu_0 \boldsymbol{J} = \nabla \times \boldsymbol{B} \tag{1a}$$

$$\nabla \times \boldsymbol{E} = -\frac{d\boldsymbol{B}}{dt} \tag{1b}$$

Second, the magnetic induction **B** needs to be described in different parameters: the vector potential **A** (equation (2)) and a combination of the field **H** and the magnetization **M** (equation (3)).

$$\boldsymbol{B} = \nabla \times \mathbf{A} \tag{2}$$

$$\boldsymbol{B} = \mu_0(\boldsymbol{H} + \boldsymbol{M}) \tag{3}$$

Equation (3) can be interpreted in terms of microscopic magnetic dipole moments. These dipoles are facing random directions. If a sufficiently strong magnetic field **H** is imposed on a high-μ the material the dipoles will line up in the direction of the magnetic field and stay in that direction even when the magnetic field is turned off (Figure 1.3). The average dipole density is called the magnetization **M** of the material. The remaining magnetization once the field is turned off is called remanence $\mathbf{M}_1$.

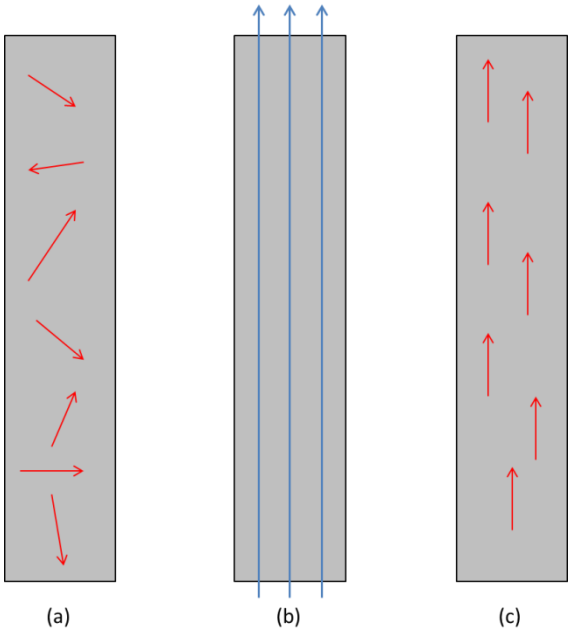

Figure 1.3 magnetization of a high μ metal, the red arrows represent the small dipoles, the blue arrows represent the applied magnetic field, a) net zero magnetization, b) magnetic field H applied, c) magnetization in direction of applied field with no field present caused by remanence

Suppose a uniformly magnetized block which has magnetization $\mathbf{M}_r$ in absence of an externally applied field **H**. Combining this information with equations (1a) and equation (3) an expression for **J** in terms of $\mathbf{M}_r$ can be found.

$$\mu_0 \boldsymbol{J} = \nabla \times \boldsymbol{B} = \mu_0 \nabla \times (\boldsymbol{H} + \boldsymbol{M}_r) = \mu_0 \nabla \times \boldsymbol{M}_r \rightarrow \boldsymbol{J} = \nabla \times \boldsymbol{M}_r \qquad (4)$$

This can then be rewritten using Stokes's theorem to:

$$\boldsymbol{K} = \boldsymbol{M} \times \hat{n} \qquad (5)$$

Here **K** is a surface current. That means that each of the microscopic dipoles described before can be seen as a rotating current around the dipole. If the dipole density is uniform, the magnetization of the block can then be seen as a current over its surface (Figure 1.4).

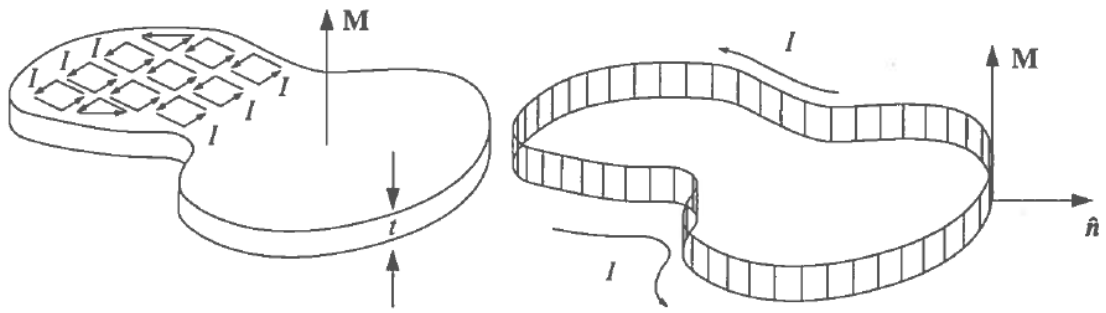

Figure 1.4 magnetization depicted as current over the surface (source: D.J.Griffiths, introduction to electrodynamics, third edition)

1.1.2 High-μ metal basic theory

A consequence of a high permeability is that the material has effectively no magnetic induction parallel to its surface ($B_{\parallel} \approx 0$ just outside the surface).

To explain this an example is used: an interface between a μ-metal and air is taken. This interface is at z=0 with z>0 being μ-metal and z<0 being air (Figure 1.5). To simplify things the problem is taken to be 2D with the x axis parallel to the interface and the z axis perpendicular.

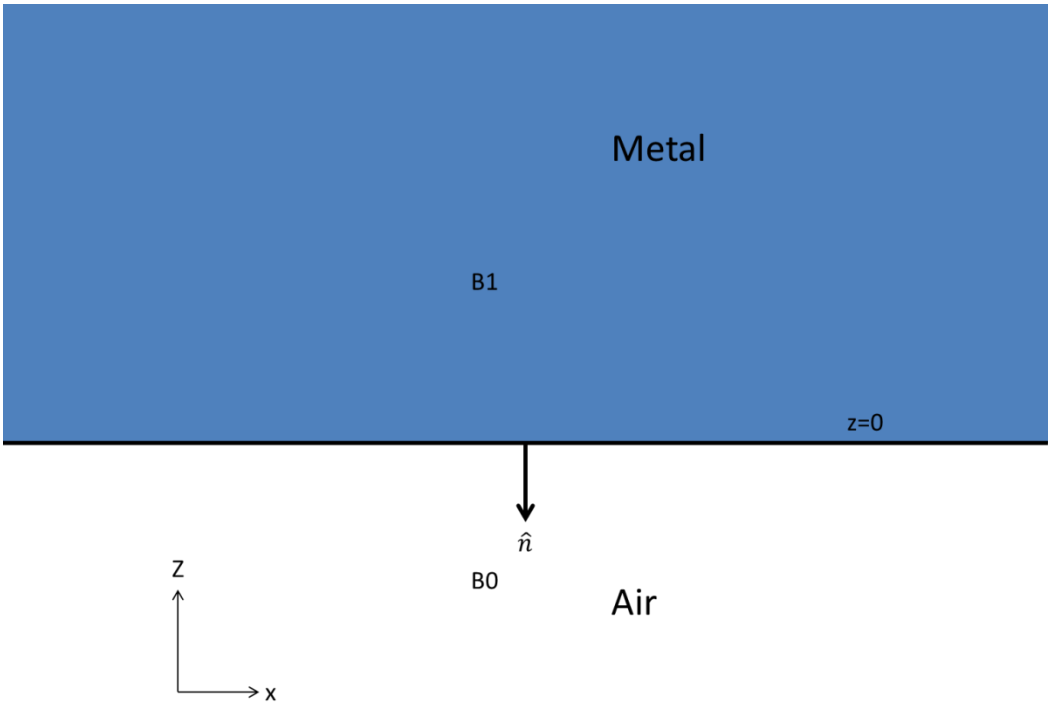

Figure 1.5 interface between a μ metal and air

To solve this example equation (6.27) from [2] is used.

$$\boldsymbol{B}^{\parallel}_{above} - \boldsymbol{B}^{\parallel}_{below} = \mu_0(\boldsymbol{K} \times \hat{n}) \tag{6}$$

For this formula the surface current **K** needs to be known, which was previously determined to be dependent on the magnetization **M**:

$$\boldsymbol{K} = \boldsymbol{M} \times \hat{n} \tag{5}$$

In this 2D system **M** and **B** have only x and z components and only the μ-metal can be magnetized.

$$\boldsymbol{B} = B_x\hat{x} + B_z\hat{z}, \qquad \boldsymbol{M} = M_x\hat{x} + M_z\hat{z} \tag{7}$$

This is then used to solve the equations with the normal in the –z direction:

$$\boldsymbol{K} = \boldsymbol{M} \times \hat{n} = (M_x\hat{x} + M_z\hat{z}) \times -\hat{z} = M_x\hat{y}$$

$$\boldsymbol{B}^{\parallel}_{above} - \boldsymbol{B}^{\parallel}_{below} = \mu_0(\boldsymbol{K} \times \hat{n}) = \mu_0(M_x\hat{y} \times -\hat{z}) = -\mu_0 M_x\hat{x} \tag{8}$$

Now an expression for M as a function of B is needed. For that equation (3) is used in combination with the relation between the magnetic field **B** and the field **H**.

$$\boldsymbol{B} = \mu_1\boldsymbol{H} \rightarrow H = \frac{B_x}{\mu_1}\hat{x} + \frac{B_z}{\mu_1}\hat{z}$$

$$\boldsymbol{B} = \mu_0(\boldsymbol{H} + \boldsymbol{M}) \rightarrow \boldsymbol{M} = \frac{\boldsymbol{B}}{\mu_0} - \boldsymbol{H} \tag{9}$$

Here μ_1 is the permeability. To solve this the values need to be implemented of for the magnetic field inside the μ-metal:

$$\boldsymbol{M} = \frac{B_{1x}}{\mu_0}\hat{x} + \frac{B_{1z}}{\mu_0}\hat{z} - \left(\frac{B_{1x}}{\mu_1}\hat{x} + \frac{B_{1z}}{\mu_1}\hat{z}\right) = \left(\frac{B_{1x}}{\mu_0} - \frac{B_{1x}}{\mu_1}\right)\hat{x} + \left(\frac{B_{1z}}{\mu_0} - \frac{B_{1z}}{\mu_1}\right)\hat{z}$$
$$= B_{1x}\frac{\mu_1 - \mu_0}{\mu_0\mu_1}\hat{x} + B_{1z}\frac{\mu_1 - \mu_0}{\mu_0\mu_1}\hat{z} \qquad (10)$$

Now this is used to solve equation (6) with the parallel field in the x-direction.

$$\boldsymbol{B}^{\parallel}_{above} - \boldsymbol{B}^{\parallel}_{below} = -\mu_0 M_x \hat{x}$$

$$\rightarrow B_{0x}\hat{x} - B_{1x}\hat{x} = -\mu_0 B_{1x}\frac{\mu_1 - \mu_0}{\mu_0\mu_1}\hat{x} = B_{1x}\frac{\mu_0 - \mu_1}{\mu_1}\hat{x} = B_{1x}\left(\frac{\mu_0}{\mu_1} - 1\right)\hat{x}$$

$$\rightarrow B_{0x}\hat{x} = B_{1x}\frac{\mu_0}{\mu_1} \qquad (11)$$

From this, it is concluded that how higher the permeability (μ_1) how lower the parallel component of the magnetic field close to the surface. So with very high permeability, the parallel component near the surface is almost zero ($B_{\parallel} \approx 0$ just outside the surface). In chapter 2, we will see how this requirement forms the basis for straight forward modelling high-μ metal shields.

Another property of a high-μ metal is the hysteresis relation between the magnetization **M** inside the material and the external applied field **H** (Figure 1.6) [3]. This hysteresis is a consequence of the remanence shown in Figure 1.3. If a material is taken which initially has no magnetization and a field is applied its dipoles will start aligning in the direction of the field which in turn causes a net magnetization **M**. Now lets increase the field until a maximum magnetization M_s is reached. M_s is the saturation magnetization, reached when all dipoles point in the direction of the external field. When in this situation the field is turned off, most of the dipoles will stay aligned leading to the remanence M_r. As the external field is made more negative, more and more dipoles will switch orientation until the net magnetization becomes zero at H=-H_c, the negative coercivity. Increasing the negative field further eventually flips all dipoles and M becomes –M_s. Reducing the amplitude of H from negative to zero leads again to M=-M_r. This process thus creates a loop centered around M=0, H=0 but never reaching its original initial state again (Figure 1.6).

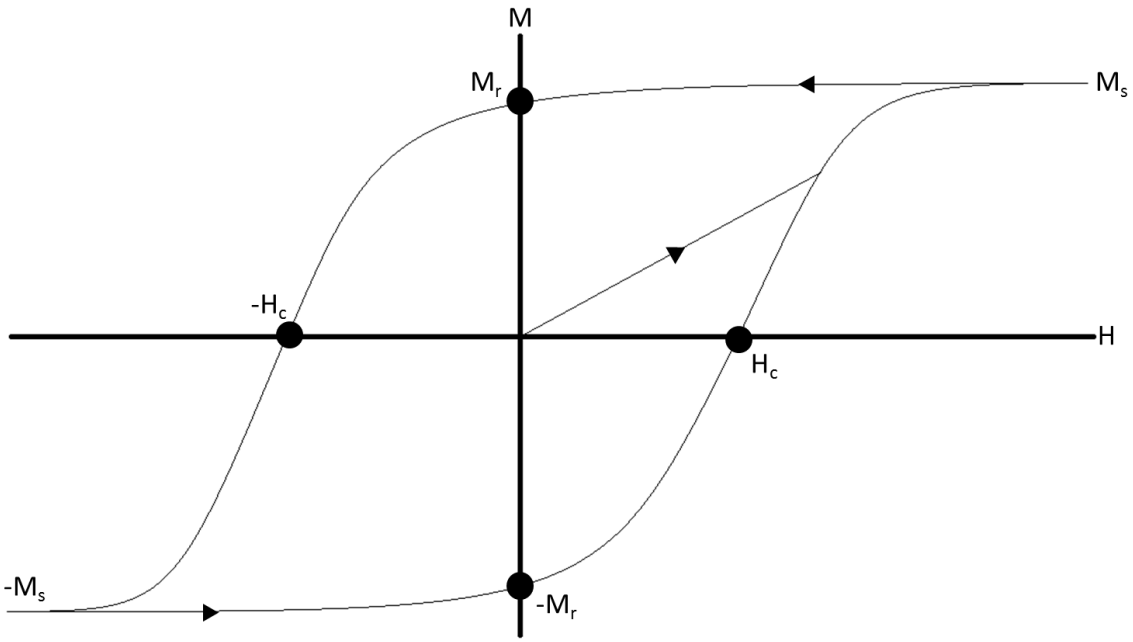

Figure 1.6 hysteresis curve for magnetization M over field H of a high-μ metal

The hysteresis curve and especially the remanent magnetization will be an important issue in this assignment, since M_r may cause a magnetic field as described in equation (3). This may cause a magnetic field to be "frozen in" in a shield made of high-μ metal.

1.1.3 AC effects

Another effect relevant to this assignment is the presence of eddy currents. These are induced when an AC magnetic field is applied to a material. Faraday's law (equation (1b)) states that a changing magnetic field B will cause an electric field E. This electric field will give rise to a current I, which in turn generates a magnetic field B. Because of the minus sign in Faraday's law (equation (1b)) this induced magnetic field will be in the opposite direction of the applied magnetic field (Figure 1.7).

These eddy currents only penetrate a certain distance into the material, the so-called skin depth. This skin depth depends on material and on the frequency of the applied magnetic field.

The eddy currents cause a phase shift in the measured magnetic field (compared to the applied field), since the induced magnetic field 90^0 is out of phase with the applied one. It is also important to mention that when a low enough frequency is reached, the eddy currents become negligeable.

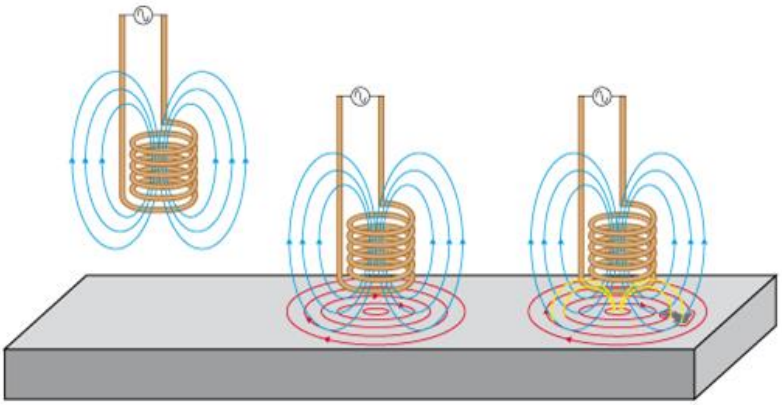

Figure 1.7 illustration of eddy currents being produced by a AC magnetic field inside a material, material grey, applied magnetic field blue, eddy currents red, counter magnetic field produced by eddy currents yellow, (source picture: http://www.olympus-ims.com/en/ndt-tutorials/eca-tutorial/what-is-eca/basic/)

1.1.4 Demagnetization procedure

As discussed in paragraph 1.1.2, magnetic remanence may cause problems with high-μ shields so a way has to be found to remove the remanence. For this, a so-called demagnetization procedure may be used. This is done by applying an AC field and then slowly bringing its amplitude down to zero. Two conditions need to be met to successfully remove the remanence. First a low enough frequency must be chosen so that no effect of eddy currents is present. This is to make sure that the field penetrates throughout the thickness of the shield. Secondly, a high enough initial field amplitude must be chosen so that the field fully saturates the hysteresis curve from Figure 1.6. The demagnetizing procedure then results in the M(H) curve schematically shown in Figure 1.8.

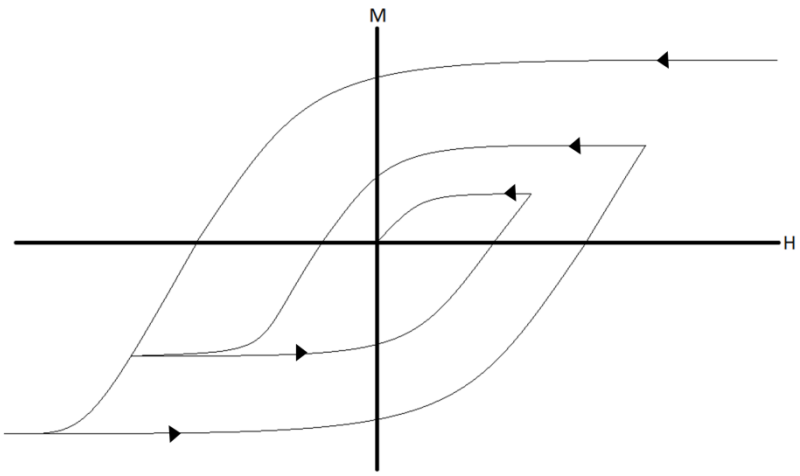

Figure 1.8 demagnetization curve M over H

1.1.5 Literature

µ-metal shields are typically used in room temperature applications, e.g. in a magnetometry laboratory [4]. However, at low temperatures most µ-metals permeability drops drastically. Since this is a large problem for shielding at cryogenic temperatures, the company called Vacuumschmelze GmbH & Co.KG specially developed the material CryoPerm. CryoPerm has the property that instead of decreasing, its permeability increases at low temperatures (Figure 1.9).

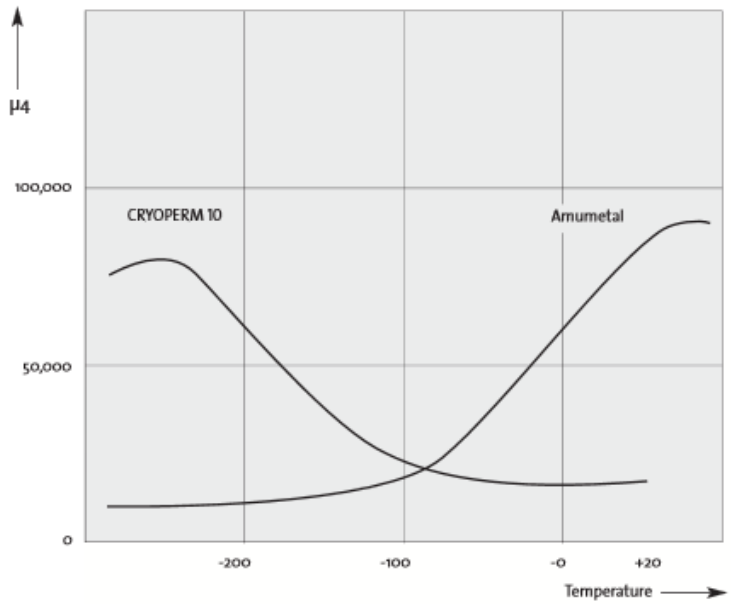

Figure 1.9 permeability of CryoPerm 10 and Arnumetal (high µ metal) over temperature (source picture: amuneal manufacturing corp, data sheet "*Custom Magnetic Shielding for Low Temperature Applications*", http://amuneal.com/sites/default/files/AmunealDataSheet2.pdf)

We also head to specify what "high" permeability is. The theoretical model is taken form [5]. Here the shielding factor determined for a model for cylinders and spheres is compared with respect to different parameters. One subject studied here is the shielding factor of a long cylinder is studied depending on relative permeability (μ/μ_0) and the thickness of the cylinder. The results of which are shown in Figure 1.10.

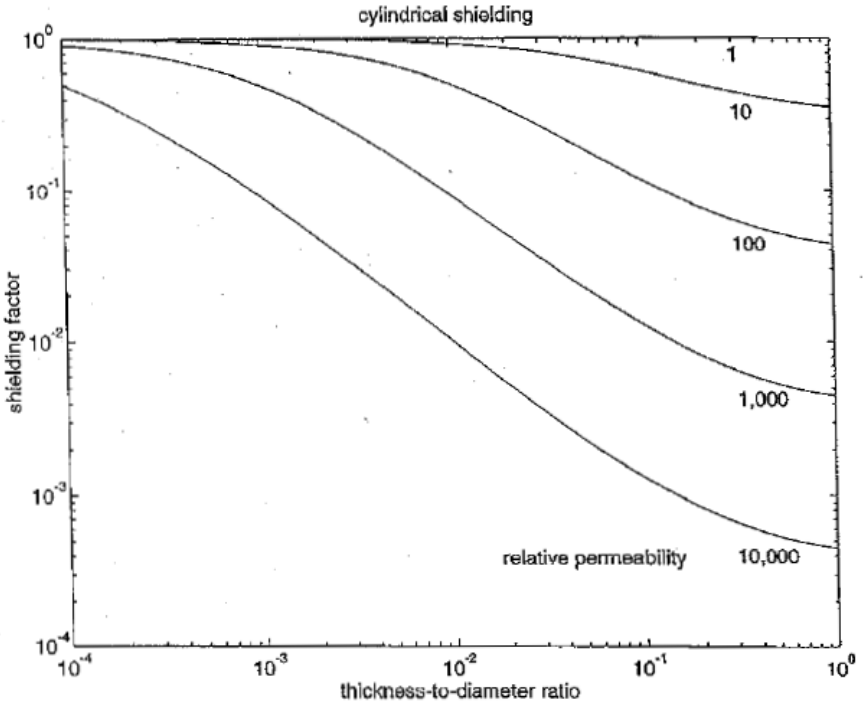

Figure 1.10 Flux shunting shielding for a long cylindrical shield. shielding factor s ($B_{measured}/B_{applied}$) is shown as a function of ratio of shield thickness to inner diameter (Δ/2a), for various values of relative shield permeability (μ/μ_0) (source picture: J.F.Hoburg, "*Principles of Quasistatic Magnetic Shielding with Cylindrical and Spherical Shields*", IEEE Transactions on Electromagnetic Compatibility 37 (4), pp. 574-579, 1995 [5])

For the Athena mission, SRON needs a shielding factor of 1000 or more. From Figure 1.10, it is estimated that at least a relative permeability of more than 10000 is needed or alternatively a very thick shield.

Another important aspect studied here is the effect of frequency on the shielding. Previous work [6] was done to look for a material needed to create a good EMI filter by comparing Mettglas with CryoPerm at cryogenic temperatures. The conclusion from this was that CryoPerm loses its effectiveness as a shield above frequencies of ~100Hz.

Another aspect studied is how hard it would be to achieve the shielding factor 1000 needed by SRON. In previous work [4] a shielding factor of 3000 was reached but this did require a combination of 5 shields made from P-80 to achieve, which indicates that it is not easy to achieve high shielding factors with little space.

1.2 Superconducting shields

1.2.1 Basic theory superconductors

In the frame of this assignment, also a few basic properties of superconductors need to be introduced. Here, we just expand on two key properties relevant for magnetic shields. First, a superconductor is a material that has no resistance below a certain temperature called the critical temperature (T_c). Second, type II superconductors in a magnetic field have two states the Meissner state and the vortex state. In superconductors charge carriers "condensate " into Cooper pairs. Cooper pairs are pairs of electrons that are bound together, both having opposite momentum. Further understanding of this pairing mechanism is not needed in this context and interested readers are referred to [7, ch.6].

The different magnetization states of a superconductor will be explained, beginning with the Meissner state. In the Meissner state, no magnetic field is present inside the superconductor. This implies that the right hand side of equation (3) is zero:

$$\boldsymbol{B} = \mu_0(\boldsymbol{H} + \boldsymbol{M}) = 0 \ \rightarrow \boldsymbol{H} = -\boldsymbol{M} \qquad (12)$$

The magnetization M cancels the applied field H exactly. Such a material is called a perfect diamagnetic material. In paragraph 1.1.1, it was shown that magnetization **M** can be described as a current over the materials surface. So the Meissner state has super-currents running over the materials surface, which cancel out the applied magnetic field.

Lets look at this surface a bit closer. No magnetic field may enter the material in the Meissner state. This means that the external field cannot have a perpendicular component on the surface of the material, since else the magnetic field would enter the material (surface currents can only influence parallel field components at an interface, the perpendicular component of the magnetic induction **B** is continuous across the interface). So it can be concluded that also outside the shield, there is no perpendicular component of the magnetic field on the surface when the shield is in the Meissner state($B_\perp = 0\ on\ the\ surface$). Just like with high-μ metals, the boundary condition is the basis of modelling the field around a superconductor.

Note that in reality the magnetic field does penetrate the material a certain depth. This so-called penetration depth λ is material and temperature dependent. However, in this assignment, we assume that the shield thickness>>λ, so that we can neglect this effect.

Another property of the Meissner state is that it is destroyed if a high enough magnetic field is applied. This threshold is called the first critical field H_{c1}. At higher fields, the kinetic energy of the super-currents becomes too high and they cannot cancel out the applied field anymore. At that point, a magnetic field gets inside the superconductor which causes the Meissner state to break down. However, this doesn't break down superconductivity itself.

Above H_{c1}, a second magnetization state is created inside the material called the vortex state. In this state, small areas of normal metal are surrounded by circulating currents called vortices.

This state also breaks down if a high enough magnetic field is applied, called the second critical field H_{c2}. The vortex density grows with increasing external field. At a high enough magnetic field vortices will start to touch, which causes superconductivity to break down. For further discussion of the subject the reader is referred to [8, ch.4].

The transitions between these states (i.e. H_{c1} and H_{c2}) dependent on temperature, as described in Figure 1.11.

For this assignment, two ways to cool-down a material below the critical temperature T_c with a field present are studied. Either the field is first removed then the sample is cooled and finally the field is applied again (zero-field cooling), as indicated in Figure 1.11(1). Alternatively, the sample is cooled through the critical temperature T_c while the field is present (field cooling) as seen in Figure 1.11(2). The consequences for shields are explained paragraph 1.2.2 and 1.2.4.

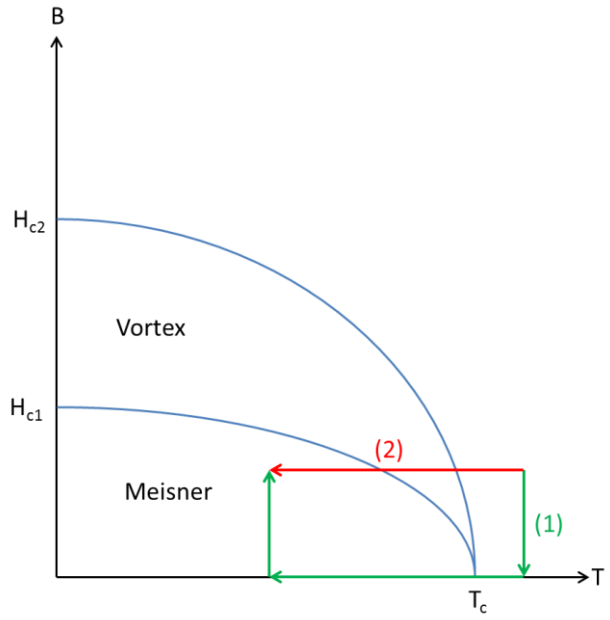

Figure 1.11 Magnetic "phase diagram" of type II superconductor, indicating the phase boundary $H_{c1}(T)$ between the Meissner- and vortex state and $H_{c2}(T)$ between the vortex- and normal state. Also indicated are two possible trajectories

to take a superconductor from a state (T_2,H) to state (T_1,H), with $T_1<T_c<T_2$. Trajectory (1) is called zero-field cooling, (2) is field cooling

1.2.2 Remanence in superconductor

We already mentioned how remanence may limit the effectivity of a magnetic shield. For superconductors there are two types of remanence: geometric flux trapping and vortex trapping.

First, geometric flux trapping will be explained. It is caused by the magnetic field that is created by super-currents because of the geometry of the material when a magnetic field is present during cool down through the critical temperature. As an example, a cylinder of superconducting material is taken at a temperature above T_c and a field is applied in its axial direction (Figure 1.12a). Now the cylinder is cooled down through T_c with the field still applied (Figure 1.12b). Then the field is turned off. The superconductor will "want" to keep the flux inside the cylinder constant because of Faraday's law (equation (1b)). Rotating super-currents will start to flow on a macroscopic scale, creating a magnetic field inside the cylinder (Figure 1.12c). This causes geometric flux trapping in the cylinder.

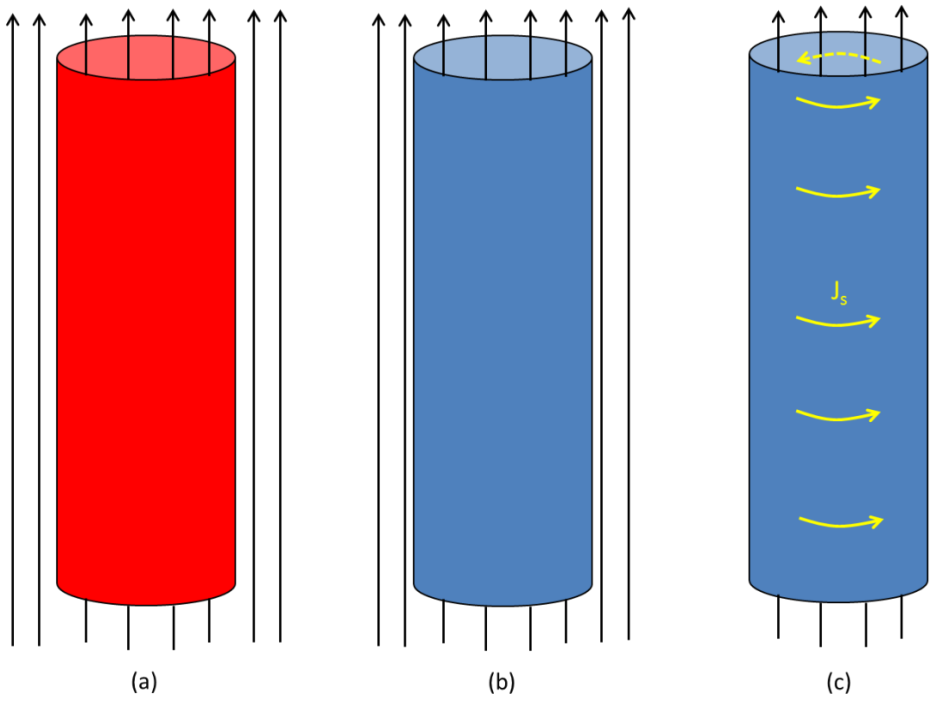

Figure 1.12 illustration of geometric flux trapping; black arrows represents the applied field, yellow lines induced super-current, a) field applied cylinder in normal state ($T>T_c$), b) field still applied cylinder in superconducting state ($T<T_c$), c) field turned off, internal field created by rotating super-currents.

Geometric trapping causes problems for a superconducting magnetic shield, since it results in a permanent field "frozen" inside it due to this remanence.

This effect can be countered by making sure no magnetic field is present during cooling, e.g. as in the hybrid assembly shown in Figure 1.1 by adding an extra μ-metal shield. In such case, geometric flux trapping is minimised by making sure that only a very low field is present during cool-down to be trapped and Faraday's law will keep de field inside the cylinder close to zero. Super-currents will cancel any field applied after cooling. Essentially this method follows path (1) from Figure 1.11.

The second form of remanence is vortex trapping. As mentioned in paragraph1.2.1, vortices are small areas inside a superconductor where the material is in the normal state. In these areas magnetic field can go through the superconductor, creating a weak spot in the shield. On a microscopic scale, the magnetic field present inside the vortex causes the same effect as with the macroscopic geometric flux trapping: magnetic field is permanently trapped inside the vortex. Even if the shield is used in the Meissner stare, a field-cooled trajectory inevitably must pass through the

vortex state, as can be seen in Figure 1.11. As we will see below, vortices which are "pinned" at material inhomogeneities will "survive" in the Meissner state and will give rise to a remanent field.

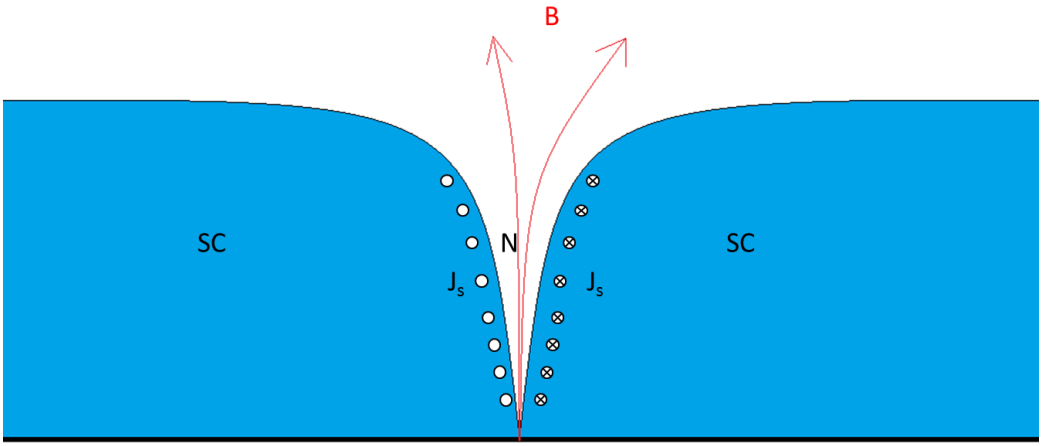

Figure 1.13 illustration of vortex trapping, blue is superconducting state, white normal state, red arrows magnetic field, black dot crosses super currents

Since these 2 forms of remanence cause problems for magnetic shielding they need to be removed with a demagnetization procedure. This is for superconductors quite simple. The material is brought back above the critical temperature T_c and cooled down again. However if the field remains present during cool-down, the remanence will not be removed. So for a practical demagnetization the material should be brought above T_c and then lowered below T_c but with no field present.

1.2.3 Literature

Several techniques have been proposed and/or used to avoid remanence in superconducting shields. A first example is used to shield a space-based gyroscope [9]. Here the shield is made of a lead balloon. It is deflated during cool-down and inflated while superconducting. This setup relies on "a trial and error" principle since the amount of magnetic shielding is not certain. Furthermore, a large and complex apparatus is needed to inflate the lead balloon and to move it over the sample.

A second example is described in [10]. In this case, a device is used to locate trapped flux and to move it to a buffer zone. This is done by locally heating the area around the trapped flux and thus "pushing" it out of the shield. This technique has the problem that it requires a large and complex apparatus which is not practical for a satellite. Another disadvantages is that it only removes vortex trapping, not geometric trapping.

A third example is proposed in [11]. In this case a current through the shield simultaneous with a magnetic field applied along the shield causes the flux quanta to move to buffer zones made in the top and bottom of the shield. However, this technique does nothing against geometric flux trapping, while the power supply and coil needed to make the magnetic field add a lot of bulk and weight to the setup.

1.2.4 New technique

For its collaboration with SRON, the UT proposed a new technique to avoid flux trapping and remanence, as explained below. Part of this assignment was to estimate the feasibility of this new method using the Ginzburg-Landau model, as discussed in detail in paragraph 2.2.1. In this paragraph, we simply describe the proposed procedure and use a "hand-waving" argument to discuss the possible problem with it. The method aims to create a superconducting cylinder that is cooled down while a magnetic field is applied, but will have no problems with geometric flux trapping as described in paragraph 1.2.2. This means that the field-cooled path (2) from Figure 1.11 is modelled.

The advantage would be that this technique could be achieved with only one single shield. The μ-metal shield would become redundant and this would save space and weight in a satellite.

First the technique will be explained with an example: consider a superconducting cylinder at a temperature above T_c and with a magnetic field B applied along its z-axis (Figure 1.14a). First the

flux through the top opening is made zero by applying a counter field (Figure 1.14b). Although this is a form of active shielding, note that only a small portion of the shield needs to be made flux-free. This greatly limits the size, weight and power consumption of the compensation coil. Next, this top part will be made superconducting by applying a controlled temperature gradient over the cylinder in such a way that the temperature decreases from top to bottom (dT/dz<0). An interface between the superconducting and normal state is thus created on the cylinder. Then, the counter magnetic field is turned off and the super-currents take over to cancel out the applied field (Figure 1.14c). Now the temperature gradient is moved down, which causes the N/S interface to move down and makes more of the cylinder superconducting. The idea behind the trick is that the field will be "pushed out" by the moving interface. When the interface reaches the bottom it will have pushed the magnetic field out of the whole cylinder including it inner volume (Figure 1.14d).

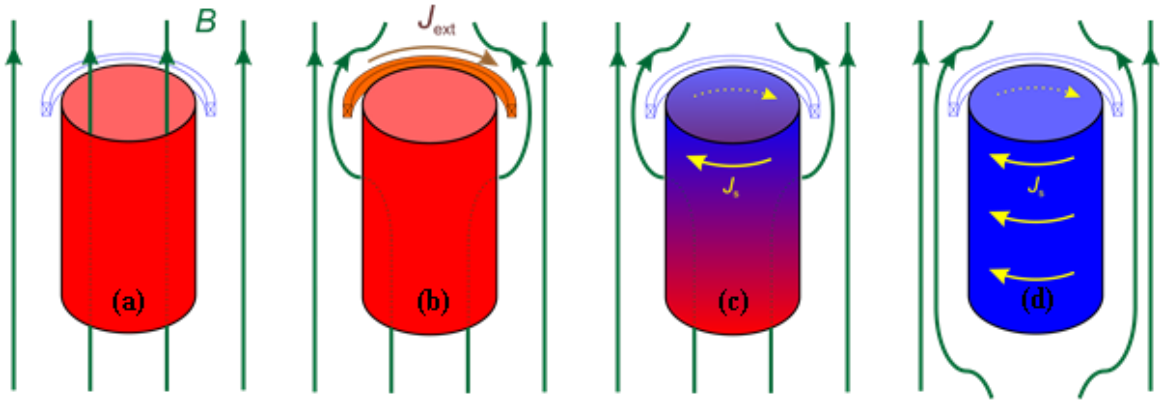

Figure 1.14 red is normal metal, blue is superconducting metal, a) the cylinder is in normal state and field is present, b) the top opening is made flux-free with a coil, c) The top is made superconducting, creating an interface between superconducting state and normal state, d) the interface is moved down and pushes out the field until the shield is entirely superconducting and no field is present anymore

One of the possible problems foreseen with this technique is the interaction between material inhomogeneity and the moving N/S interface. This could cause vortex trapping.

A rough estimate of this effect can be made based on simple arguments [12]. The argument uses the coherence length ξ, which can be seen as the typical "thickness" of the N/S interface. Just like the penetration depth λ, discussed in paragraph 1.2.1, ξ is temperature dependent as will be discussed in more detail in paragraph 2.1.2

This argument aims to estimate the minimum temperature gradient that is necessary to make the new method work in the presence of defects. With "defects" we mean material inhomogeneities that cause a local depression ΔT_c of the critical temperature. A constant temperature gradient is assumed ($T(x) = T_0 - |\nabla T| x$), with T_0 the temperature at the interface and ∇T the imposed temperature gradient (Figure 1.15). This estimate assumes that a defect can be described as a local suppression of the transition temperature $T_c - \Delta T_c$ in a certain point x_d. The main idea is as follows: as long as the defect remains within the coherence length ξ of the interface before it becomes superconducting, no vortex will be created. However, if the defect falls outside the coherence length, a vortex is created and the proposed technique doesn't work. The defect becomes superconducting when $T(x_d) = T_c - \Delta T_c$. Since T_0 is taken at T_c, this temperature becomes $T(x_d) = T_0 - |\nabla T| x_d$, giving the point $x_d = \frac{\Delta T_c}{|\nabla T|}$. So the coherence length must be bigger than x_d with temperature $T=T_c-\Delta T_c$. Next, we consider temperature dependence of the coherence length $\xi = \frac{0.74}{\sqrt{1-\frac{T}{T_c}}}$ (see also paragraph 2.2.2). The requirement that the coherence length at this defect needs to be bigger then $x_d = \frac{\Delta T_c}{|\nabla T|}$ leads to a minimum value for the gradient, equation (13)

$$\xi(x_d) = x_d \rightarrow \frac{0.74\xi_0}{\sqrt{\frac{\Delta T_c}{T_c}}} > \frac{\Delta T_c}{|\nabla T|} \rightarrow |\nabla T| > \left(\frac{\Delta T_c}{T_c}\right)^{3/2} \frac{1}{0.74} \frac{T_c}{\xi_0} \qquad (13)$$

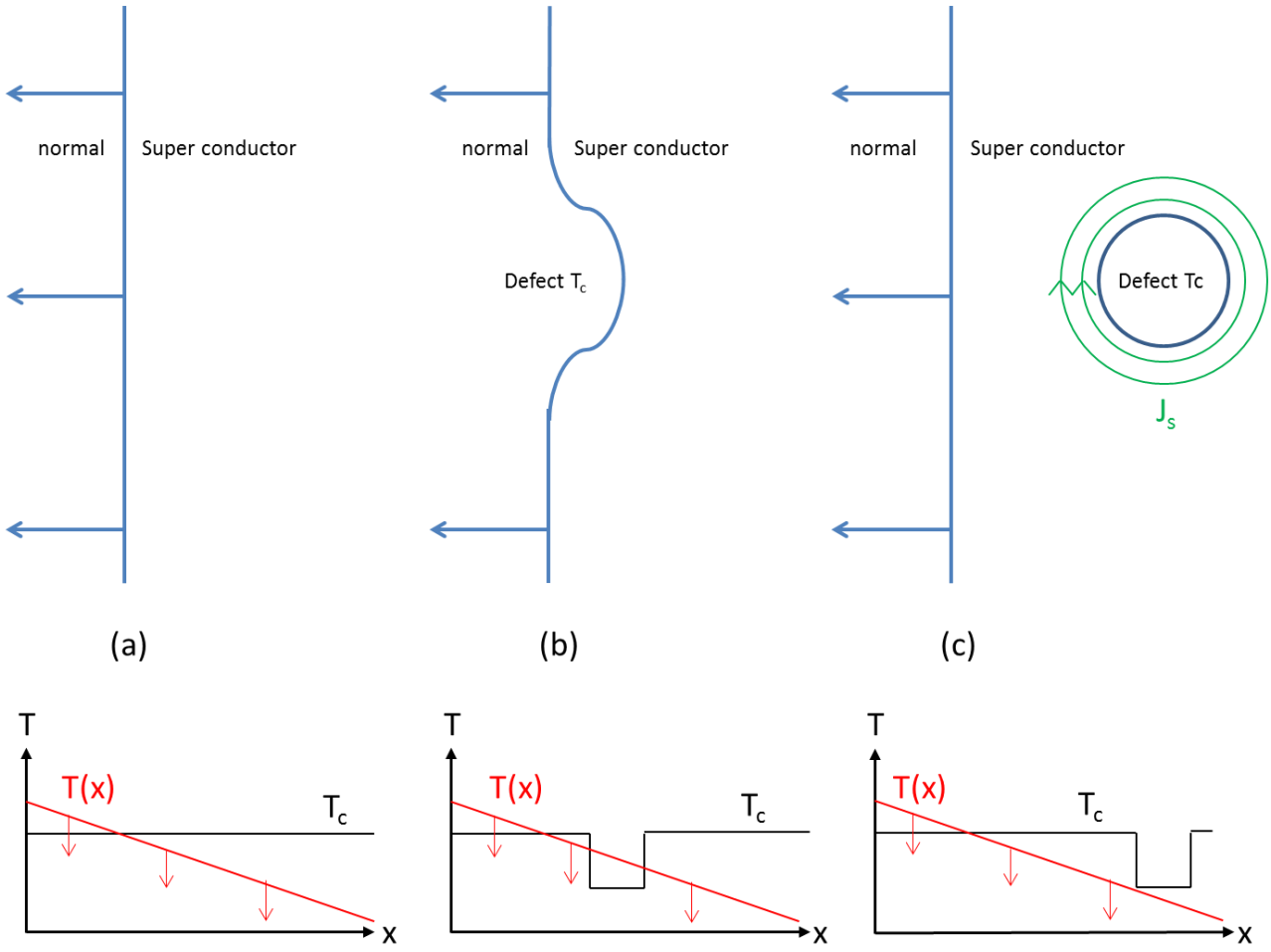

Figure 1.15 Illustration what would happen if a defect is present near the interface between normal and superconducting state, a) no defect present, b) defect present on the interface, c) defect has created a vortex in the superconductor

1.3 Structure of this assignment

Chapter 2 gives more details about the theory and modelling. In this chapter, the Ginzburg-Landau (GL) theory will briefly be explained and a 1-dimensional GL numeric model will be set up to describe the cool-down in the presence of inhomogeneity. Different numerical approaches to solve the resulting non-linear equations are discussed. Furthermore, analytical expressions for simple geometries of both superconductors and high-μ metals are reviewed and a linearized FEM (Comsol MultiPhysics) is discussed to treat more complex geometries.

Chapter 3 treats the experimental setup and methods used to study simple CryoPerm and Nb shields. Also previous measurements done with a Hall probe on the CryoPerm shield will compared with the new measurements done with the SQUID sensor.

Chapter 4 reviews the results. Here all the results from the measurements will be compared with those from the modelling and also the result of the GL model for the new cooling method will be shown.

Finally, chapter 5 gives a general discussion and conclusion of the experimental and modelling results.

2 Theory & models

As mentioned in chapter 1, the goal of this assignment is 2-fold: 1) to validate straight forward models as a design tool for magnetic shields (and especially, to check experimentally where the models break down due to effects such as remanence); and 2) to construct a first numerical model for the cool-down of a superconductor in presence of a magnetic field, in order to check the hand-wavy argument described in paragraph 1.2.4

In this chapter, we describe the models that are used in more detail. Paragraph 2.1 first describes a number of analytical approaches, either to estimate the remanence of μ-metal cylinders or to describe the shielding obtained with superconducting disks and cylinders in the Meissner state. Next, we discuss the general features of finite element models, which are implemented in this assignment with commercial software.

Paragraph 2.2 then deals with the Ginzburg-Landau (GL) approach that was taken to model the in-field cool-down of a type II superconducting shield. First the key ingredients of the GL description are introduced and then the standard GL equations are adapted to incorporate a thermal gradient. The section excludes with a brief discussion of the numerical recipe chosen to solve the resulting equations.

2.1 Analytical and "FEM" modelling

2.1.1 General analytical approach

In this assignment, all analytical models treat cylindrical systems, so the choice of a cylindrical coordinate system makes more sense. This coordinate system consist of the three coordinates: r perpendicular to the cylinder wall, θ parallel to the cylinder wall and z along the length of the cylinder. The representation of this coordinate system (compared to the usual x,y,z coordinate system) is shown in Figure 2.1.

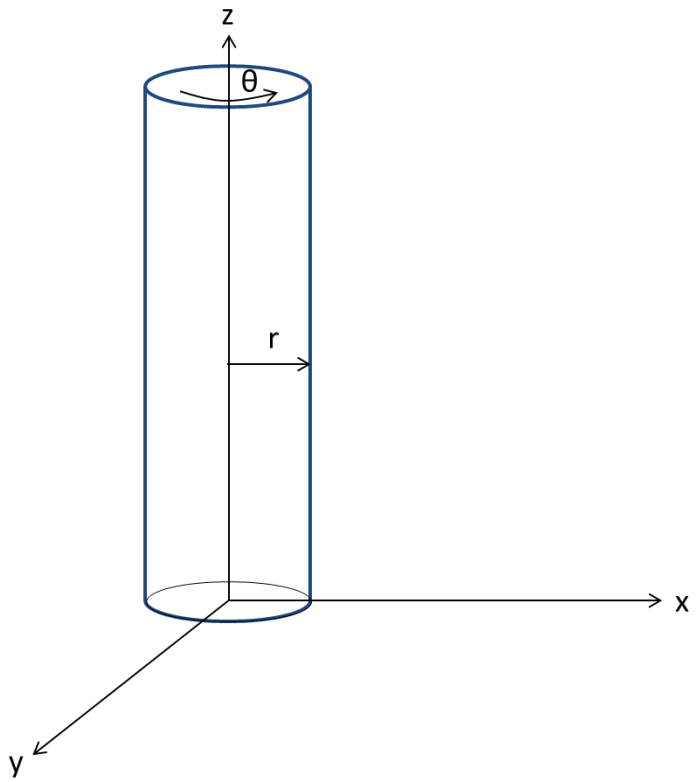

Figure 2.1 the cylindrical coordinate system

In regions of space without current, a scalar magnetic potential ϕ can be defined such that $H = -\nabla\phi$ [13] the field can then be found by solving the Laplace equation $\nabla^2\phi = 0$. In cylindrical coordinate system the Laplace equation is written in terms of r, θ and z as:

$$\nabla^2 f = \frac{d^2 f}{dx^2} + \frac{d^2 f}{dy^2} + \frac{d^2 f}{dz^2} = 0 \tag{14}$$

$$\nabla^2 f = \frac{1}{r}\frac{d}{dr}\left(r\frac{df}{dr}\right) + \frac{1}{r^2}\frac{d^2 f}{d\theta^2} + \frac{d^2 f}{dz^2} = 0 \tag{15}$$

The equation is solved with the ansatz of separation of variables. The function f(r,θ,z) that depends on multiple variables as the product of three independent functions, each dependent only on 1 of the variables:

$$f(r,\theta,z) = R(r)\Theta(\theta)Z(z) \tag{16}$$

This has the advantages that it results in a set of ordinary differential equations, rather than one involving partial differentials.

Now a couple of analytical models needed for comparison with the experimental results will be discussed.

Axially magnetized μ-metal cylindrical shell

The first model is about the magnetic field produced by a cylinder made from high-μ metal and magnetized in the z-direction. This model is used in paragraph 4.1.2 to analyse the measured remanence on the axis of a μ-metal shield. For this the theory from paragraph 1.1.1 (the magnetization of a material can be seen as a current over its surface) is used. Using the previously discussed theory, the magnetization can be represented by a current going clockwise in the inner surface of the cylinder and counter-clockwise on the outer surface (Figure 2.2).

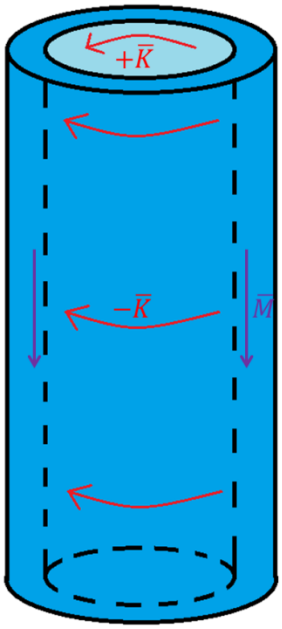

Figure 2.2 surface currents caused by the magnetization of an axial magnetized cylinder

These currents may be represented by two coils, one at radius of the inner surface with a current going clockwise and the other at the outer surface with counter-clockwise current. The analytical descriptions of a coil with finite length in cylindrical coordinates only provides magnetic field values along the vertical symmetry axis (at r=0). [2 ,problem 5.11]. The formula derived for such a coil is:

$$\bar{B}(r=0,\theta,z) = \frac{\mu_0 K}{2}\left[\frac{z+h}{\sqrt{(z+h)^2+R^2}} - \frac{z}{\sqrt{z^2+R^2}}\right]\hat{z} \tag{17}$$

Here h is the height of the coil, R its radius of the coil and K is the sheet current in the coil.

Now this single coil can be extended to model two coils in opposite direction as a model for an axially magnetized hollow cylinder. This analytical formula is given in equation (18). In this equation h_c is height of the cylinder, R_i its inner radius, d the thickness of the cylindrical shell and K is the sheet current density on the surface.

$$\bar{B}(r=0,\theta,z)=\frac{\mu_0 K}{2}\left[\frac{z+h_c}{\sqrt{(z+h_c)^2+{R_i}^2}}-\frac{z}{\sqrt{z^2+{R_i}^2}}-\left(\frac{z+h_c}{\sqrt{(z+h_c)^2+(R_i+d)^2}}-\frac{z}{\sqrt{z^2+(R_i+d)^2}}\right)\right]\hat{z} \tag{18}$$

Transverse components of the remanence in a magnetized hollow cylinder

The Second model is needed to determine the effect of magnetization of the cylinder along the r- and θ-direction at z = 0 and will be compared to measured data in paragraph 4.1.2. This model requires equation (1a) and equation (2) and is written out in appendix A. The results may be written as a general solution of the Laplace equation (15), leading to:

$$B_r(r,\theta,z=0)=\frac{-1}{r}(E_0\ln r+F_0)+\sum_{k=1}^{\infty}\left(E_k r^{k-1}+F_k r^{-(k+1)}\right)\sin[k(\theta-\varphi_k)] \tag{19a}$$

$$B_\theta(r,\theta,z=0)=(E_0\theta+G_0)\frac{1}{r}+\sum_{k=1}^{\infty}\left(E_k r^{k-1}-F_k r^{-(k+1)}\right)\cos[k(\theta-\varphi_k)] \tag{19b}$$

The coefficients E_k, F_k and G_k are once more interpreted in terms of surface currents, as we will see later.

Magnetic field near simple cylindrical systems in the Meissner state

Several analytical models are found in literature for superconducting shields in the Meissner state. All rely on the boundary condition $B_\perp = 0$ discussed in paragraph 1.2.1. Some examples are now given below.

In [14], a scalar magnetic potential ϕ(r,θ,z) is introduced and the boundary condition $B_\perp = 0$ is used to work out the field near superconducting disks or hollow cylindrical shells. The main conclusion is that an external field is attenuated exponentially with axial depth inside the shell (or distance to the disk). Although these results are directly qualitatively relevant for this assignment, the geometries discussed are too simple to describe a complex-shaped shield such as the one in Figure 1.1 quantitatively.

In [15], an analytical model is made for a closed superconducting "cup". The author uses Green's theorem to find the potential of the cup and then breaks it up into multiple regions in order to solve them individually. It is also mentioned in this paper that this technique could be used for far more complex shapes, but no actual examples are shown. When this was studied closer for this assignment, it was quickly concluded that relevant complex shapes would require numerical techniques to solve the resulting system of boundary conditions and it was decided that the models for the superconducting Meissner shield could be better made using a finite element approach, as explained below.

2.1.2 Finite element approach

The finite element approach used in this assignment is implemented in the commercial program Comsol MultiPhysics. This method is used to model more complex geometries where no analytical method is present. For the finite element method, the problem needs to be defined inside a certain space. This space is then broken up into a grid of triangles as illustrated in Figure 2.4. Inside this space the differential equations are known. These can be different depending on the area inside the space. Next the boundary conditions of the problem need to be implemented. Now with these boundary conditions and differential equations, the solution is constructed grid point by grid point. This results in an approximate solution of the problem. For further discussion of the finite element method, the reader is referred to [16].

Comsol MultiPhysics is used by SRON and also in this assignment to model the shields. One of the reasons for this work is to validate these models with the measurements that were done in the assignment and are presented in chapter 4.

The models used here and some of the results are shown below.

For the high-μ metal, shield a model of two nested cylindrical shells is made in an axial symmetric system (Figure 2.3).

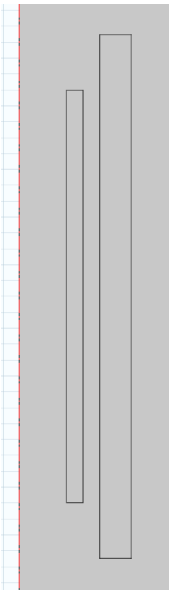

Figure 2.3 axis-symmetric model description for the high-μ metal shield

For the superconducting shield a model is made (Figure 2.4) once more using the boundary condition $B_{\perp} = 0$ on the surface of the shield in the Meissner state. In Comsol this boundary condition is implemented as "magnetic insulation". In this model, the superconducting shield consists of two pieces which are combined with a narrow gap between them. This is explained in more detail in paragraph 3.3.1.

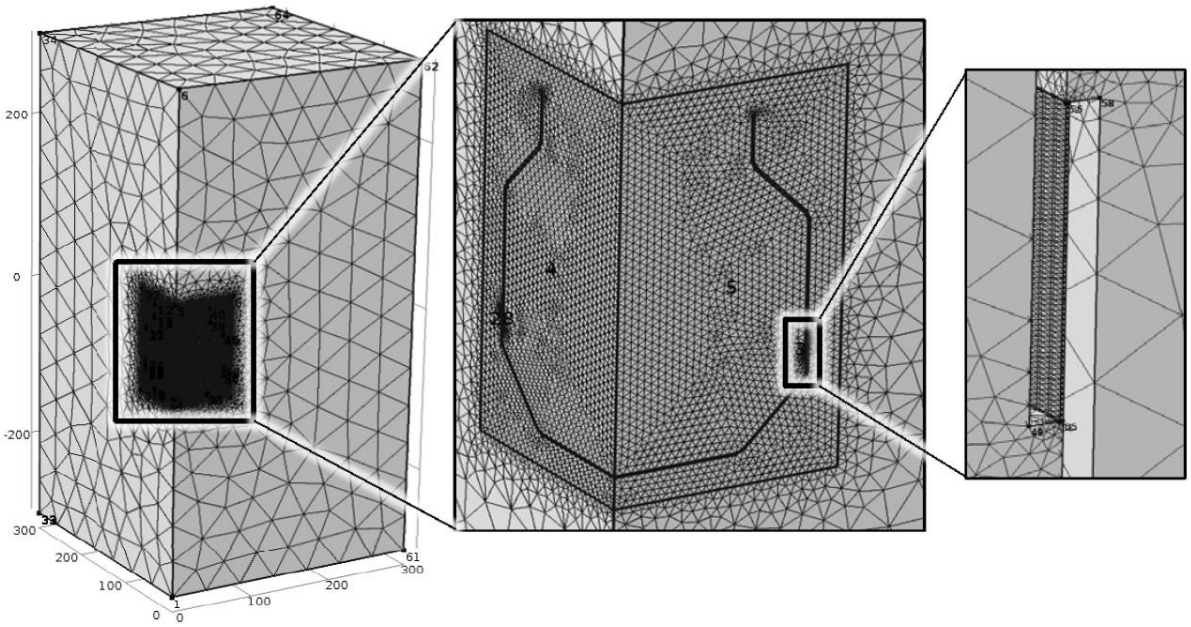

Figure 2.4 model description for superconducting shield

To give a first impression, some results of the model of the superconducting shield are also shown below (Figure 2.5).

a)

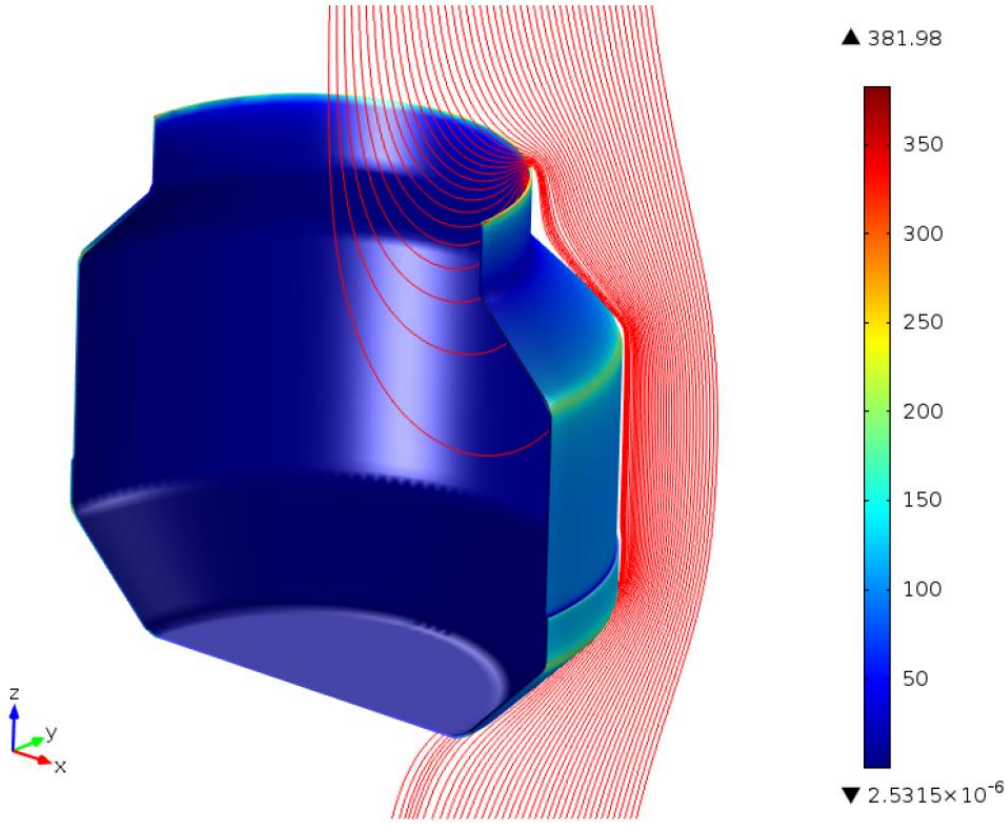

b)

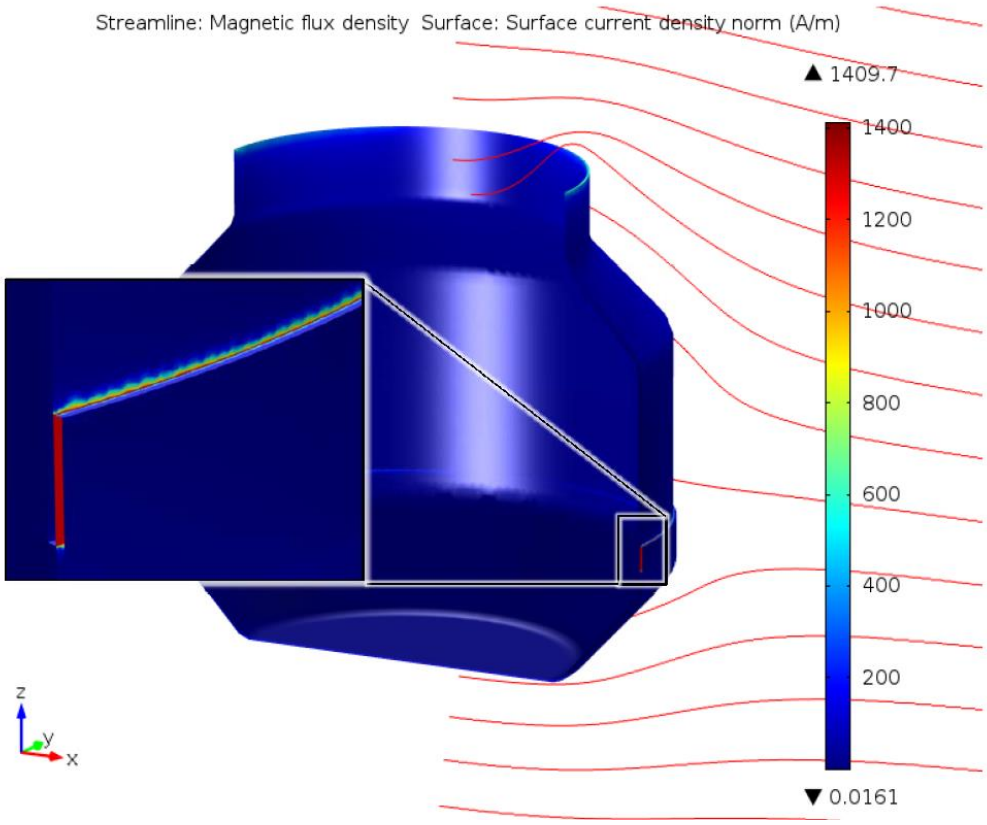

Figure 2.5 examples of the magnetic field inside and around the superconducting shield, a) axially applied field, b) transverse applied field. The insert in b) shows the overlap region between the main shield and the bottom shield cover in more detail

2.2 Ginzburg-Landau theory

2.2.1 Basic Ginzburg-Landau theory

Ginzburg-Landau (GL) theory was derived by Vitaly Ginzburg and Lev Landau in 1950, based on one of Landau's earlier theories of second-order phase transition. In this theory the free energy minimum is found by describing it in terms of an order parameter and demanding that its partial derivatives with respect to this parameter are zero. One of the important consequences of this approach is that it is only accurate close to the critical temperature T_c.

When creating the theory, Ginzburg and Landau had an important realization. This was that apart from the magnetic field, also a second variable was needed for a complete description of superconductors. They then realized that just like in quantum mechanics a complex wave function ψ could be introduced as order parameter. Later ψ was found to be the wave function of the Cooper pairs, defined as $|\psi|^2$= Cooper pair density.

This wave function ψ starts to develop at the interface between a normal (ψ=0) and superconducting region (ψ≠0). However, ψ needs a certain length to develop inside the superconductor, the so-called coherence length ξ[1]. Using this information and the previously introduced penetration depth λ of the magnetic field, a qualitative description of the interface between a normal and superconducting metal can be already made (Figure 2.6).

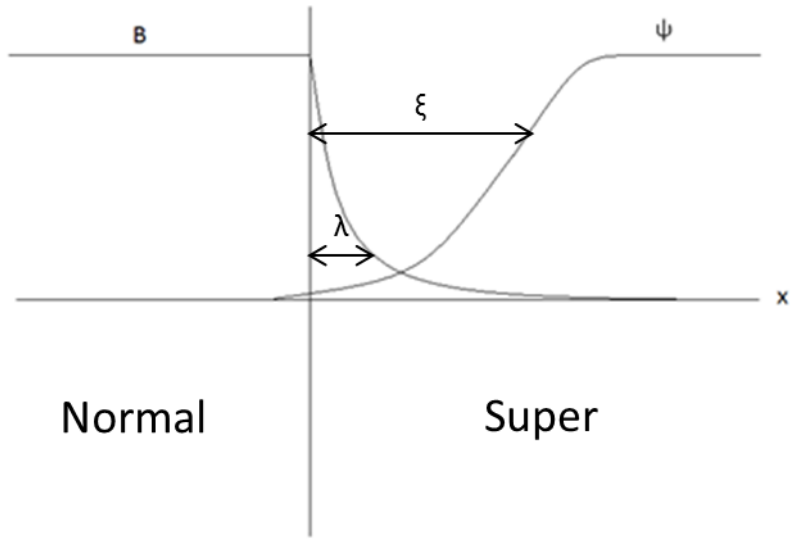

Figure 2.6 representation of the magnetic field B and the magnitude of the superconductors order parameter ψ at the boundary between normal metal and superconducting metal

However, the approach allows also to quantify the situation in the form of the GL equations. To derive these equations first the GL energy equation (equation (20)) is needed.

$$f(\boldsymbol{r}) = f_n + a|\psi|^2 + \frac{1}{2}b|\psi|^4 + \frac{1}{2m^*}|(-i\hbar\nabla - e^*\boldsymbol{A})\psi|^2 + \frac{\boldsymbol{B}^2}{2\mu_0} - \frac{\mu_0 \boldsymbol{H}_0^2}{2} \qquad (20)$$

This equation is easiest understood when broken into parts. The first 3 terms in the equation ($f_n + a|\psi|^2 + \frac{1}{2}|\psi|^4$) represent the equilibrium energy deep inside the superconductor. It should be mentioned that the parameter a is negative in the superconductor: f(|ψ|) needs to have to minima at $\pm\sqrt{\frac{-a}{b}}$ to achieve superconductivity and these minima are only present if a<0. Second, the middle part

[1] As discussed below, the gradient of |ψ| is associated to the current density. A too high gradient would imply a too high kinetic energy of the Cooper pairs

($\frac{1}{2m^*}|(-i\hbar\nabla - e^*\boldsymbol{A})\psi|^2$) is the equation for kinetic energy with a magnetic field applied. Finally, the end part ($\frac{\boldsymbol{B}^2}{2\mu_0} - \frac{\mu_0 \boldsymbol{H}_0^2}{2}$) represents the energy of the magnetic field.

In the GL energy equation (equation (20)) there are two variables present: the wave function ψ and the vector potential A (the magnetic field B is not independent, since it is rewritten as function of A using equation (2). To derive the GL equations, the minimum of the energy needs to be found with respect to ψ and A. This is done by taking the derivative of equation (20) to ψ and A separately and putting the results equal to zero. This is written out in more detail in appendix C. The famous resulting GL equations then become:

$$a\psi + b|\psi|^2\psi + \frac{1}{2m^*}|(-i\hbar\nabla - e^*\boldsymbol{A})|^2\psi = 0 \tag{21a}$$

$$\boldsymbol{J} = -\frac{e^* i\hbar}{2m^*}[\psi^*\nabla\psi - \psi\nabla\psi^*] - \frac{e^{*2}}{2m^*}\boldsymbol{A}|\psi|^2 \tag{21b}$$

2.2.2 Ginzburg Landau theory and the proposed cooling method

For this assignment, the GL equations are used to model the new field-cooling technique described in paragraph 1.2.4. The GL theory was chosen because it best describes the interface between a superconducting and normal metal and this is exactly the area where most of the problems are expected.

For this model, the temperature dependence of the GL equations needs to be made explicit. The starting point are the GL equations as derived above (equations (21a,b)). To make the equations simpler, some assumptions are made. The first assumption is that the magnetic field is applied in the z-direction and only x-dependent. With that information and using equation (2) the vector potential can be chosen in the y-direction and x-dependent ($\boldsymbol{A} = A_y(x)\hat{y}$). The second assumption is that the wave function may be broken into parts: a real part f which is x-dependent and a phase θ which depends linearly on y. This results in :$\psi(x,y) = \psi_\infty f(x)e^{i\theta(y)} = \psi_\infty f(x)e^{iky}$. To simplify the notation further, some definitions are needed. The first "definition" is equation (1a) ($\mu_0\boldsymbol{J} = \nabla \times \boldsymbol{B}$). The other definitions are the coherence length ξ, the penetration depth λ and the equilibrium value of the wave function defined as: $\psi_\infty^2 = \frac{-a}{b}, \xi^2 = \frac{\hbar^2}{2m^*|a|}, \lambda^2 = \frac{m^*}{\mu_0 e^{*2}\psi_\infty^2}$. Finally, the flux quantum φ_0 and the GL parameter κ are defined as: $\phi_0 = \frac{h}{e^*}, \kappa = \frac{\lambda}{\xi}$. Using these definitions and assumptions, equations (22a,b) can be rewritten as:

$$\xi^2\frac{d^2(\psi_\infty f)}{dx^2} - \left(\xi k - \frac{2\pi\xi}{\phi_0}A\right)^2\psi_\infty f + \psi_\infty f - \psi_\infty f^3 = 0 \tag{22a}$$

$$\frac{2\pi\xi(\kappa\xi)^2}{\phi_0}\frac{d^2A}{dx^2} + \left[\xi k - \frac{2\pi\xi}{\phi_0}A\right]f^2 = 0 \tag{22b}$$

In these equations there is still no temperature dependence. However, it is known that the parameter *a* form equation (21a) is temperature dependent. Since ξ and ψ_∞ both depend on the parameter *a*, they will also be temperature dependent. This results in:

$$a \propto \left(\frac{T}{T_c} - 1\right)$$

$$\xi^2 = \frac{\hbar^2}{2m^*|a|} \propto \frac{1}{1 - \frac{T}{T_c}} \rightarrow \xi = \frac{\xi_0}{\sqrt{1 - \frac{T}{T_c}}} \tag{23}$$

$$\psi_\infty^2 = \frac{-a}{b} \propto 1 - \frac{T}{T_c} \rightarrow \psi_\infty = \psi_{\infty 0}\sqrt{1 - \frac{T}{T_c}} \tag{24}$$

Now the temperature dependence of ξ and ψ_∞ can be implemented into equations (22a,b) which makes the GL equations explicitly temperature dependent. This derivation is written out in more detail in appendix D.

2.2.3 Numerical solutions of Ginzburg Landau equations

Here the model for the new controlled field cooling technique, as described in paragraph 1.2.4, is written out. To model this procedure, the GL equations are solved numerically with the program labview.

The GL equations are solved for a 1D system extending in the x direction with the interface between superconductor and normal metal at x=0. The assumptions taken here are that the amplitude of the wave function ψ varies in the x-direction and that the magnetic field B is applied in the z-direction. Using equation (2) we can choose a vector potential A in the y-direction corresponding to a current density J is in the y-direction, as shown in Figure 2.7

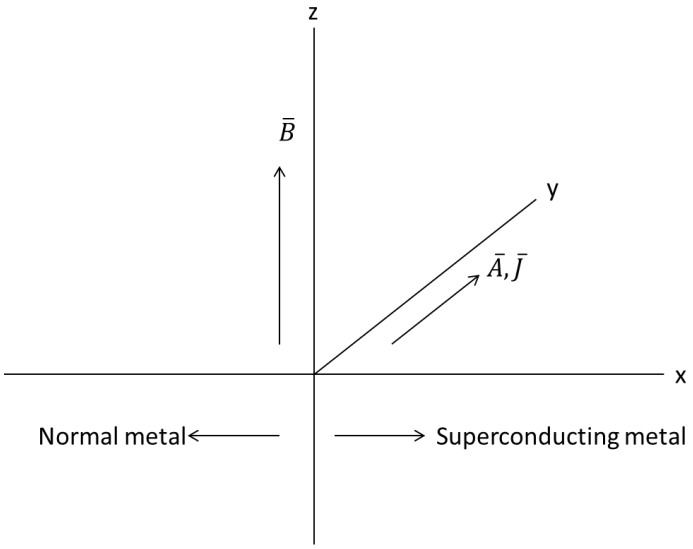

Figure 2.7 illustration of the system for the Ginzburg Landau equations

Now the boundary conditions need to be defined. These are taken from Figure 2.6 since they reflect the general shape expected for the results:

$$B_z(0) = \frac{\mathrm{d}A_y(x)}{\mathrm{dx}}_{x=0} = B_0, \qquad B_z(\infty) = \frac{\mathrm{d}A_y(x)}{\mathrm{dx}}_{x=\infty} = 0$$

$$\frac{df}{dx}_{x=0} = b, \qquad f(\infty) = 1$$

So it is expected that the magnetic field is equal to the applied field at the interface and zero deep inside the superconductor. The amplitude of the wave function has a derivative b on the interface and is fully developed (and constant) deep inside the superconductor. It might be expected that the gradient of the real part of the wave function is zero at the interface, but Cooper pairs tunnel into the normal metal at the interface through quantum tunnelling so a certain non-zero gradient b develops [17]. Since b is material-dependent we treat it as a free parameter. To keep the system simple, the temperature gradient is taken to be constant:

$$T(x) = T_0 - \nabla T x$$

with T_0 as the temperature at the interface between superconductor and normal metal and ∇T as the temperature gradient.

When all this is implemented into equations (22a,b), it results in equations (25a,b).

$$\xi_0{}^2\frac{d^2f}{dx^2}-\left(\xi_0 k-\frac{2\pi}{\phi_0}\xi_0 A\right)^2 f+f-f^3 + \tau\left[\xi_0\frac{1}{1-t_0+\tau u_0}\frac{df}{dx}-f\frac{1}{4}\frac{\tau}{(1-t_0+\tau u_0)^2}+u_0 f-u_0 f^3\right]-t_0[f-f^3]=0 \quad (25a)$$

$$\frac{2\pi\kappa^2\xi_0{}^3}{\phi_0}\frac{d^2A}{dx^2}+\left[\xi_0 k-\frac{2\pi\xi_0}{\phi_0}A\right]f^2+\tau u_0\left[\xi_0 k-\frac{2\pi\xi_0}{\phi_0}A\right]f^2-t_0\left[\xi_0 k-\frac{2\pi\xi_0}{\phi_0}A\right]f^2=0 \quad (25b)$$

ξ_0 is the coherence length at T=0. To make the model easier to calculate, the variables are made dimensionless by defining $t_0\equiv\frac{T_0}{T_c},\tau\equiv\frac{\nabla T}{T_c}\xi_0,u\equiv\frac{x}{\xi_0},\alpha_0\equiv\xi_0 k-\frac{2\pi\xi_0}{\phi_0}$.

Implementing these results in equations (26a,b).

$$\frac{d^2f}{du^2}-\alpha_0{}^2 f+f-f^3+\tau\left[\frac{1}{1-t_0+\tau u}\frac{df}{du}-f\frac{1}{4}\frac{\tau}{(1-t_0+\tau u)^2}+uf-uf^3\right] - t_0[f-f^3]=0 \quad (26a)$$

$$-\kappa^2\frac{d^2\alpha_0}{du^2}+\alpha_0 f^2+\tau u\alpha_0 f^2-t_0\alpha_0 f^2=0 \quad (26b)$$

Now the dimensionless order parameters f and α_0 need to be solved.

Also the boundary conditions need to be rewritten in terms of the dimensionless variables. This results in:

$$\frac{\mathrm{d}\alpha_0}{\mathrm{d}u}_{u=0}=-\frac{2\pi\xi_0}{\phi_0}\xi_0 B_0\equiv-\beta_0,\qquad \frac{\mathrm{d}\alpha_0}{\mathrm{d}u}_{u=\infty}=0$$

$$\frac{df}{du}_{u=0}=b,\qquad f(\infty)=1$$

All of this is derived in more detail in appendix E.

With the equations and boundary conditions rewritten, a numerical method to solve the problem needs to be found. First we remark that this is a boundary condition problem: at the two boundaries (u=0 and u=∞) the derivatives of the functions we seek (f(u) and α_0 (u)) are known.

To find a general method to handle this type of problem two books were consulted [18] and [19]. In these books, two methods where found for this type of boundary problem.

The first method is the so-called "shooting method". In this method, for 1 of the boundary points the known derivative is taken and the value of the function is guessed. Then the problem is integrated inwards form this boundary, with the starting values of the function and its derivative implemented in the differential equation itself. Finally, the solution is checked by going to the other boundary and checking if the value or derivative match up to the already known value or derivative there. If not, a new guess is made until the correct solution is found.

This trial and error method isn't preferable here because our problem consists of two coupled differential equations. For each try, one or both need to be changed to find the correct solution and the convergence towards the correct solutions is very slow.

The second method is based on solving a matrix of all function values on a discreet grid. This means that the differential equation is written out in its numerical form for each value f_i and α_i and this system of 2n equations is put into a matrix and solved with a linear solver routine

This doesn't work for this problem, because there are nonlinear terms in the differential equations.

Since no standard method was found in literature, a method was created to tackle this problem. This iteration method is described in detail in appendix F, but the result is given below:

$$f_i^{p+1\prime} = b + \sum_{j=0}^{i}\left[\left(\alpha_j^p\right)^2 f_j^p - f_j^p + \left(f_j^p\right)^3 - \tau\left[\frac{1}{1-t_0+\tau u_j}\frac{df_j^p}{du_j} - f_j^p\frac{1}{4}\frac{\tau}{\left(1-t_0+\tau u_j\right)^2} + u_j f_j^p - u_j\left(f_j^p\right)^3\right] + t_0\left\{f_j^p - \left(f_j^p\right)^3\right\}\right]\Delta u \tag{27a}$$

$$f_i^{p+1} = 1 - \sum_{j=i}^{N} f_j^{p+1\prime}\Delta u \tag{27b}$$

$$\alpha_i^{p+1\prime} = \beta_0 + \frac{1}{\kappa^2}\sum_{j=0}^{i}\left[\alpha_j^p\left(f_j^p\right)^2 + \tau u_j\alpha_j^p\left(f_j^p\right)^2 - t_0\alpha_j^p\left(f_j^p\right)^2\right]\Delta u \tag{28a}$$

$$\alpha_i^{p+1} = -\sum_{j=i}^{N}\alpha_j^{p+1\prime}\Delta u \tag{28b}$$

The superscripts "p" and "p+1" refer to successive generations of trial solutions.

For this method an initial function for f^0 and α^0 needs to be known. These are guessed based on the expected form of the functions shown in Figure 2.6.

This method in theory can be used straightforwardly. However, because the two functions are coupled and strongly non-linear the first try showed that the method was not stable. To compensate for the instability, numerical "damping" is applied: a percentage c of the new function and percentage (1-c) old function are combined to make the f function and same is done for α as seen below:

$$f = cf_{new} + (1-c)f_{old}, \qquad \alpha = c\alpha_{new} + (1-c)\alpha_{old}$$

This nest f and α values are again put into the numerical recipe and everything is repeated again. This process is then repeated until a small enough difference between f_{old} and f_{new} and between α_{old} and α_{new} is reached.

3 Experimental layout

3.1 Set-ups

3.1.1 Magnetic components

To avoid complications due to the earths magnetic field and various stray fields, all experiments where done inside a magnetic shielded room (Vaccumschmelze AK3B, 2.4x3x4m^3 [20]). In the centre of this room where the various shields are tested, the background field is measured to be <10nT.

For these experiments, two Helmholtz coils were used. A Helmholtz coil is a set consisting of 2 identical short solenoids of radius R placed parallel to each other at a distance R apart. This has the advantages that in the centre of the set field homogeneity is maximised, with both first and second derivative of B with respect to the axial direction zero [2].

The first Helmholtz coil has a diameter of 400mm and distance of 200mm between the coils. It has a field constant of 674μT/A. The second coil set consists of 2 "Helmholtz" coils one producing a field in the z-direction and the other one in the y-direction. The "Helmholtz" in the y-direction consists of two square-shaped coils with sides of 1444mm placed 1390 mm apart. The z-direction "Helmholtz" coil is made of two circular solenoids with diameter of 1720mm placed 1520mm apart. Their field constants were verified using a fluxgate (Bartington Mag-03), yielding 54.41μT/A in the y-direction and 97.86μT/A in the z-direction. Strictly speaking, these two coil sets are no Helmholtz coils. Nevertheless, we shall refer in the rest of the text to 3 coil sets as "small Helmholtz" (which will be used to create both horizontal and vertical fields); the "large vertical Helmholtz"; and the "large horizontal Helmholtz". The words 'vertical' and 'horizontal' will refer to the generated field direction.

A fluxgate is a device that consists of two coils wrapped around a ferromagnetic core. Through one of these coils an alternating current is put, producing an AC magnetic field in the core which in is sensed by the other coil. External DC fields are then detected by their influence on the non-linear magnetic susceptibility of the core [21]. Although these devices are robust, relatively simple in use and precise over a wide field range, they cannot be used at the cryogenic temperatures where we want to test our shields. Therefore, in this assignment the fluxgate is only used for background measurements and coil calibrations.

A power supply is used to drive the Helmholtz coils. Coil current is measured by a 0.1Ω shunt producing a voltage (in V) that is 10% of the current (in A). This voltage is amplified 10 times (Ectron model 560 amplifier) so the measured voltage is equal to the applied current. This is then read by a DAQ card (NI USB 6216) and processed with a labview program.

3.1.2 Measurement devices

Prior to this assignment, some work was already done to determine the magnetic shielding of the CryoPerm shield, using a Hall-probe (GaAs/AlGaAs probe, ChenYang Technologiesa, type HS80). The Hall constant for this probe was 1.256V/T at ambient temperature (300K) and 3.413V/T with the probe submerged in liquid nitrogen (77K). The noise floor obtained with this probe was in the order of ~4μT, which was too high for a detailed comparison with model results.

Therefore, for this assignments a three-axis SQUID sensor (models XYZ-WM02 Figure 3.1) is used. When rotated around the 2-axis, the x and y direction SQUIDS are ~5mm off-axis because they are placed on the sides of a cube. The SQUID sensors are controlled using a Star Cryoelectronics controller (model PFL-100) and read out by the program PCS100 Squidcontrol. Although the SQUID sensor offers a far superior sensitivity compared to the Hall probe, it is important to note that it cannot measure absolute field values. Once the feedback loop is locked, in principle field variations as small as <1pT can be detected, but the amount of flux in the SQUID loop prior to locking is unknown.

The basic layout of the SQUID electronics is shown in Figure 3.2. A feedback loop consisting of a feedback resistance and coil determines the range at which can be measured. The SQUIDs measure by keeping the magnetic flux through them constant; this is done with a feedback coil. The maximum readout of the feedback coil is ~6V with the resistance determining the range which can be measured (i.e. the lower the resistance the larger the range). The resistance can be set to the values 1, 10 or 100kΩ.

A problem that can occur is momentary loss of locking, during which the magnetic field inside the SQUID jumps to a different level. This has the effect that the SQUID now reads out a different voltage at the same applied magnetic field, causing the differential comparison to be lost. In principle this can be compensated for afterwards in the data files, but this is not a perfect solution so in most cases it is best to redo the measurements and to reset the SQUID.

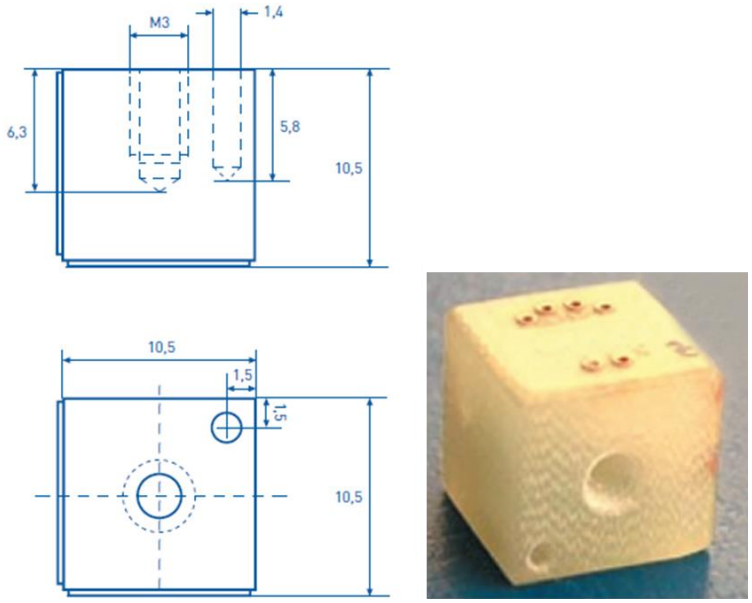

Figure 3.1 3-axis 3DGreen SQUID sensor dimension description

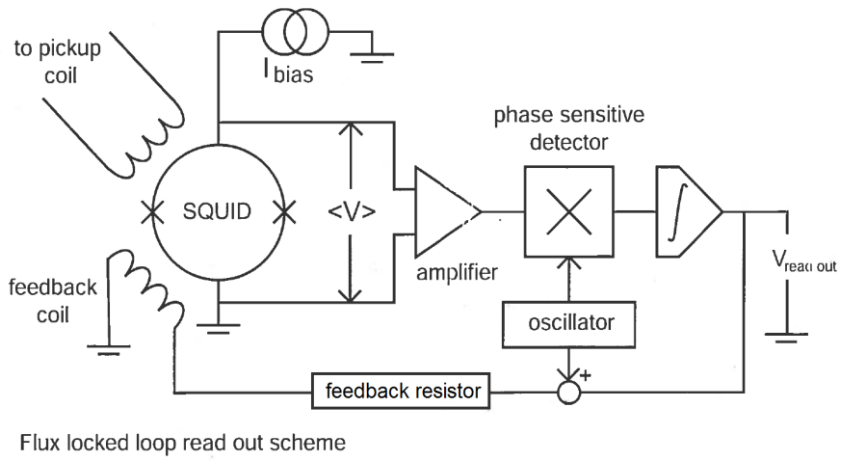

Figure 3.2 SQUID electronics overview

The first thing that needed to be done was to calibrated the SQUIDs for the CryoPerm measurements. For the calibration, both Helmholtz sets are used and the sensors are calibrated for two different feedback resistors (1kΩ, 10kΩ). The calibration for the x,y SQUIDs are only done with feedback resistance of 10kΩ. For these calibrations, the large horizontal Helmholtz was used. For the calibration of the z SQUID both the feedback resistance of 1kΩ and 10kΩ are used. For the calibration with the feedback resistance of 10kΩ, the large vertical Helmholtz is used. With the feedback resistance of 1kΩ the small Helmholtz is used. The SQUID constants found by the calibration are shown in Table 3.1.

Squid axis	Feedback resistance (kΩ)	Calibration (V/μT)
x	10	1.837±1%
y	10	-1.863±1%
z	10	2.044±2%
z	1	0.2078±2%

Table 3.1 calibration results SQUIDs for CryoPerm measurements

With these values the maximum measureable field can be determined. Taking the maximum readout voltage mentioned before (~6V) this gives a maximum measureable field in z-direction of ~30μT using the 1kΩ feedback resistor.

Between the CryoPerm and the Nb measurements, the wiring of the SQUID sensors was redone, so the SQUIDs needed to be recalibrated for the Nb measurements.

For the Nb measurements, only the feedback resistance of 10kΩ was used. First for the calibration of the x,y SQUID's the larger horizontal Helmholtz was used and second for the calibration of the z SQUID the larger vertical Helmholtz was used. This results in the SQUID constants as shown in Table 3.2.

Squid axis	Feedback resistance (kΩ)	Calibration (V/μT)
x	10	1.87±2%
y	10	-1.866±2%
z	10	1.958±2%

Table 3.2 calibration results SQUID's for Nb measurements

This then corresponds to a maximum measureable field of ~3μT for the Nb measurements.

3.1.3 Cryostat and insert

The experiments where done in liquid helium at 4.2K inside a fiber-glass reinforced epoxy cryostat. An epoxy cryostat is used instead of a metal to minimize magnetic interference caused by the cryostat. All measurements are done with the cryostat inside one of the Helmholtz coil sets, with both the coil and the cryostat placed inside the magnetically shielded room.

For the experiments, the height of the SQUID sensor needs to be varied with respect to the shield. This is achieved by attaching the squid sensor to a hollow G10 tube (l 880mm; ϕ_i 16mm) which can slide inside a second hollow G10 tube (l 605mm; ϕ_i 22mm). On top of the smaller tube, the SQUID electronics are placed. At the bottom of the outer tube a support ring (l 5mm; ϕ_i 51mm) is fixed and the shield is attached below that ring. This configuration makes it possible to move the SQUID sensor compared to the shield by moving the SQUID electronics. A second advantage of this configuration is that it allows the SQUID sensor to be rotated around the axis of the shield. A third advantage is that the ring slides into the tail of the cryostat, so that the insert does not vibrate easily. A schematic description of the setup is shown in Figure 3.3.

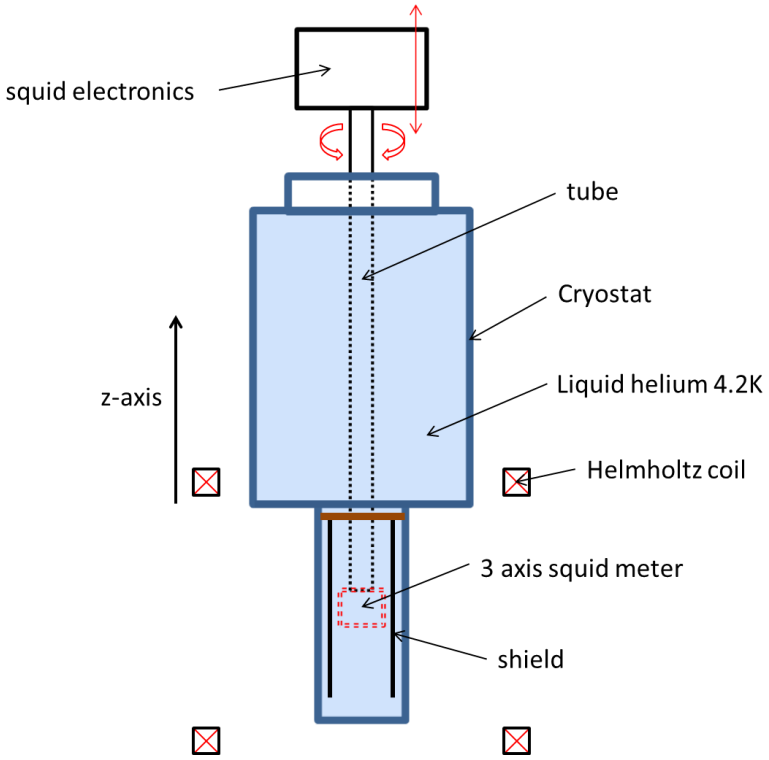

Figure 3.3 sematic description setup

For some of the experiments, the height of the SQUID sensor needs to be continuously measured. This is achieved by fixing a block with a treaded hole to the SQUID electronics. Inside this block, a nylon rod with a tread is screwed with the bottom of the rod resting on the top flange of the cryostat. When the nylon rod turns, the SQUID electronics moves up and down compared to the cryostat (which causes the SQUID sensor to move up and down compared to the shield). A potentiometer on top of nylon rod measures the number of rotations of the nylon rod. So with the distance per rotation known (2mm per rotation), the height can be measured. This gives a setup as shown in Figure 3.4.

For this continuous height measurement, the output of the potentiometer is read by a DAQ card and processed with a labview program.

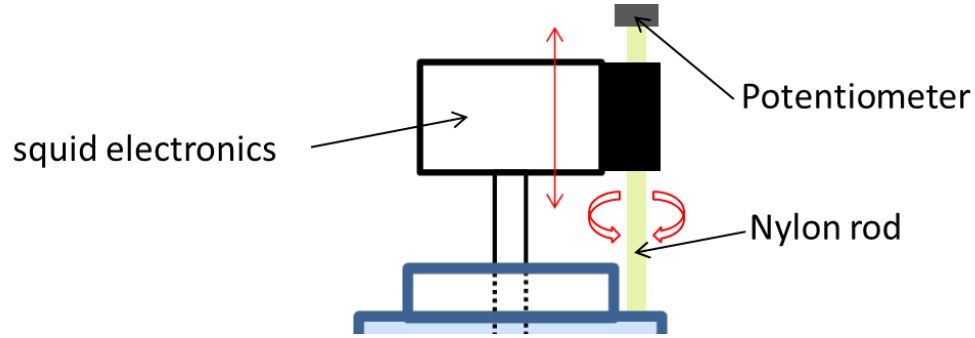

Figure 3.4 setup for potentiometer height measurement

For some experiments, field needs to be measured off-axis from the central z axis. For this, at the bottom of the insert where the SQUID sensor is attached to the smaller G10 tube, a horizontal extension is constructed. With this extension, the SQUID sensor can be mounted 20 mm off-axis in the radial direction. This setup is shown in Figure 3.5.

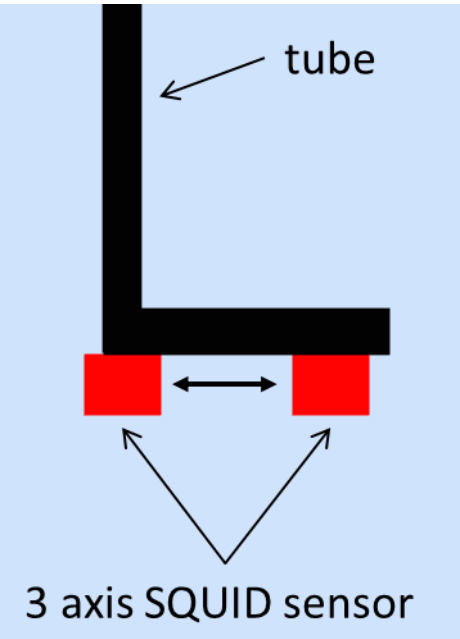

Figure 3.5 setup for moving SQUID sensor 20mm off axis from the central z-axis

3.2 CryoPerm shield

3.2.1 Description CryoPerm shield

The CryoPerm shield consists of two concentric cylinders made of CryoPerm which are clamped together by two Teflon collars to keep them in place (Figure 3.6). The dimensions of the cylinders are shown in Table 3.3. It should be mentioned that both CryoPerm cylinders have a weld in them along the z-direction. These 2 welds where placed on top of one another during the experiments to see if an effect of the weld could be measured.

	Inner diameter (mm)	Length (mm)	Wall thickness (mm)
Inner cylinder	34	130	0.5
Outer cylinder	41	165	1

Table 3.3 CryoPerm cylinders dimensions

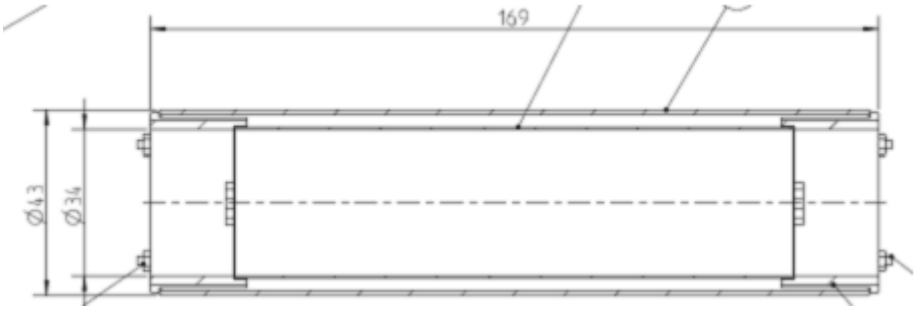

Figure 3.6 shield assembly with CryoPerm cylinders clamped between Teflon collars

3.2.2 Demagnetization procedure CryoPerm shield

Multiple times the CryoPerm shield needs to be demagnetised. This is done by disassembling the shield and demagnetizing the two cylinders separately. The demagnetization is carried out inside the magnetic chamber to make sure that a minimal ambient field is present during demagnetization. For the inner cylinder, 10 turns of insulated Cu wire are wound through the bore of the cylinder. This wire is then fed with a 0.2Hz sinusoidal current, with an initial amplitude of 2.64A. This corresponds to an initial magnetic field of H=200A/m on the cylinder. Following a strategy as described in paragraph 1.1.4, this current is reduced by 5% per wave until it reaches a minimal amplitude of 5mA

(H=0.38A/m). This minimum is because of noise from the combination of the function generator (Agilent 33120A) and the power supply (The Boss 20Volt-20Amp, Electronic Measurement Inc.). The same thing is done for the outer cylinder. Again 10 turns of insulated Cu wire are wound through, only this time an initial amplitude of 2.17A is applied, again corresponding to an initial magnetic field of H=200A/m on the cylinder. Once more the current is then decreased until a current of 5mA (H=0.42A/m) is reached.

3.2.3 Previous work on CryoPerm shield with Hall sensor

For this assignment, first a comparison needs to be made with previous work done on the CryoPerm shield. These experiments were done in a Styrofoam bucket, either at room temperature or filled with liquid nitrogen. Here a magnetic field with a triangular wave shape with an amplitude of 1mT was applied in z-direction. A Hall probe was used to measure the magnetic field at different z positions in the shield. An example of one the measurement series is given in Figure 3.7. Note that the top of the shield assembly is at z=82.5mm (Figure 3.6).

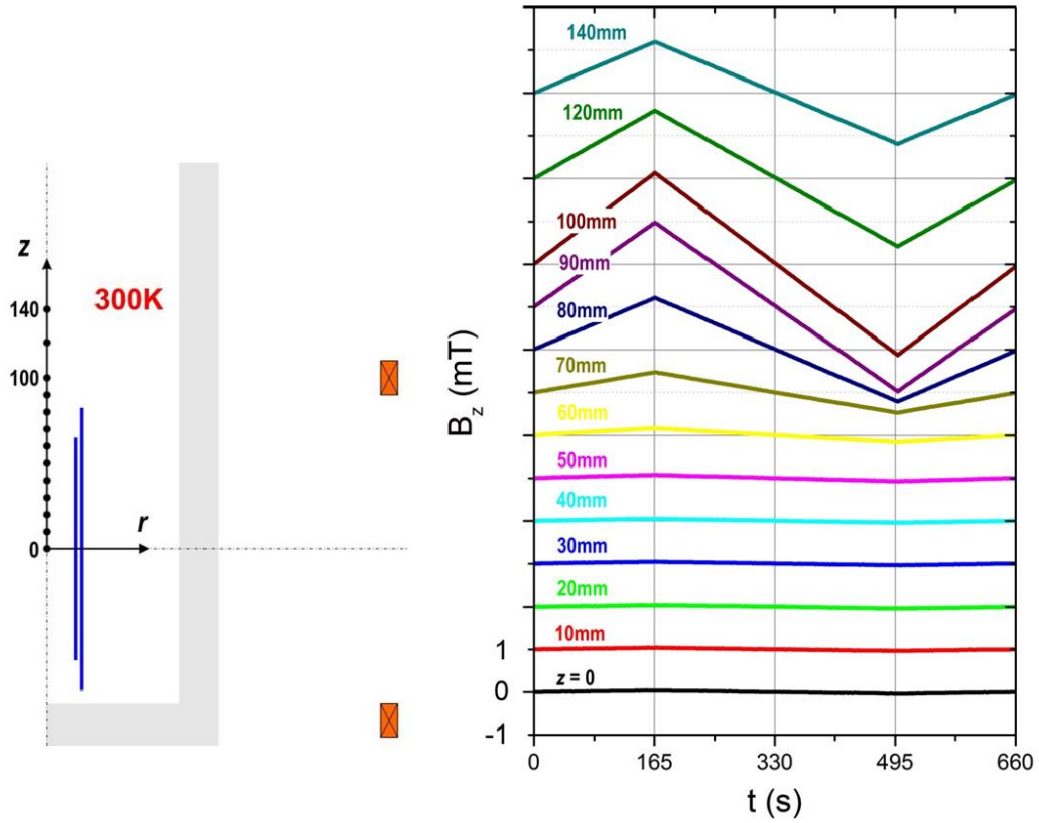

Figure 3.7 previous work done on CryoPerm shield, a triangular wave applied with amplitude of 1mT, seen at different z positions

It is observed that the amplitude of the magnetic field decreases as one descends deeper inside the shield. This amplitude is then used to determine the shielding factor.

This earlier work was not conclusive because the measurements needed also to be done at lower temperatures. Furthermore, the Hall probe had a problem measuring the magnetic field in the middle of the shield (z=0) because the measurement noise was too high (~4μT), so a measurement device that can measure lower values was needed.

3.2.4 Measurement plan CryoPerm shield

First the measurements form the earlier work described above are repeated at 4.2K with the SQUID sensors. An axial AC magnetic field is applied and measured on-axis at different z positions. The magnetic field with a triangular wave shape is applied with an amplitude of 100μT in the z-direction and the measurements were done at a temperature of 4.2K. The lower amplitude compared to the previous works is chosen because the z SQUID has a maximum measureable amplitude of ~30μT in the z-direction, so if a field of 1mT would be applied very little measurement points in z would be below the 30μT. The results are then compared to earlier Hall probe results and to a FEM model.

The second measurement concerns the attenuation factor at the centre of the shield with different magnetic field amplitudes applied in z-direction. First the shield needs to be demagnetized, as described in paragraph 3.2.2. Next an external AC field is applied in the z-direction with an amplitude of 1μT and the attenuated magnetic field is measured at z=0. After this, the amplitude is increased somewhat and the procedure repeated. This process is repeated until an amplitude of 100μT is reached. These results are used to study the effect of remanence.

The third measurement is the phase difference of an AC applied magnetic field in z-direction, compared to the measured magnetic field at centre of the shield. This is then repeated for different frequencies of the applied magnetic field. The goal is to determine the frequency at which eddy currents become negligible. This is used to determine below which frequency the measurements and demagnetization procedure need to be done.

The fourth measurement is the effect of remanence over the central z axis. First the magnetic field is measured along the central z axis for a demagnetized shield with no external field applied. Then a field excursion of 100μT is applied in z-direction (and brought back to zero). Next, the magnetic field is once more measured along the central z axis. Also these results are specifically aimed at studying the effect of remanence.

The last measurement is the effect of remanence and the weld at the centre of the shield. First the magnetic field is measured at the centre of the shield over different angles for a demagnetized shield with no external field applied. Then again a field excursion of 100μT is applied in z-direction. Finally, the magnetic field is measured again at the centre of the shield over different angles. These results are used specifically to look at the effect of the welds on the CryoPerm cylinders, that have been aligned as discussed above.

3.3 Nb shield

3.3.1 Description Nb shield

Nb is a type II superconducting material with a critical temperature of 9.2K, the highest known critical temperature for elemental superconductors. It is important to note that the superconducting properties of Nb are dependent on the purity of Nb [22], so damage to the shield could cause problems.

The superconducting Nb shield consists of two parts: a top “tube” and a bottom “lid”. To construct the shield, the top tube is slid over the bottom lid. This has the disadvantage that it creates a small gap between the two parts where they overlap. The configuration of the shield and its dimensions are shown in Figure 3.8.

a) b)

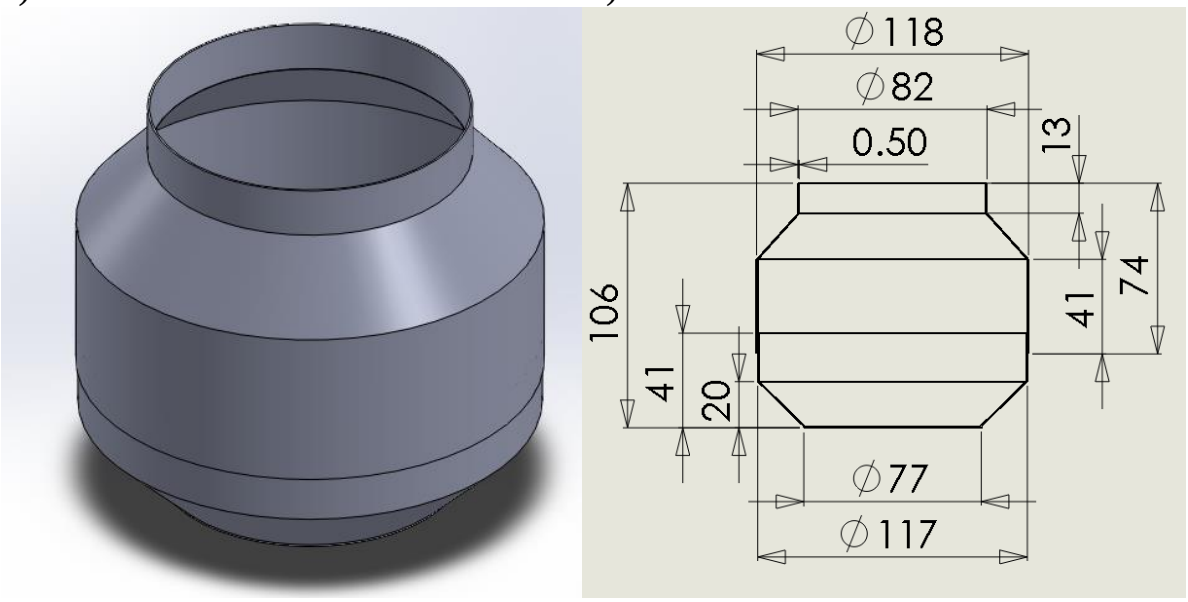

Figure 3.8 description of the Nb shield, dimensions in mm, the overlap between the top tube and bottom lid 9mm, a) overview, b) cross-section

The parts of the shield where made using a technique called deep drawing. Deep drawing is a technique were a plate of material is placed on top of a mold. Then a press a applied to the material to press it into the mold. This results in the material having the same shape as the mold. This technique has the advantage that no welds are present in the parts, but it has the disadvantage that stress is put on the material to press it into the mold which could lead to material dislocations and surface defects.

3.3.2 Demagnetization procedure Nb shield

In this assignment the Nb shield needs to be demagnetized. This is simply done by heating it up above 20K while still inside the cryostat inside the magnetically shielded room. 20K has chosen since it is well over the critical temperature of Nb (T_c=9.2K). To do, this first the shield is brought out of the liquid helium. Then the shield is heated with a heater placed around the region where the 2 parts overlap in Figure 3.8. To determine if the material has indeed reached a temperature above 20K, 2 thermometers were placed on the shield: one on the top and one on the bottom part. When these reach a temperature above 20K the heater is turned off. Then the shield is again brought into the liquid helium and allowed to cool down below its critical temperature. During this cool-down, it should be made sure that no field is present so that no flux trapping occurs.

3.3.3 Measurement plan Nb shield

All measurements are done with a 9mm overlap between the top tube and bottom lid.

The first measurement is the attenuation along the z-axis, with at magnetic field applied in the z-direction. First the shield is demagnetized as described in paragraph 3.3.2. Then a point must be taken while no field is present. This is needed to have a zero field reference point since, as discussed above, the SQUIDs measure differentially. Now an external magnetic field of 10μT is applied in the z-direction and the magnetic field profile is measured along the central z-axis. These results will compared it to a FEM model.

The second measurement is the attenuation along the z-axis with an external magnetic field applied in the radial direction. Again the shield needs to be demagnetized first so that no flux trapping is present. Once more, a reference point must be taken with no field present. Then a magnetic field of 10μT is applied along the x-axis and the magnetic field is measured along the central z-axis. Also these results are compared to a FEM model.

The third measurement concerns the magnetic field at certain z points and at different angles with a magnetic field applied in the x-direction. Now the SQUID sensor is 20mm off-axis as shown in Figure 3.5. Again the shield needs to be demagnetized so no trapped flux is present. First, the SQUID sensor is placed 40mm below the top of the shield. Then a reference point is taken at certain angle (α=0) with no field present. Next an external magnetic field of 10μT is applied in the x-direction. Then the SQUID sensor is rotated 360 degrees around the shields central axis and the magnetic field is measured at certain angles (Figure 3.9). The same experiment is repeated a second time with the SQUID sensor 80mm below the top of the shield. Since it was feared that feedback loop unlocking as described in paragraph 3.1.2 would not be so obviously detectable here, the experiment was repeated with a field of 1μT applied in x-direction. Also these results are compared to a FEM model.

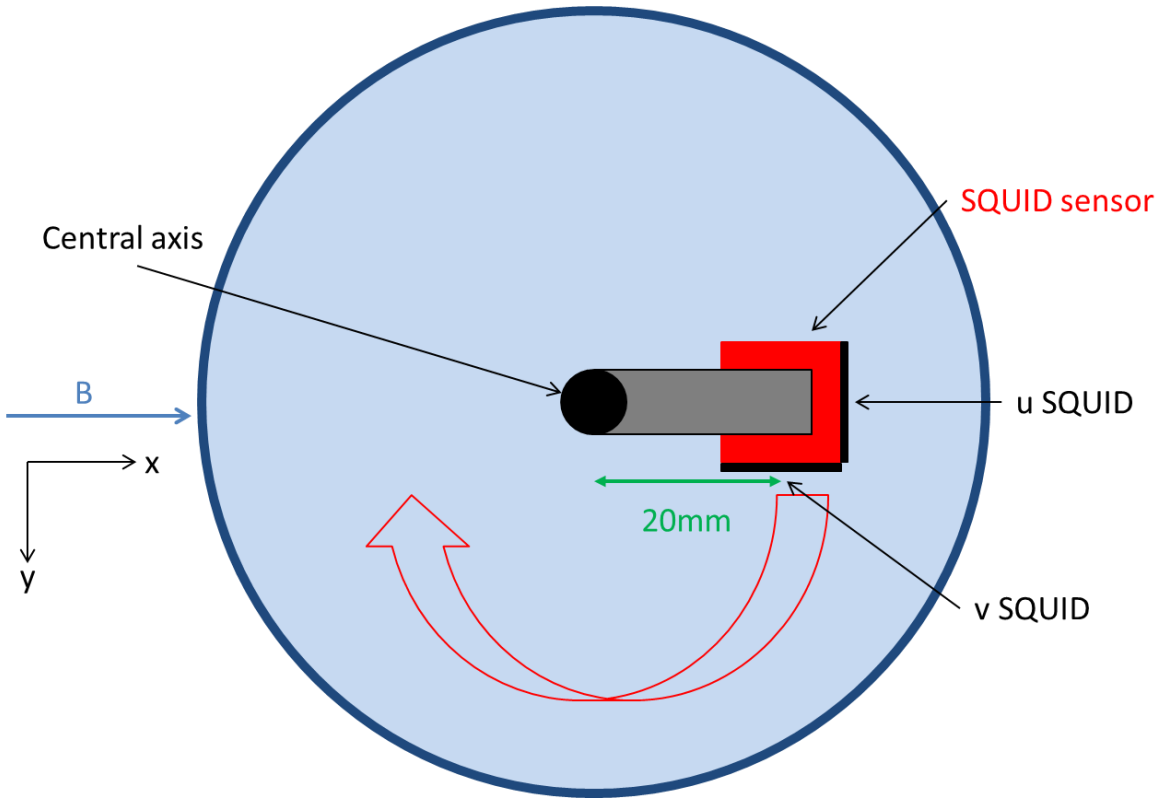

Figure 3.9 top view setup for when the SQUID sensor is 20mm off-axis with a magnetic field applied in x direction at α=0

The fourth measurement is of the phase difference and the attenuation of a AC applied magnetic field in z-direction. Here the SQUID sensor is again 20mm off-axis (R=20mm), kept on a constant angle (α=0) and demagnetized. Then the SQUID sensor is placed 80 below the top of the shield, after which a sinusoidal magnetic field is applied in the z-direction with an amplitude of approximately 1μT and a frequency of 0.1Hz. The magnetic field is then measured and compared to the applied field to determine the phase difference and attenuation. This is repeated in steps for higher frequencies until 3kHz is reached. Then the experiment is repeated for an amplitude of approximately 10μT, but now only up to a maximum frequency of 300Hz. These result are used to study the effect of frequency on the attenuation factor of Nb shield.

The last measurement is to look at remanence. First the magnetic field is measured over the central z-axis with no field applied, but here geometrical flux trapping is created by applying a magnetic field in the z-directions while cooling down. To achieve this, first the shield is heated up as described in paragraph 3.3.2. Then a magnetic field of 1μT is applied in z-direction and the shield is cooled down below its critical temperature while the field is still present. This should give flux trapping as described in paragraph 2.2.3. Finally, the external magnetic field is turned off and now the remanent magnetic field is measured over the central z-axis. This is then repeated for different magnetizing fields of 0T, 10μT and 100μT. These results are used to study the remanence of the Nb shield.

4 Results

This chapter forms the core of the report. The results of the experiments described in chapter 3 are presented, and compared to the models discussed in chapter 2. As mentioned in the introduction, the goal is especially to validate the FEM models as design tool, but also to asses where they break down due to effects of remanence. Paragraph 4.1 will discuss the shielding factor and remanence of a CryoPerm shield assembly, paragraph 4.2 presents similar data obtained with the deep-drawn Nb shield. paragraph 4.3 finally, is somewhat different: it presents the results of the GL calculations of the field- and other parameter profiles in presence of a temperature gradient and thus forms a first attempt to verify the hand-wavy relation concerning flux pinning during cool-down in presence of disorder.

4.1 CryoPerm shield

In the present section, the experimental data on the double CryoPerm shield (Figure 3.6) are compared to FEM and number of simple analytical models. Paragraph 4.1.1 concentrates on the shielding factor, which was measured on-axis as function of depth inside the shield, external field amplitude and frequency. In paragraph 4.1.2 the effects of remanence are presented in more detail. The remanent field is measured as function of axial position before and after an external field excursion, and also as function of orientation with respect to the axial weld in the shield assembly.

4.1.1 Magnetic shielding CryoPerm shield

First, the profile of the axial component of the magnetic field along the (z)-axis of the double walled CryoPerm assembly is measured here. z=0 represents the centre of the shield. An external AC magnetic field is applied in the axial direction with a triangular wave shape, a frequency of 0.1Hz and an amplitude of 100μT. The measurements are done with the SQUID sensor. They are compared to the previous experiment done with a Hall probe, as explained in paragraph 3.2.3, and with a FEM model of the shield with an applied axial field of 100μT and the "magnetic insulation" boundary condition ($B_{\parallel} = 0$). All results are shown in Figure 4.1.

a)

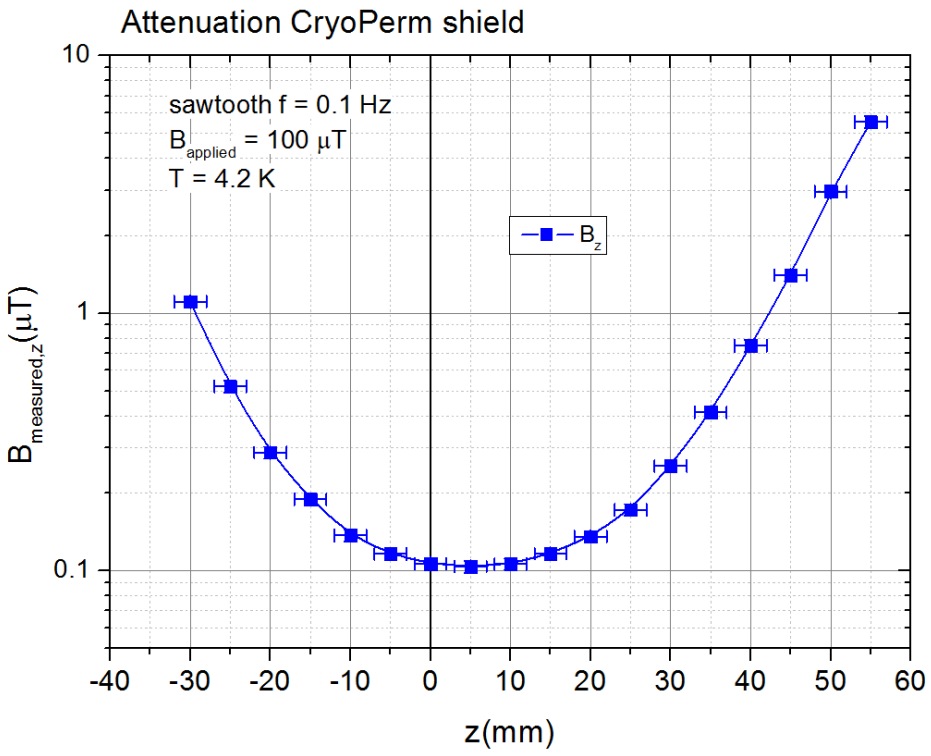

b)

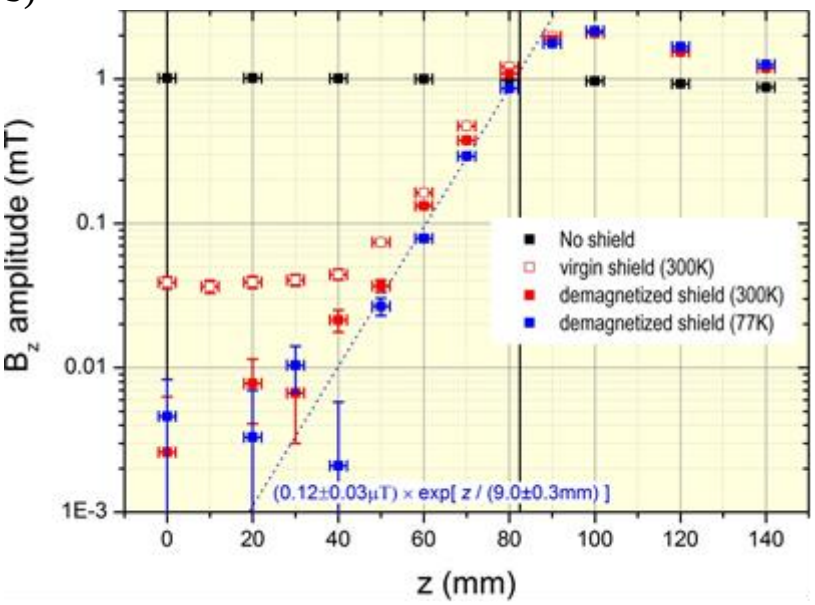

c)

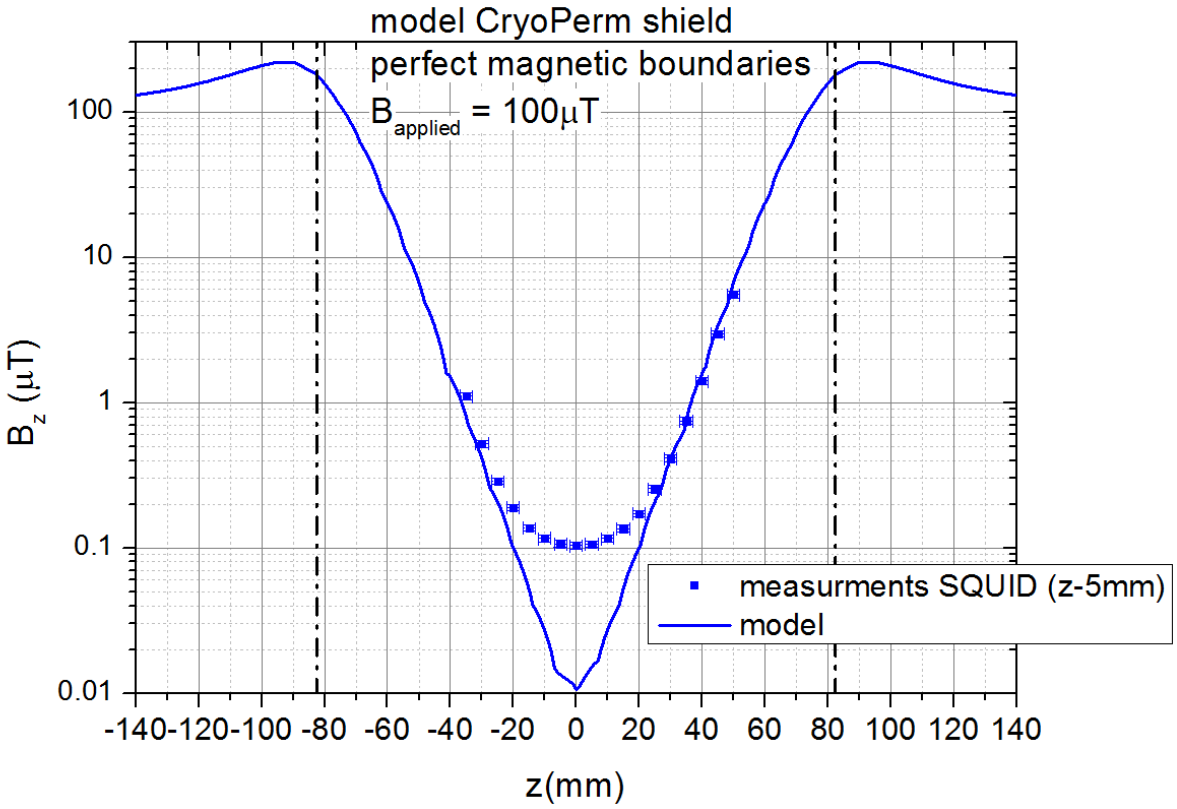

Figure 4.1 shielding of an AC magnetic field applied in z-direction with an amplitude of 100μT and frequency 0.1Hz, z=0 is the centre of the shield, a) z-component of the field, measured with the SQUID sensor, b) previous measurements with Hall probe, black line indicates the edge of the shield not that the applied amplitude was higher than for the SQUID measurements, c) full: solid line model prediction with perfect magnetic boundaries ($B_{\parallel} = 0$), squares results SQUID measurements translated 5mm to the left, dash dot line indicates the edge of the shield

The maximum measurable field of the SQUID (see paragraph 3.1.2) necessitated a difference in the amplitude of the applied magnetic field between the SQUID measurements (amplitude=100μT Figure 4.1a) and the previous measurements with the Hall probe (amplitude=1mT Figure 4.1b). So that they cannot be compared directly in terms of absolute field values. In the SQUID data (Figure 4.1a) there is a clear plateau around the centre of the shield, with a minimum value a little off-centre

(z=5mm). This offset is assumed to be a measurement error. This minimum value gives a maximum shielding factor of approximately ~970, i.e. just below the shielding factor of 1000 needed in the Athena mission. Looking at the previous measurement (Figure 4.1b) it is seen that the magnetic field reaches a maximum just outside the edge of the shield and then decreases again to the applied value. These results are compared to the model (Figure 4.1c). To compare the SQUID measurements with the model the measured data need to be moved 5mm to the left, in order to negate the off-axis mistake mentioned above. It is observed that the minimum value seen at Figure 4.1a) is a lot lower in the model but the point where the field profile goes through 1μT is approximately the same (z=35mm).

Next, the attenuation is studied as a function of applied field amplitude. First the shield is demagnetized as described in paragraph 3.2.2. Then an AC magnetic field is applied in z-direction which has a triangular wave shape with a frequency of 0.1Hz and an amplitude of 1μT. The magnetic field in the z-direction is measured at centre of the shield (z=0). Then the amplitude of the applied field is increased and the procedure is repeated. This is done until an amplitude of 100μT is reached. The results are given in Figure 4.2

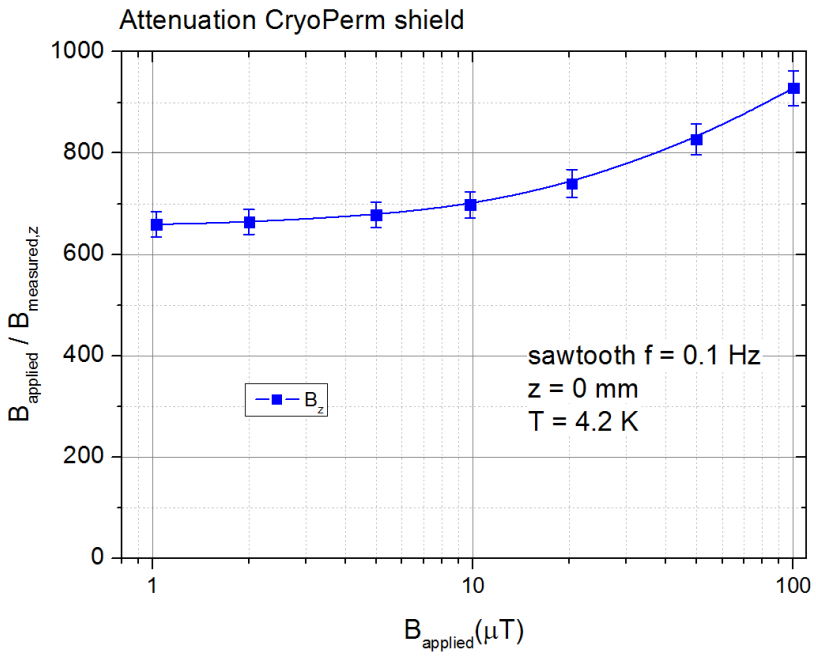

Figure 4.2 attenuation factor against applied AC field, the AC field is a triangular wave with frequency 0.1Hz, SQUID sensor positioned in the centre of the shield z=0

From these results it is observed that the attenuation factor increases with increasing amplitude of the applied field. Presumably, this is an effect of the remnant magnetization of the shield. "A dynamic susceptibility can be defined as $\chi_{m,AC} \equiv \frac{dM}{dH}$. Referring to Figure 1.6, if the shield is magnetized the slope of the M(H) curve around the point H=0; M=M_r will be low for low H-amplitudes, effectively causing a relatively low value of μ=1+χ_m. As the amplitude of the H increases, a larger part of the M(H) loop is sampled, effectively increasing μ and therefore yielding better shielding".

Next, the phase difference between the applied and measured field at different frequencies is studied. An AC magnetic field is applied in the z-direction as a sine wave with a frequency of 1Hz and an amplitude between ~75μT and ~95μT. Ideally, the amplitude would have been kept constant, but the frequency dependence of the amplifier made that impossible. Measurements are taken at the centre of the shield (z=0) using a oscilloscope and the phase difference is determined directly from the oscilloscope screen. Now the frequency is increased and the procedure repeated. This is done until a frequency of 100Hz is reached. The results are shown in Figure 4.3.

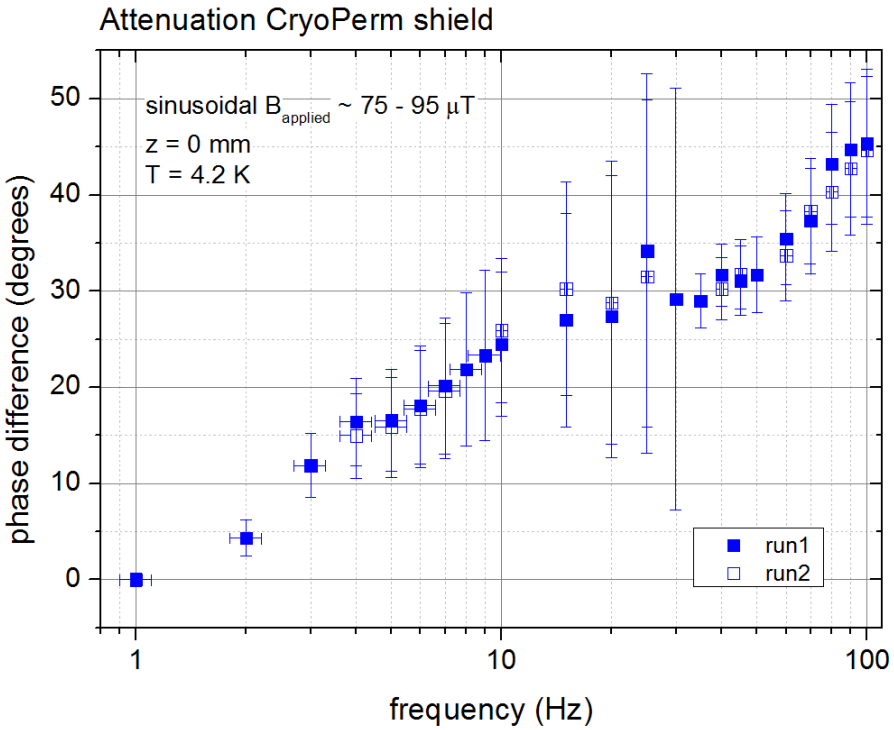

Figure 4.3 phase difference against frequency of a magnetic field with a sine wave and an amplitude between 75µT and 95µT, solid symbols first run, open symbols second run

It is observed that the phase difference increases increasing frequency. Below ~1Hz, the phase difference is virtually zero. From this it is concluded that there are no significant eddy current present inside the shield below 1Hz, as explained in paragraph 1.1.3.

4.1.2 Remanence CryoPerm shield

In this paragraph, the effect of remanence of the CryoPerm shield is studied. First the shield is demagnetized as described in paragraph 3.2.2. The magnetic field is then measured in all directions with the SQUID sensor moving along the z-axis, using the potentiometer setup shown in Figure 3.4. Then a field excursion of 100µT is applied in the z-direction (i.e. the external field is ramped to 100µT and then back to zero). Now the magnetic field is again measured along the z-axis in all directions. Noting that the SQUIDs do not allow absolute field measurements (see paragraph 3.1.2), we arbitrarily take a reference point (i.e. we put "B=0") at z=140mm. This gives the results as shown in Figure 4.4.

a)

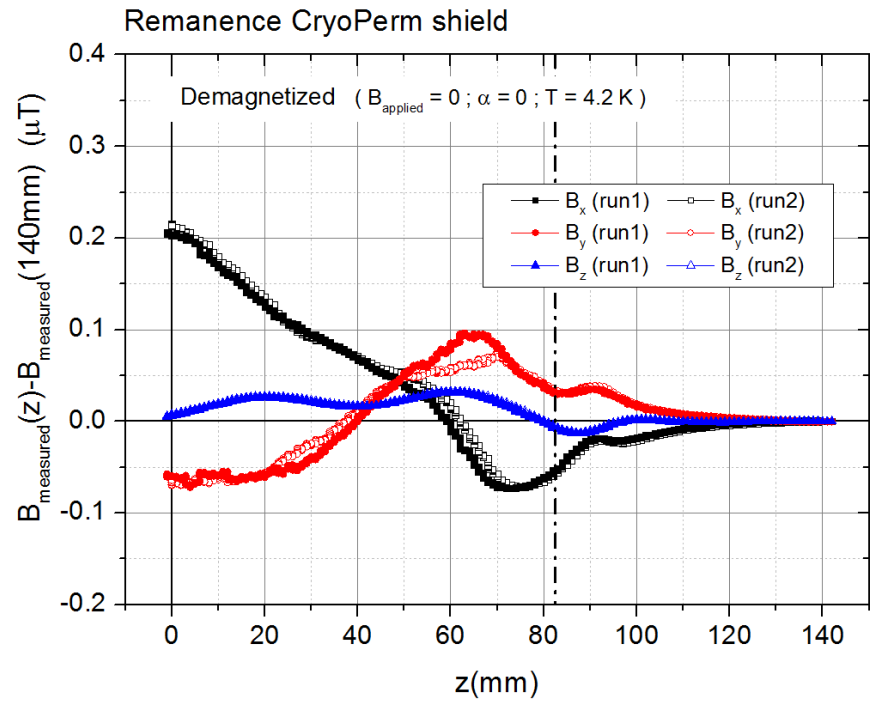

b)

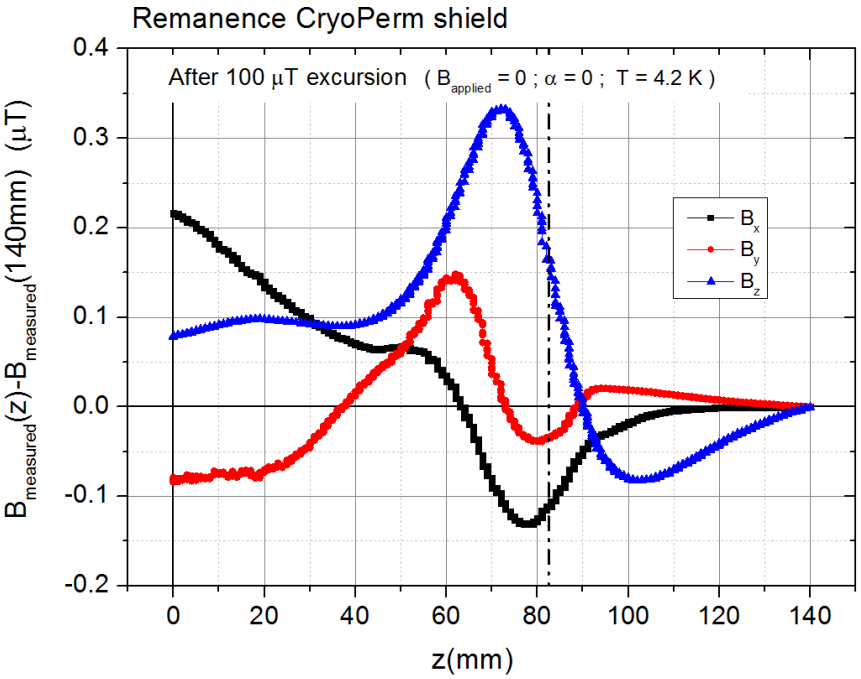

Figure 4.4 the dash dot line is the edge of the shield, black square Bx, red ball By, blue triangle Bz, solid symbols first run, open symbols second run, a) demagnetized shield, b) after excursion of 100μT

It is observed that the excursion of 100μT has an effect on all 3 components of the measured magnetic field. The CryoPerm shield is now magnetized so remanence is present. Using the observation of paragraph 1.1.1 that a magnetization of a material can be described as a surface current, a model of the magnetized CryoPerm shield is made. First it is assumed that the 2 CryoPerm cylinders that form the shield are equally magnetized in the same direction. Then the magnetization of the cylinder is described as sheet currents over the surface, with the current on the inner surface flowing in the opposite direction from the one on the outer surface, as described in paragraph 2.2.1. This results in a model as shown in Figure 4.5.

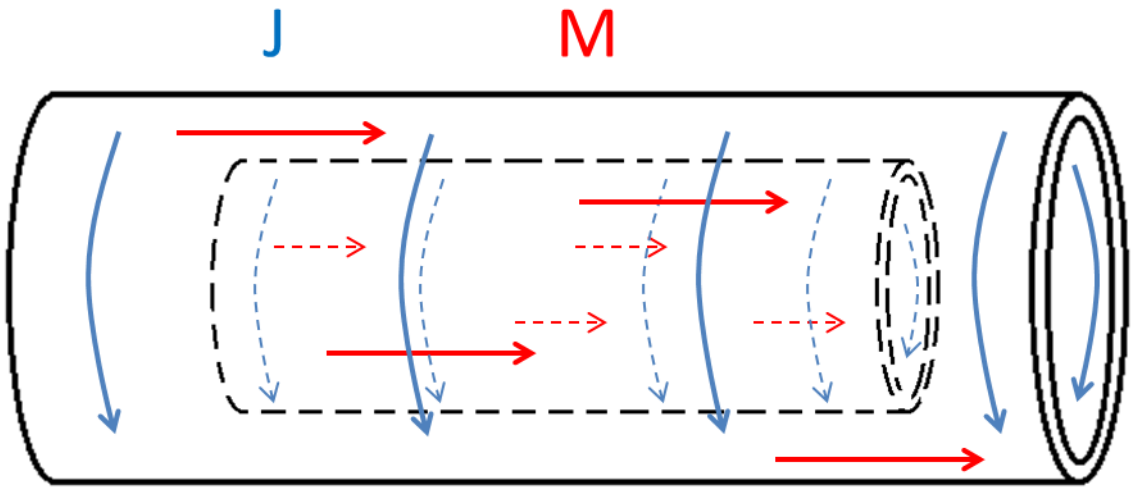

Figure 4.5 model magnetized shield with both cylinders magnetized same direction, red arrow magnetization, blue arrow current, solid line outer cylinder, dashed line inner cylinder

The analytical model for a magnetized cylinder (paragraph 2.2.1) allows to describe this problem. This equation is used to model a cylinder which is magnetized in the z-direction:

$$\bar{B}(r=0,\theta,z)=\frac{\mu_0 K}{2}\left[\frac{z+h_c}{\sqrt{(z+h_c)^2+{R_i}^2}}-\frac{z}{\sqrt{z^2+{R_i}^2}}-\left(\frac{z+h_c}{\sqrt{(z+h_c)^2+(R_i+d)^2}}-\frac{z}{\sqrt{z^2+(R_i+d)^2}}\right)\right]\hat{z} \quad (18)$$

Since the shield is made of two cylinders, equation (18) needs to be used to model both the cylinders individually after which they are simply added up. For the final result the values from Table 3.3 are implemented into this equation and this gives the model result for the values of the axial field component along the central z-axis of the CryoPerm shield magnetized in the z-direction.

The analytical approach leading to (19) is only valid on-axis. For a model for the field in the x,y direction, a Comsoll model must be made as described in paragraph 2.2.2. Here the magnetization of the shield is again described as a current over its surface, but now the magnetic field needs to be measured 5mm off axis because the x,y SQUID's measure 5mm off axis as described in paragraph 3.1.2. In the model it is again assumed that shield is magnetized in the z-direction and that the 2 cylinders of the shield are magnetized in the same direction. The results of these models are given in Figure 4.6.

a)

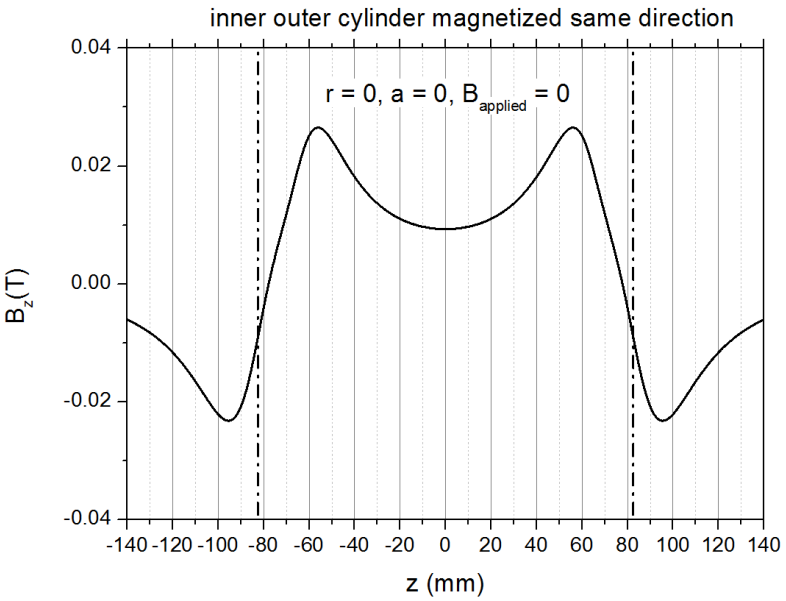

b)

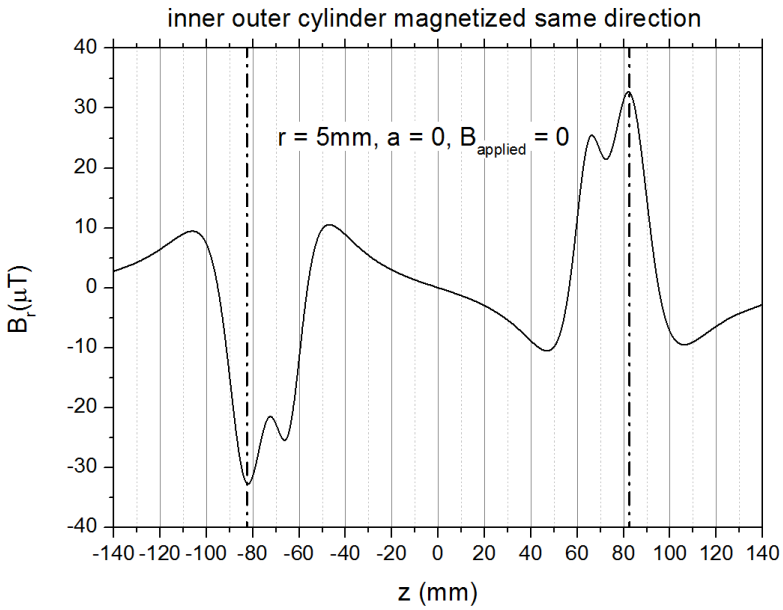

Figure 4.6 magnetic field with equal magnetization in the same direction for both cylinders, the dash dot line is the edge of the shield, a) Bz on r=0, b) Br on r=5mm

When Figure 4.6a is compared to Figure 4.4b, it is observed that the peak positions are not on the same place. Qualitatively, when Figure 4.6b is compared with Figure 4.4b, it is observed that they have different shapes. Presumably, this arises from the assumption that the cylinders are equally magnetized. To create a correct model, a different magnetization between the outer and inner cylinder needs to be assumed. This is done by using the analytical model from equation (18) to plot the peak positions of the minimum and maximum peak compared to the magnetization of inner cylinder over magnetization outer cylinder. From Figure 4.4b it is observed that the maximum peak for the magnetic field in the z-direction is approximately at 72mm and the minimum peak at 102mm. This is implemented into this plot which is shown in Figure 4.7.

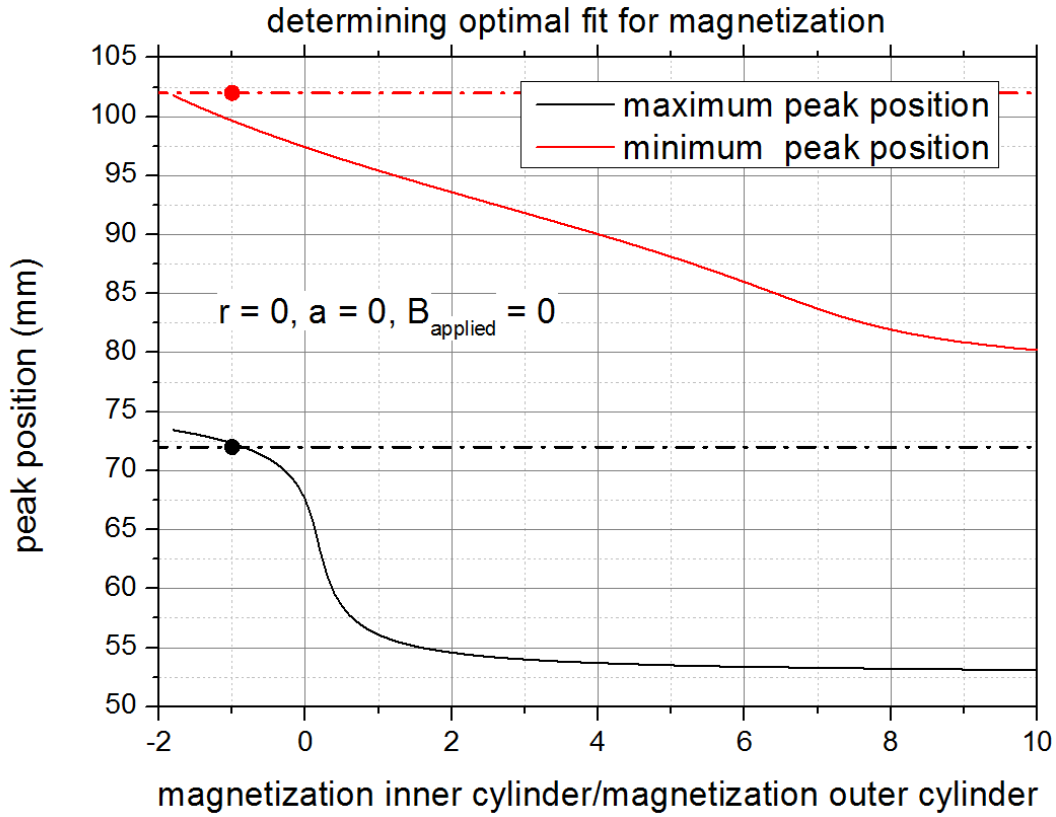

Figure 4.7 peak position of Bz over z-axis with r=0 over magnetization factor, black maximum peak, red minimum peak, dash dot line peak position from Figure 4.4b, points peak position at magnetization factor -1

From Figure 4.7 it is observed that the correct peak positions are found when the inner cylinder has approximately the same magnetization as the outer cylinder, but in the opposite direction.

The previous models are calculated again, but this time the magnetization of the inner cylinder in the opposite direction. The results corresponding to this new situation are given in Figure 4.8.

a)

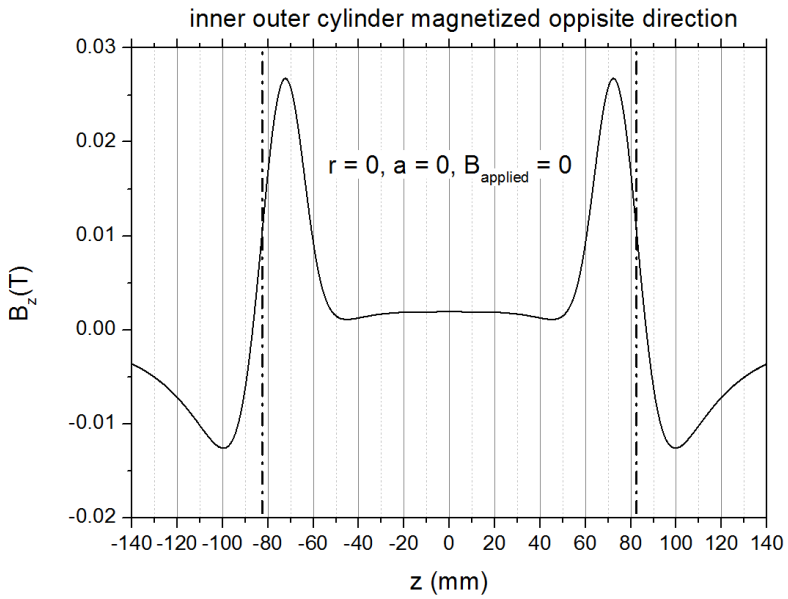

b)

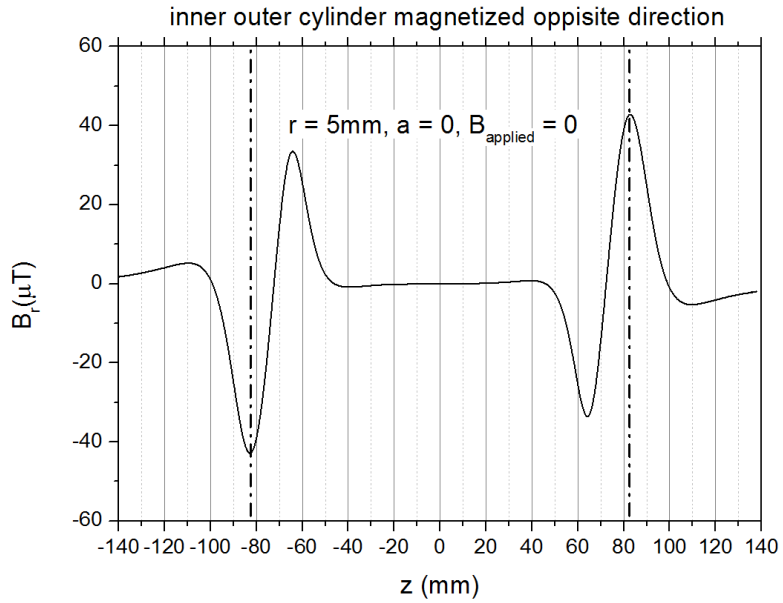

Figure 4.8 magnetic field with equal magnetization in the opposite direction for both cylinders, the dash dot line is the edge of the shield, a) Bz on r=0, b) Br on r=5mm

When Figure 4.8b is compared to Figure 4.4b, they have approximately the same shape and the peak positions are approximately on the same place. So these models seem to indicate that the CryoPerm cylinders in the CryoPerm shield become magnetized in opposite directions. Why and how this happens in reality was not tested.

Another effect of the remanence of the CryoPerm shield is the orientation of the remanent field and especially the effect the weld has on the remanence. This is measured at the centre of the shield (z=0). The welds of the two CryoPerm cylinders are aligned with one another at a fixed position. This position corresponds to the y SQUID pointing approximately at 225 degrees. First the shield is demagnetized, as described in paragraph 3.2.2. Then the magnetic field is measured in all directions at centre of the shield (z=0) while the SQUID sensor is gradually rotated 360 degrees around its central axis. Next an excursion of 100μT is once more applied in z-direction. The magnetic field is again measured in all directions at centre of shield (z=0) while rotating 360 degrees around

central axis. The reference point (B=0) is taken as the mean of the entire function. The results are shown in Figure 4.9.

a)

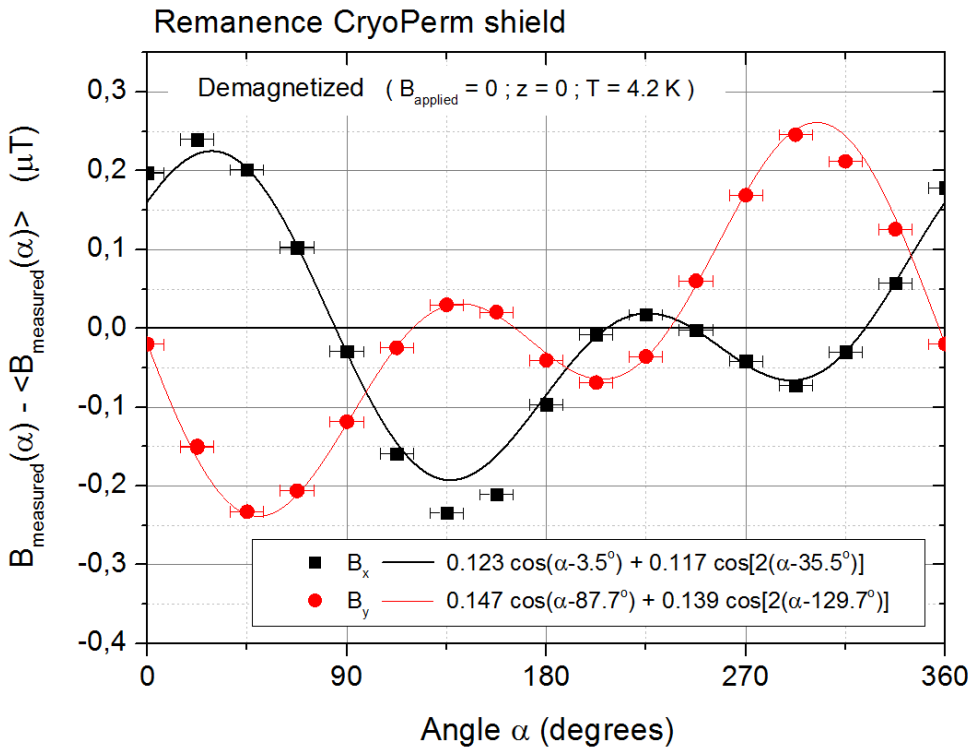

b)

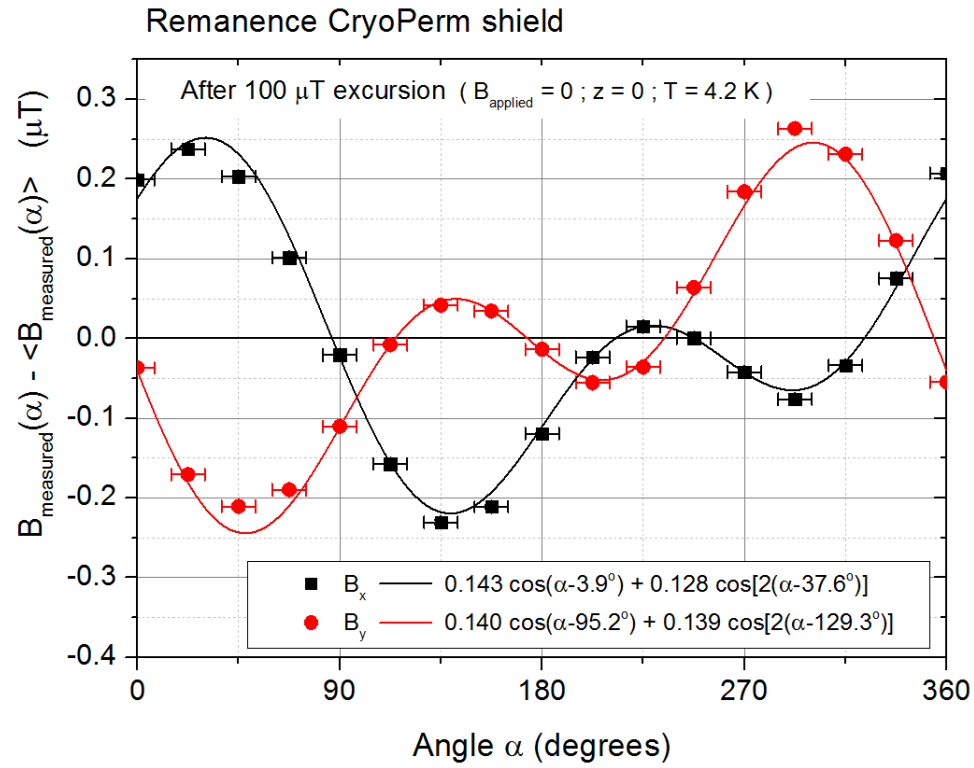

Figure 4.9 line is fit when only a dipole and quadrupole are present in the magnetic field, a) demagnetized shield, b) after excursion of 100μT

From these results, it is observed that the magnetic field at the centre of the shield (z=0) seems to be unaffected by the excursion of 100μT, since no clear difference in value or shape is seen.

Also, the shape of the $B_{x,y}(\alpha)$ profiles is surprising. It was expected to observe a homogeneous field, generated by a "dipole" type of remanent magnetization current. But the measured shape has the form of a "dipole/quadrupole" combination. This new shape is assumed to be an effect of the weld and this is further tested via a simple model. The magnetic field and current distribution of a dipole and quadrupole shape are illustrated in Figure 4.10. So now for the model a fit of a mixed dipole/quadrupole is made through the data and the result is shown in Figure 4.9. These fitted lines correspond to:

$$B_{rfit}(r = R_h, \theta, z = 0) = A_1\cos(\theta - \varphi_1) + A_2\cos[2(\theta - \varphi_2)]$$

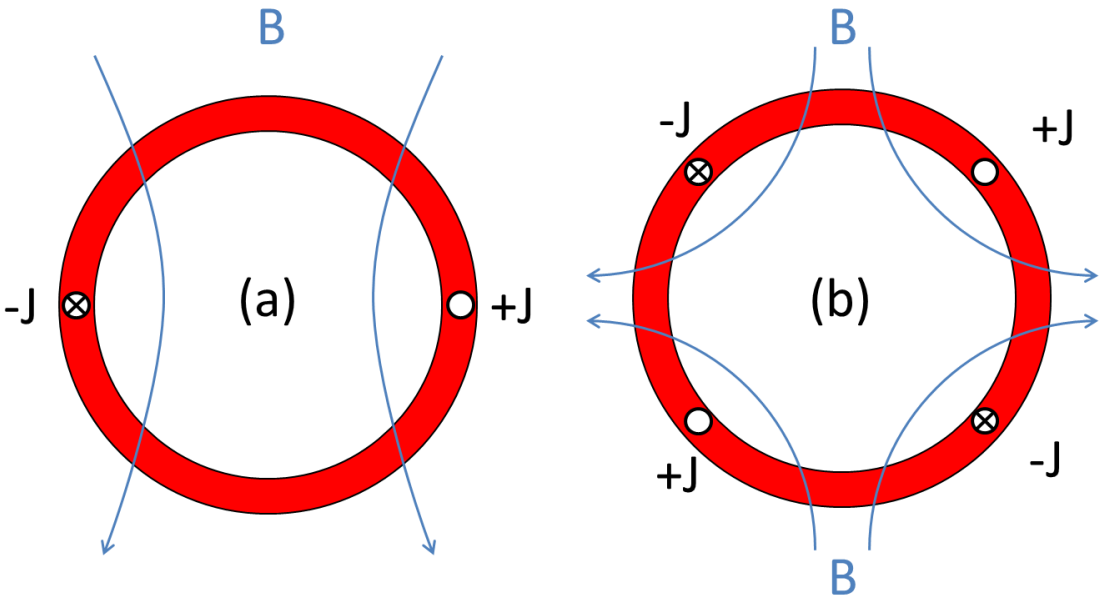

Figure 4.10 schematic illustration of dipole (a) and quadrupole (b) magnetic field and current distribution on a cylinder, bleu magnetic field lines, black current, red cylinder

To model this, the analytical expression of paragraph 2.1.1 is taken (equation (19)).

$$B_r(r, \theta, z = 0) = \frac{-1}{r}(E_0 \ln r + F_0) + \sum_{k=1}^{\infty}\left(E_k r^{k-1} + F_k r^{-(k+1)}\right)\sin[k(\theta - \varphi_k)] \qquad (19a)$$

$$B_\theta(r, \theta, z = 0) = (E_0\theta + G_0)\frac{1}{r} + \sum_{k=1}^{\infty}\left(E_k r^{k-1} - F_k r^{-(k+1)}\right)\cos[k(\theta - \varphi_k)] \qquad (19b)$$

Together with the fit to the results in Figure 4.9, the expressions allow to model the current distribution on the shield. Since it is known from paragraph 1.1.1 that a current distribution can be rewritten as a magnetization, this shows actually the effect of the magnetization due to remanence. This result is written out further in appendix B, which results in equation (29) for the current distribution over the shield.

$$\mu_0 J(\theta) = -2A_1\cos(\theta - \varphi_1) - 2A_2\frac{R_s}{R_h}\cos[2(\theta - \varphi_2)] \qquad (29)$$

R_s is the radius the of the shield and R_h is the measurement position and it is assumed that the shield is just one single thin walled cylinder. The constants from the fit of the B_y field in Figure 4.9b are taken and filled in$(A_1 = 0.14, A_2 = 0.139, \varphi_1 = 185.2, \varphi_2 = 174.3, R_s = 34mm, R_h = 5mm)$. This yields the current distribution over the wall as in Figure 4.11.

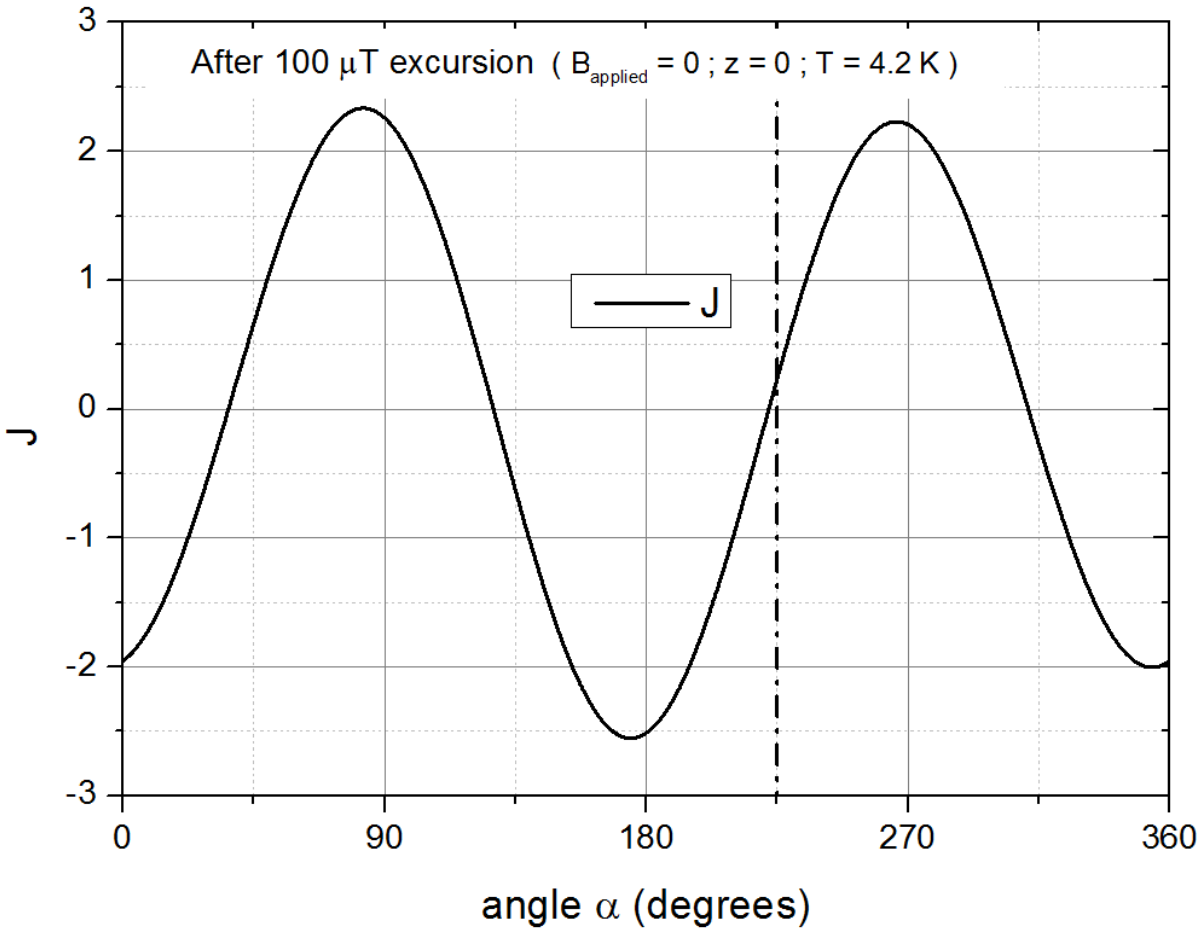

Figure 4.11 the model result for current distribution on the shield with constants $A_1 = 0.14, A_2 = 0.139, \varphi_1 = 95.2 + 90, \varphi_2 = 129.3 + 45, R_s = 34mm, R_h = 5mm$, the dash dot line is the position of the welds

As illustrated in Figure 4.10, this result can be seen as to rotating currents on the shield opposite each other which create a magnetic field caused by the magnetization. With the information that the welds are at position 225 degrees, it is indeed observed that at this angle there is an almost zero current, so that a high magnetic field created there. This model thus predicts that at the weld a high magnetization is created in the r-direction.

4.2 Nb shield

In this section, the measured data on the deep-drawn Nb shield (Figure 3.8) are presented. Paragraph 4.2.1 compares the observed axial and radial attenuation factors to the FEM model predictions as function of axial position, orientation and frequency.

4.2.1 Magnetic shielding Nb shield

First the attenuation along the central z-axis is studied with the field applied in the z-direction. Through this section, z=0 is defined as the bottom of the Nb shield. First the shield is cooled down with no external field present, to assure that no remanence is present as described in paragraph 1.2.2. A reference point is taken at z = 3mm with no field applied. As discussed in paragraph 3.1.2, this point is needed because the SQUIDs measure differentially. Now a field of 10μT is applied in the z-direction and the magnetic field profile is measured along the central z-axis. Normalizing with the applied field yields the attenuation factor. These results are compared to a Comsol model of the shield. For this model, the dimensions of the shield from Figure 3.8 are taken with a gap between the inner and outer part of 0.2mm.

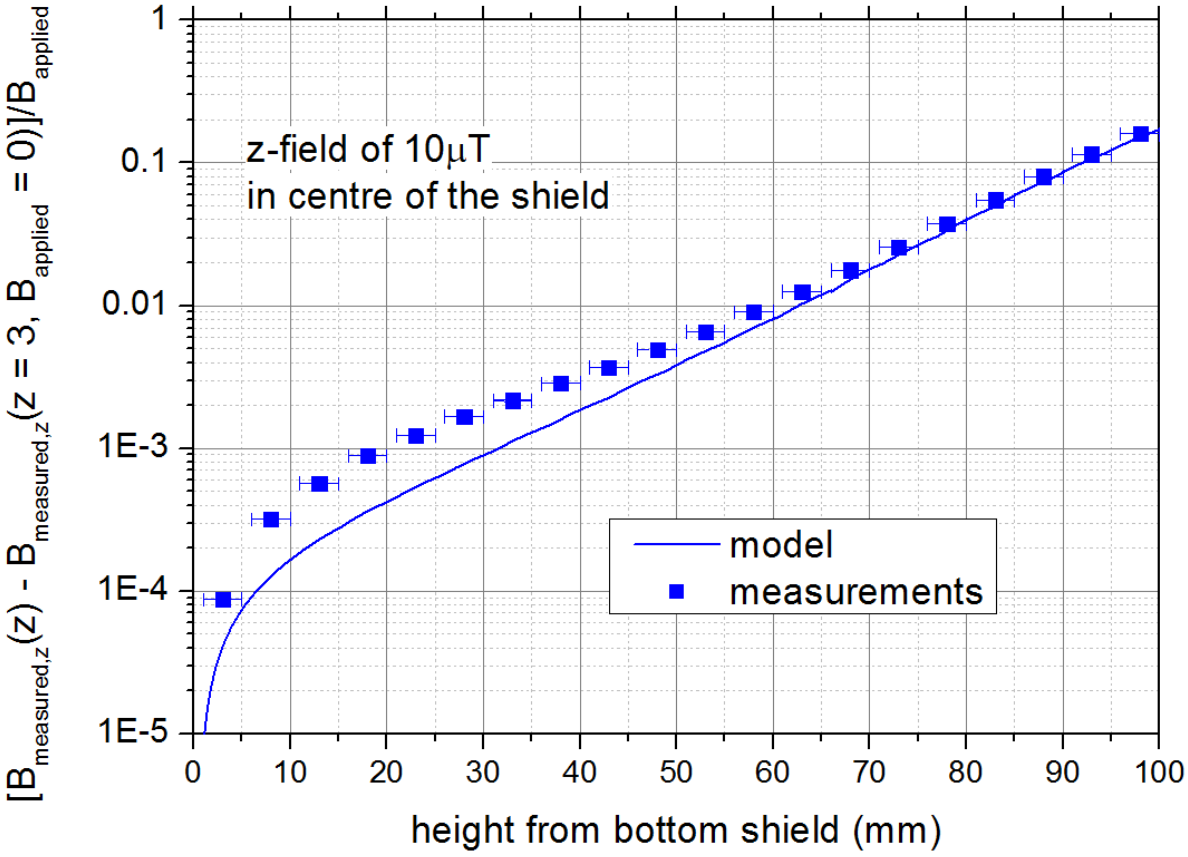

Figure 4.12 the axial attenuation factor along the central z-axis with applied axial field of 10μT along the z-direction, z=0 is bottom of the shield, blue squares are the measured results , blue line is a Comsol model with overlap of 9mm and gap of 0.2mm

The agreement between the model and the measurements is reasonable: both profiles have approximately the same shape, but below 60mm the measured values are a little higher than those of the model.

Next the attenuation along the central z-axis is measured again but now with the field applied in the x-direction. z=0 indicates the bottom of the Nb shield. First the shield is cooled down in zero external field to avoid remanence. Then a reference point is taken at z = 3mm and a field of 10μT is applied in the x-direction. The x-component of the magnetic field is measured along the central z-axis and normalized with the applied field to get the attenuation factor. These result are then again compared to the same model as before. The results are shown in Figure 4.13.

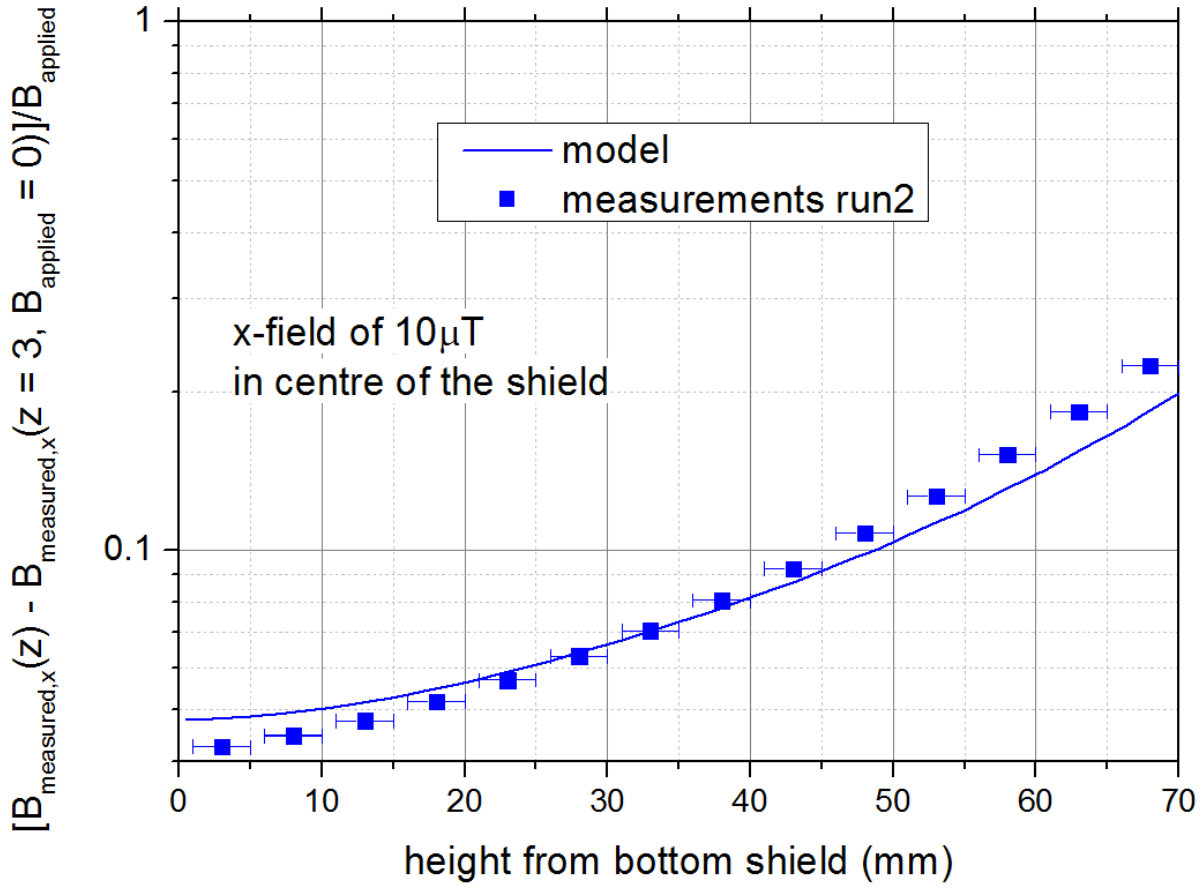

Figure 4.13 the radial attenuation factor along the central z-axis, with applied radial field of 10μT along the x-direction, z=0 is bottom of the shield, blue squares are the measured results , blue line is a Comsol model with overlap of 9mm and gap of 0.2mm

Once more the model and the measured results have the same, but the measured values seem to increase somewhat faster with height inside the shield than the model.

Next the magnetic field is studied in the presence of a radial applied field as a function of orientation, with the SQUID sensor 20mm off-axis as described in paragraph 3.1.3. As indicated in Figure 3.9, the external field is applied in the x-direction "x"- and "y" refer to the lab frame of reference while "u" and "v" define at rotating frame of reference attached to the SQUIDs. First the shield is cooled through its critical temperature with no field applied, so no remanence is present. Then the SQUID sensor is placed at 40mm below the top of the shield (z=66mm). A reference point is taken at $\alpha=0$ with no field present. Then an external magnetic field of 10μT is applied in the x-direction and the position/orientation of the SQUID sensor is changed by rotating around the central axis, as illustrated in Figure 3.9. After a full 360^0 scan, the process is repeated with the SQUID sensor 80mm below the top of the shield (z=66mm). The results are compared to the Comsol model predictions in Figure 4.14.

a)

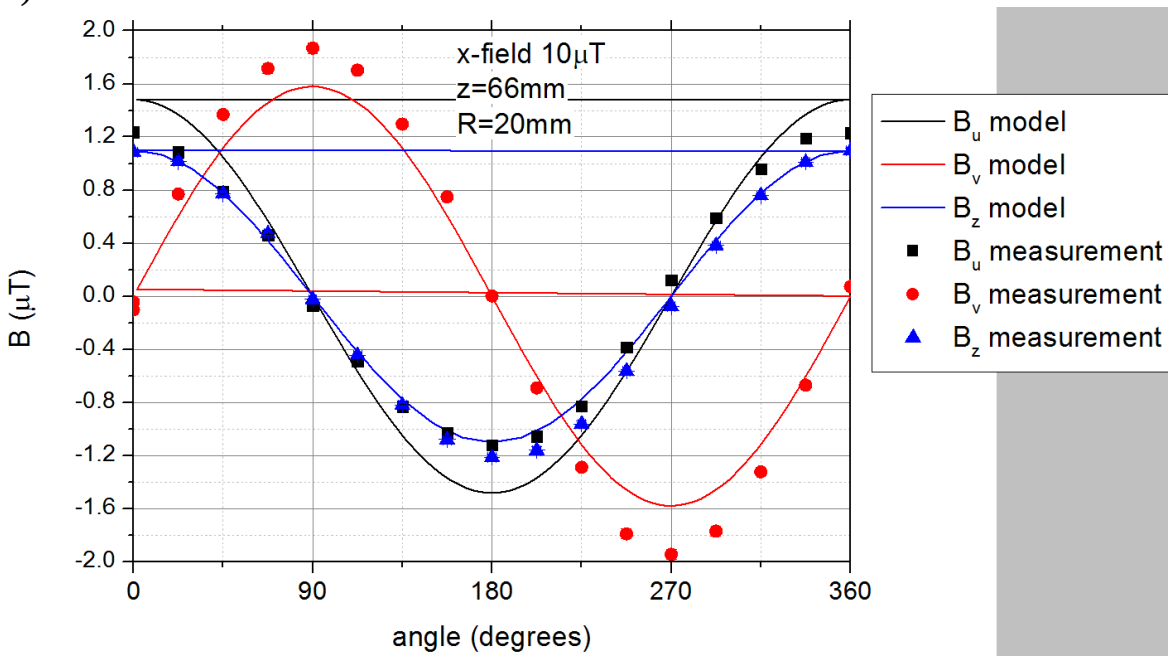

b)

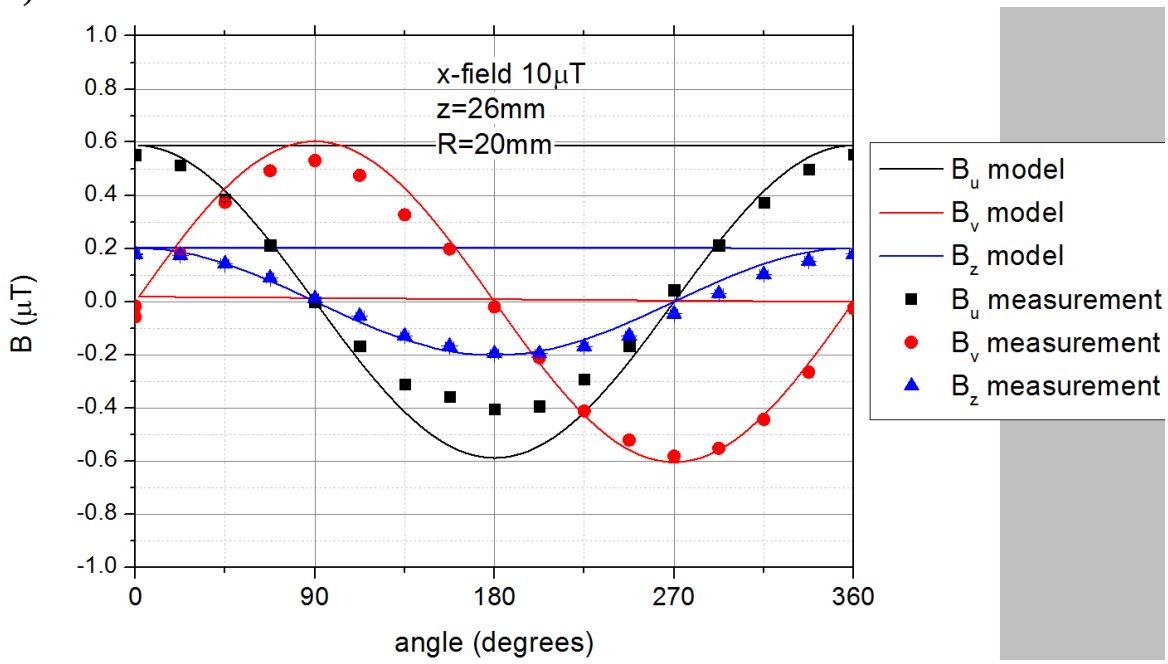

Figure 4.14 magnetic field measured at different orientations with an applied radial field of 10μT in the x-direction while SQUID sensor is 20mm off-axis, α=0 corresponds to the situations where the "u"- and "v"-direction in the reference frame of the SQUID coincide with the "x"- and "y" direction in the reference frame of the lab. The points are the measurement, the line is a Comsol model with overlap of 9mm and gap of 0.2mm, a) z=66mm, b) z=26mm

When the measured data is compared to the model, they have the same "dipole" shape (single wave) with a maximum deviation between both of ~20% for z=66mm and ~35% for z=26mm. These deviations, which thus seem to become relatively more important deep inside the shield, might be due to residual remanence or to imperfect modelling of the "gap" region where the 2 parts of the shield overlap.

It was feared that flux jumps, as described in paragraph 3.1.2, would not be obviously visible in these results, so the experiment was repeated with a lower radial applied field of 1μT. With this lower magnetic field, the flux jumps are relatively more important and thus easier to detect. The results are shown in Figure 4.15.

a)

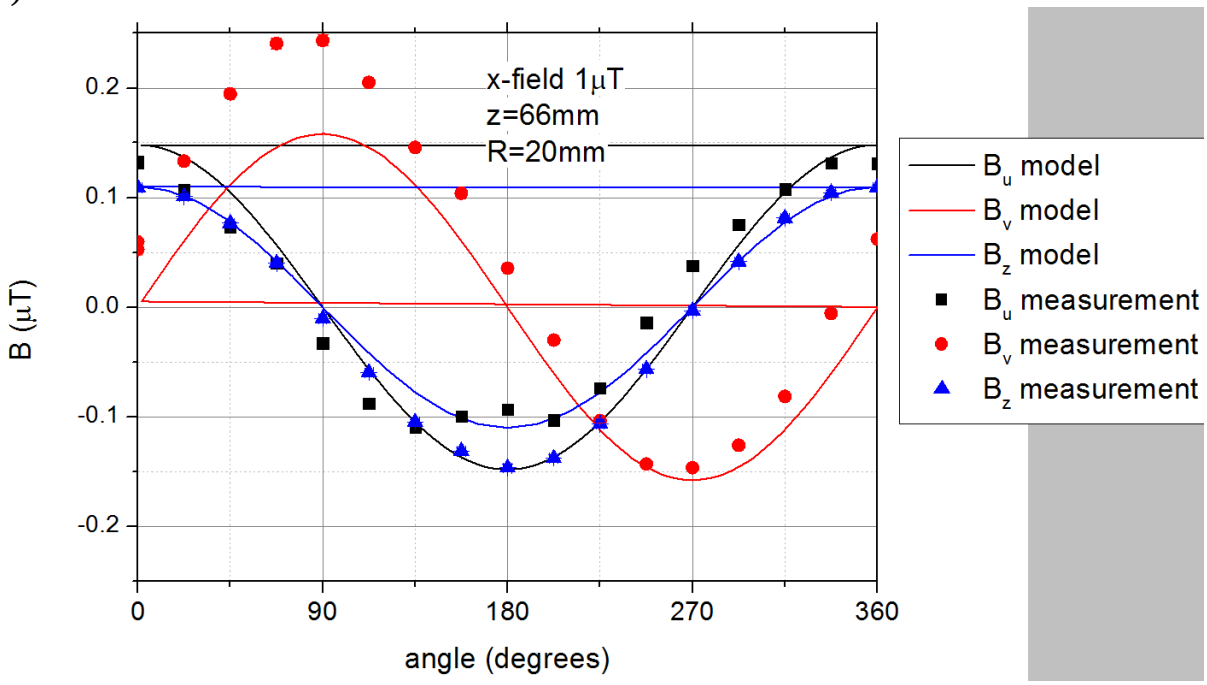

b)

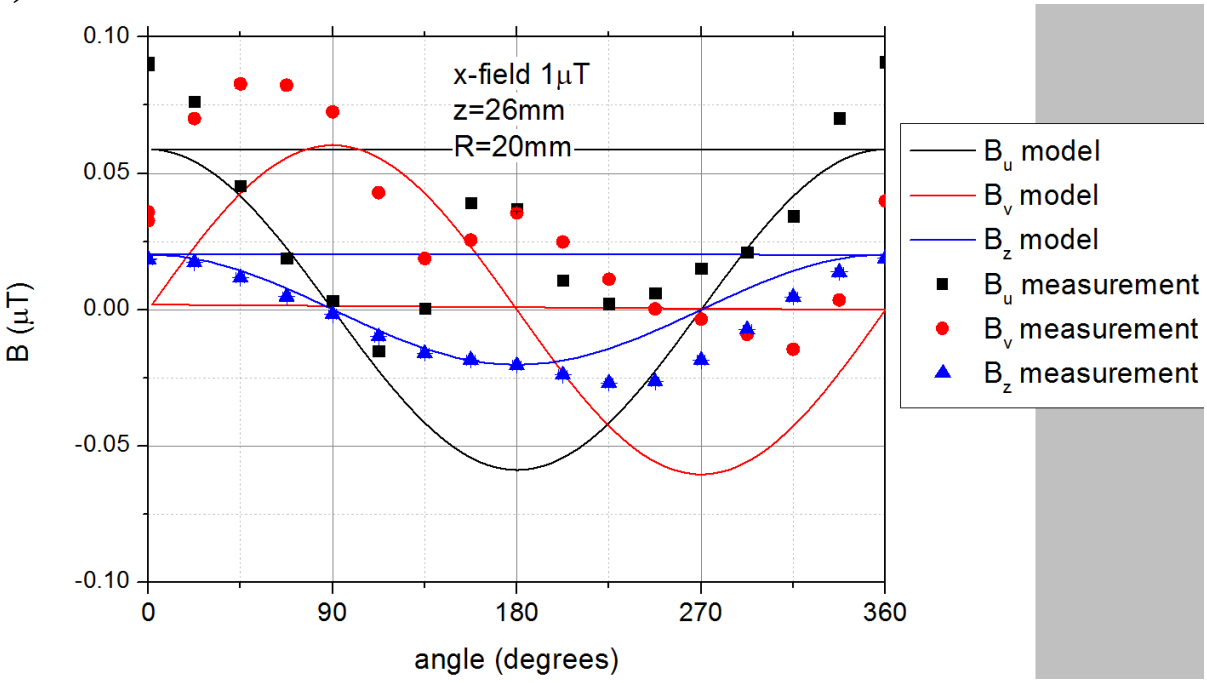

Figure 4.15 magnetic field measured with a field of 1μT applied in x-direction while SQUID sensor is 20mm of axis, α=0 the SQUID sensor "u" is 20mm off- axis in the x-direction. The points are the measurement, the line is a Comsol model with overlap of 9mm and gap of 0.2mm, a) z=66mm, b) z=26mm

At z=66mm the measured results and the model profile have again the same general shape but the maximum deviation between both has now become ~40%. Deeper in the shield at z=26mm (Figure 4.15b), even the qualitative correspondence has now been lost.

If the deviations between model and data come from imperfect modelling, we would expect them to scale with the applied external field. The fact that their relative importance clearly increases with decreasing external field, suggests that they are due to a remanence effect, as described in paragraph 1.2.2. Even if the cool-down was made in an external field that was nominally zero, it is assumed to be "frozen in" vortices which cause local problems.

Next the frequency dependence of the axial shielding factor is studied. Data are collected at z=26mm (80mm below the top of the shield) with the SQUID cube still positioned 20mm off-axis at an angle of α=0 (i.e. the position as drawn in Figure 3.9). First the shield is cooled through its critical temperature in zero external field so that remanence is minimised. Then an AC field is applied in the z-direction as a sine wave with an amplitude of approximately 1μT and a frequency of 0.1Hz. The magnetic field inside the shield is measured and compared to the applied field to determine the attenuation factor. Also the phase difference between applied and measured field is recorded. Then the frequency is increased in steps and the measurement is repeated until a frequency of 3kHz is reached.

The applied magnetic field amplitude is then increased to approximately 10μT and the measurements repeated up to a frequency of 300Hz. The second measurements didn't reach 3kHz due to the voltage compliance limit of the power supply.

The results of these experiments are shown in Figure 4.16.

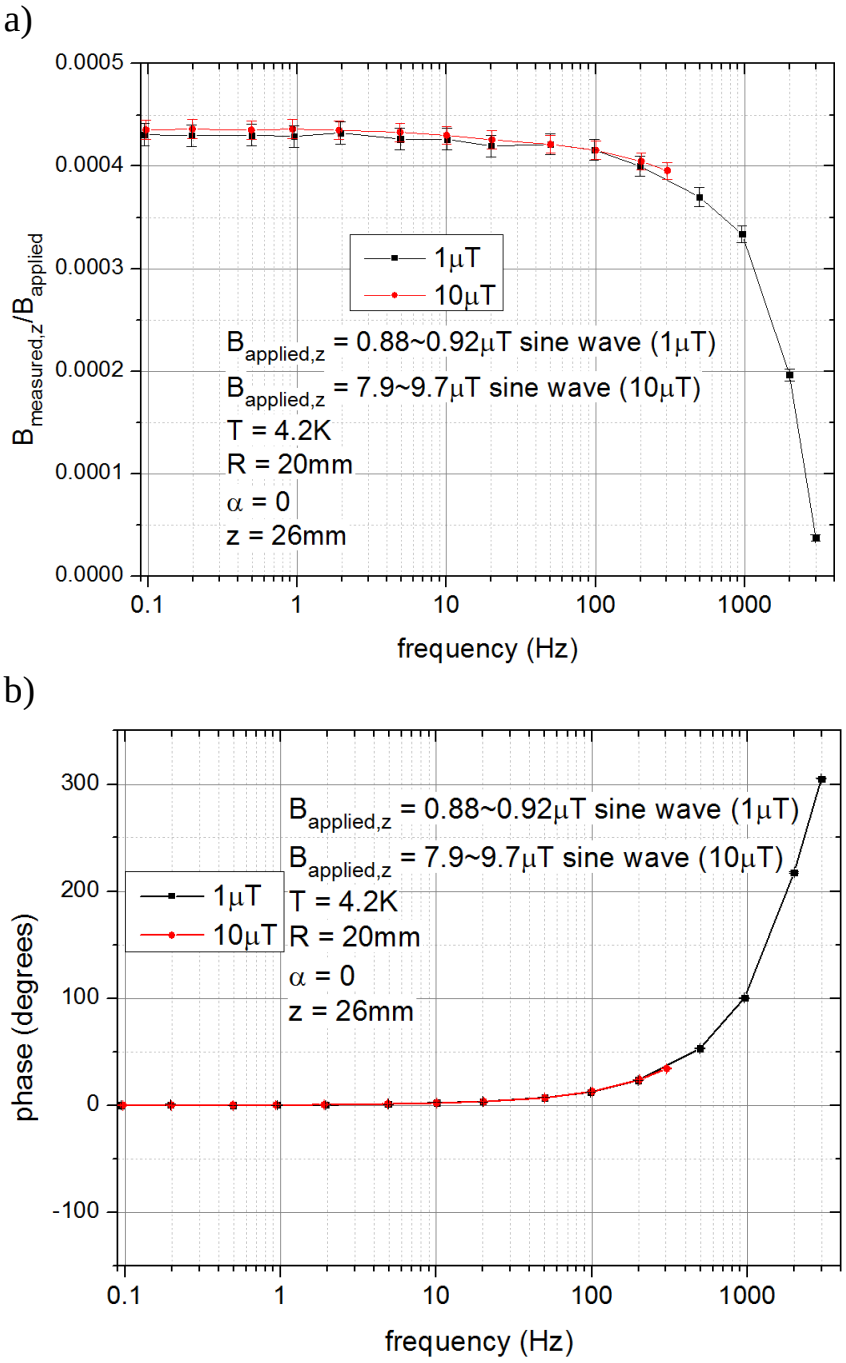

Figure 4.16 frequency dependence of the measured axial field deep inside the Nb shield, measured with 2 different amplitudes of the axially applied sinusoidal field, a) attenuation versus frequency, b) phase versus frequency

From Figure 4.16a it can be seen that with increasing frequency the attenuation becomes lower and that no change is visible when a higher field is applied.

Figure 4.16b shown that at ~10Hz the "eddy currents" seem to begin to play a role causing a phase shift. Again no clear difference is observed by increasing the amplitude. Note that these "eddy" currents on first sight seem unexpected in a superconducting material (Meissner shielding should be frequency independent) but may be explained in terms of the "two-fluid" model. At T≠0, not all charge carriers are paired into Cooper pairs and the remaining 'normal' electrons also exhibit an AC response [7].

4.2.2 Remanence Nb shield

These experiments were done to confirm the effect of remanence on the superconducting shield, as described in paragraph 1.2.2. With the shield above its critical temperature (so not yet superconducting) an axial magnetic field is applied of varying strength. While the field is still applied, the shield is cooled below its critical temperature so it becomes superconducting. Then the external field is turned off and the magnetic field is measured along the central z-axis. The reference point is taken at z=3mm so that a good comparison can be made between the remanence effect of different fields, since the higher fields cannot be measured up to the same height as the lower fields due to the maximum range of the SQUID discussed earlier (paragraph 3.1.2). The results are shown in Figure 4.17.

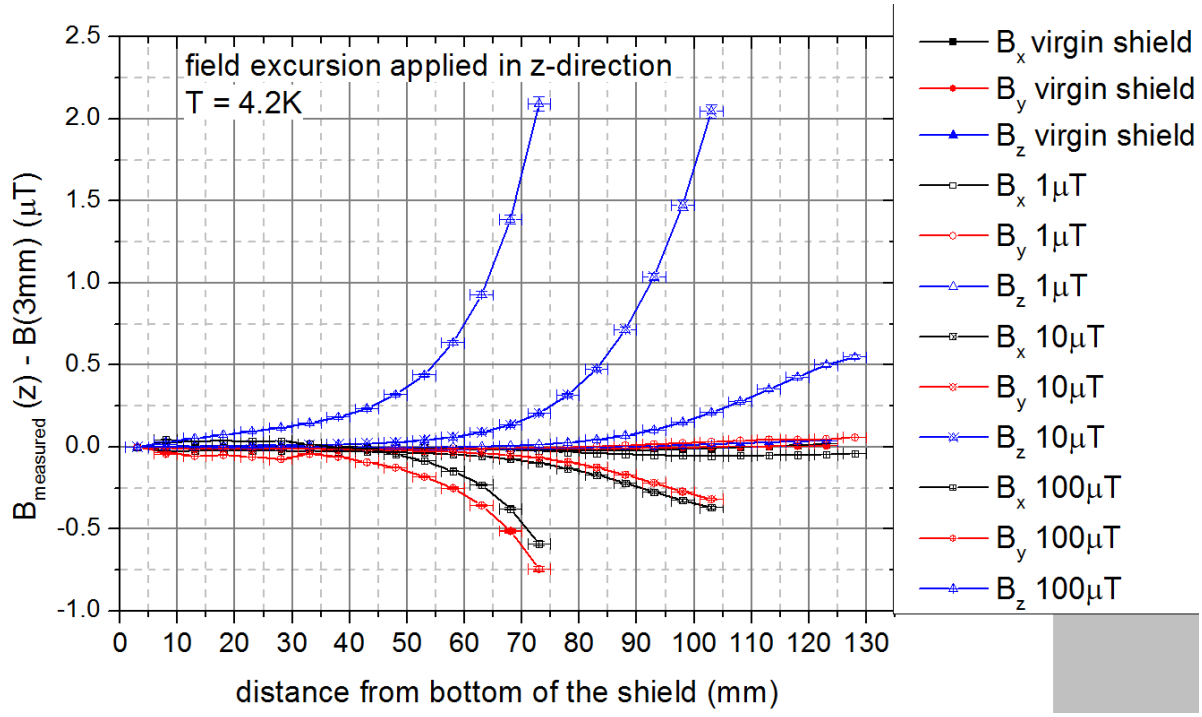

Figure 4.17 the effect of remanence on a superconducting shield measured after different axial magnetic excursions applied while going thought the critical temperature

It should be mentioned that the 100μT data were less stable than the other ones. This is assumed to be an effect of applying a large field to the SQUID sensor. With geometric flux trapping as described in paragraph 1.2.2, it is expected that with each step of increasing the applied magnetic field with a factor 10 while cooling down, the measured remanent magnetic field will also increase by 10. This is indeed observed in the data of Figure 4.17.

It is therefore concluded that geometric flux trapping clearly plays a role also with this type of half-open shield geometries.

4.3 1-D Ginzburg-Landau calculations

This section presents the results of the 1-dimensional GL simulation of the field-cooling through the superconducting transition in the presence of T_c variations. The goal of these calculations is to verify the hand-waving requirement on the magnitude of the temperature gradient:

$$\xi(x_d) = x_d \rightarrow \frac{0.74\xi_0}{\sqrt{\frac{\Delta T_c}{T_c}}} > \frac{\Delta T_c}{|\nabla T|} \rightarrow |\nabla T| > \left(\frac{\Delta T_c}{T_c}\right)^{3/2} \frac{1}{0.74}\frac{T_c}{\xi_0} \tag{13}$$

which was discussed in paragraph 1.2.4. If the temperature gradient is too small, the defect will become "enclosed" by a fully developed order parameter before it becomes superconducting and this normal 'island' will trap flux.

The GL equations described this problem have been derived in paragraph 2.2.3:

$$\frac{d^2 f}{du^2} - {\alpha_0}^2 f + f - f^3 + \tau\left[\frac{1}{1 - t_0 + \tau u}\frac{df}{du} - f\frac{1}{4}\frac{\tau}{(1 - t_0 + \tau u)^2} + uf - uf^3\right] - t_0[f - f^3] = 0 \tag{26a}$$

$$-\kappa^2 \frac{d^2\alpha_0}{du^2} + \alpha_0 f^2 + \tau u \alpha_0 f^2 - t_0 \alpha_0 f^2 = 0 \tag{26b}$$

These are the coupled non-linear differential equations for the amplitude of the order parameter f (normalised to its zero-temperature equilibrium value ψ_∞) and the magnetic vector potential α_0 (normalised to $\phi_0/2\pi\xi_0$). The reader is also reminded that $u \equiv x/\xi_0$ is the normalized position, $t_0 \equiv T/T_c$ the normalized temperature and $\tau \equiv \frac{\nabla T \xi_0}{T_c}$ the normalized temperature gradient (see appendix C-E). The boundary conditions describing the problem are:

$$\frac{\mathrm{d}\alpha}{\mathrm{d}u}_{u=0} = -\beta_0, \qquad \frac{\mathrm{d}\alpha}{\mathrm{d}u}_{u=\infty} = 0$$

$$\frac{df}{du}_{u=0} = b, \qquad f(\infty) = 1$$

To find the solution to the GL equations, the numerical iteration technique described in paragraph 2.2.3 is used:

$$f_i^{p+1\prime} = b + \sum_{j=0}^{i}\left[\left(\alpha_j^p\right)^2 f_j^p - f_j^p + \left(f_j^p\right)^3 - \tau\left[\frac{1}{1 - t_0 + \tau u_j}\frac{df_j^p}{du_j} - f_j^p\frac{1}{4}\frac{\tau}{\left(1 - t_0 + \tau u_j\right)^2} + u_j f_j^p - u_j\left(f_j^p\right)^3\right] + t_0\left\{f_j^p - \left(f_j^p\right)^3\right\}\right]\Delta u \tag{27a}$$

$$f_i^{p+1} = 1 - \sum_{j=i}^{N} f_j^{p+1\prime}\Delta u \tag{27b}$$

$$\alpha_i^{p+1\prime} = \beta_0 + \frac{1}{\kappa^2}\sum_{j=0}^{i}\left[\alpha_j^p\left(f_j^p\right)^2 + \tau u_j \alpha_j^p\left(f_j^p\right)^2 - t_0\alpha_j^p\left(f_j^p\right)^2\right]\Delta u \tag{28a}$$

$$\alpha_i^{p+1} = -\sum_{j=i}^{N}\alpha_j^{p+1\prime}\Delta u \tag{28b}$$

With the damping conditions:

$$f = cf_{new} + (1-c)f_{old}, \qquad \alpha = c\alpha_{new} + (1-c)\alpha_{old}$$

The parameters taken for this model are: the magnetic field $\mu_0 H$ is 100μT, the coherence length ξ_0 is 20nm, the GL parameter $\kappa=\lambda/\xi_0$ is 10, the critical temperature T_c is 8K, the beginning temperature T_0 is 7.98K and the gradient of real part of the wave function b (b=df/du) is 0.005.

For the first model, the temperature gradient is taken to be zero and no defects are present in the critical temperature profile. The initial starting guess needed for the iteration method is taken to resemble Figure 2.6. The iteration recipe (equations 27a,b and 28a,b) is then repeated until the maximum local difference between the old and the new function value is shorter than 0.001. The result is shown in Figure 4.18.

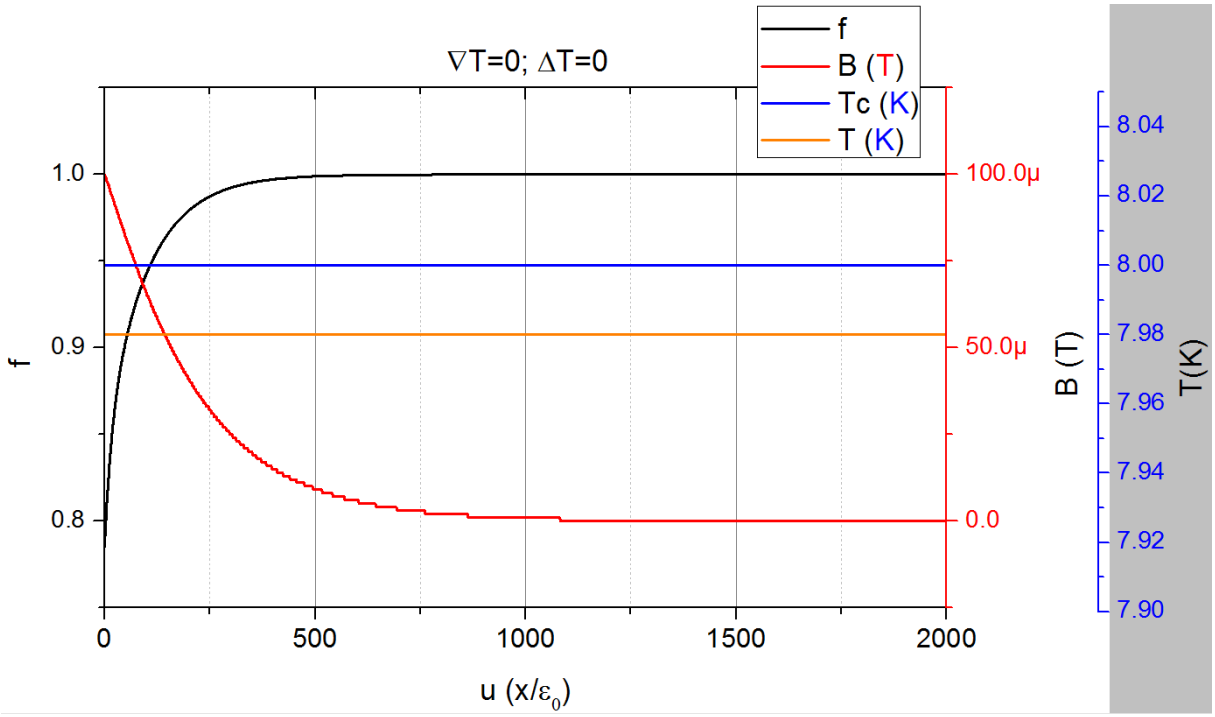

Figure 4.18 result of the GL model with no temperature gradient or defect in profile of T_c, T_c=8K, B=100μT, T_0=7.98K, κ=10,ξ_0=20nm

Note that this situation does not yet describe the "cool-down" N/S interface that we seek to simulate. Instead, f is forced to zero at x<0 so that this situation corresponds to the "text-book" example of the behaviour of the field and order parameter at the surface of a superconducting sample. However, since we expect f and B to behave qualitatively similar at the interface $T=T_c$ in the presence of a thermal gradient, we can use this solution as a starting guess for a cool-down scenario. So next the model is repeated, only now with a temperature gradient present. The same parameters and technique as before are implemented this time with $|\nabla T|$=6000K/m. This results in the function f(u) and B(u) profile shown in Figure 4.19. Note that T_c is still assumed to be homogeneous.

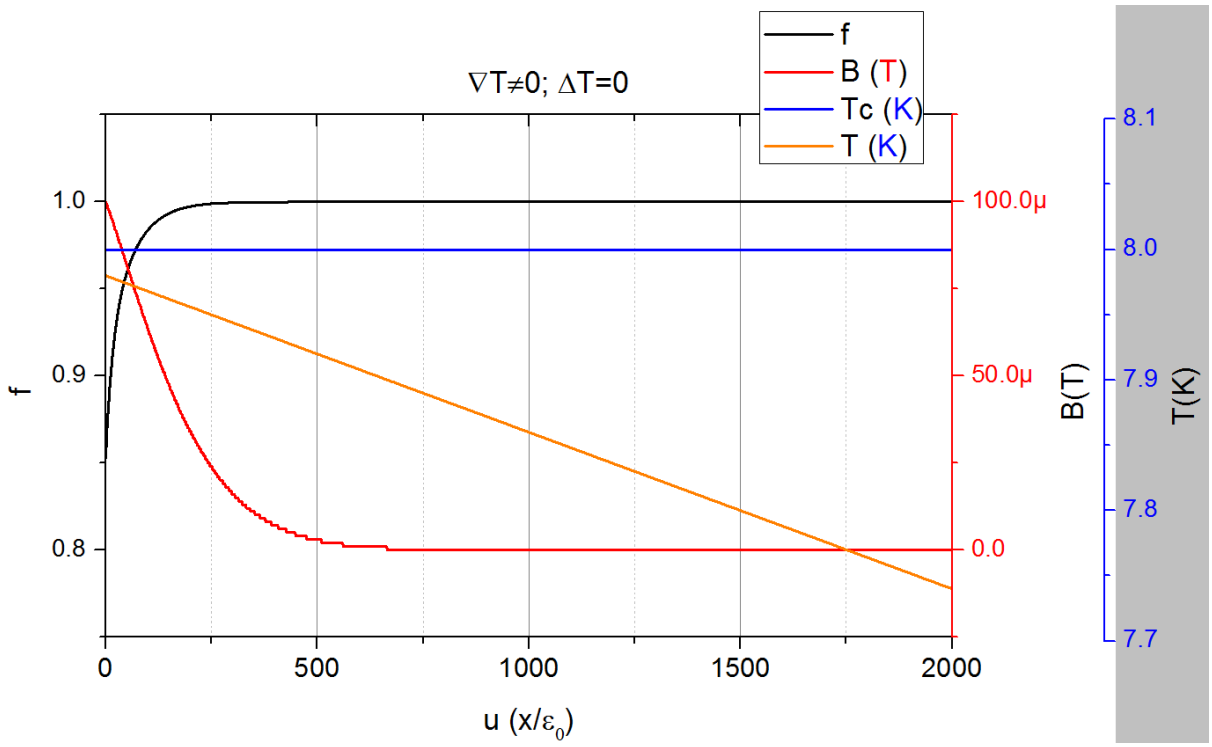

Figure 4.19 result of the GL model with temperature gradient and no defect in profile of T_c, T_c=8K, B=100µT, T_0=7.98K, ∇T=6000K/m, κ=10,ξ_0=20nm

If the two models (Figure 4.18, $\nabla T = 0$ and Figure 4.19, $\nabla T \neq 0$) are compared, it can be seen that the temperature gradient causes the "effective" coherence length and penetration depth to become shorter. This is to be expected, since both ξ and λ are temperature dependent and become shorter at lower temperatures.

The result with the temperature gradient (Figure 4.19) shows that the new technique as described in paragraph 1.2.4 would work for a material with an uniform critical temperature.

Since it is not expected that such an ideal material exists a defect is placed in the critical temperature profile. To model this, first the model as in Figure 4.19 is made. When this has converged, the defect is brought in from the left in small steps. This is done in the model by either changing the beginning temperature, the critical temperature locally or both. For each step a new model is present which needs to be allowed to converge the initial starting guesses are each time the result of the previous step. How the interface is modelled through the defect is illustrated in Figure 4.20.

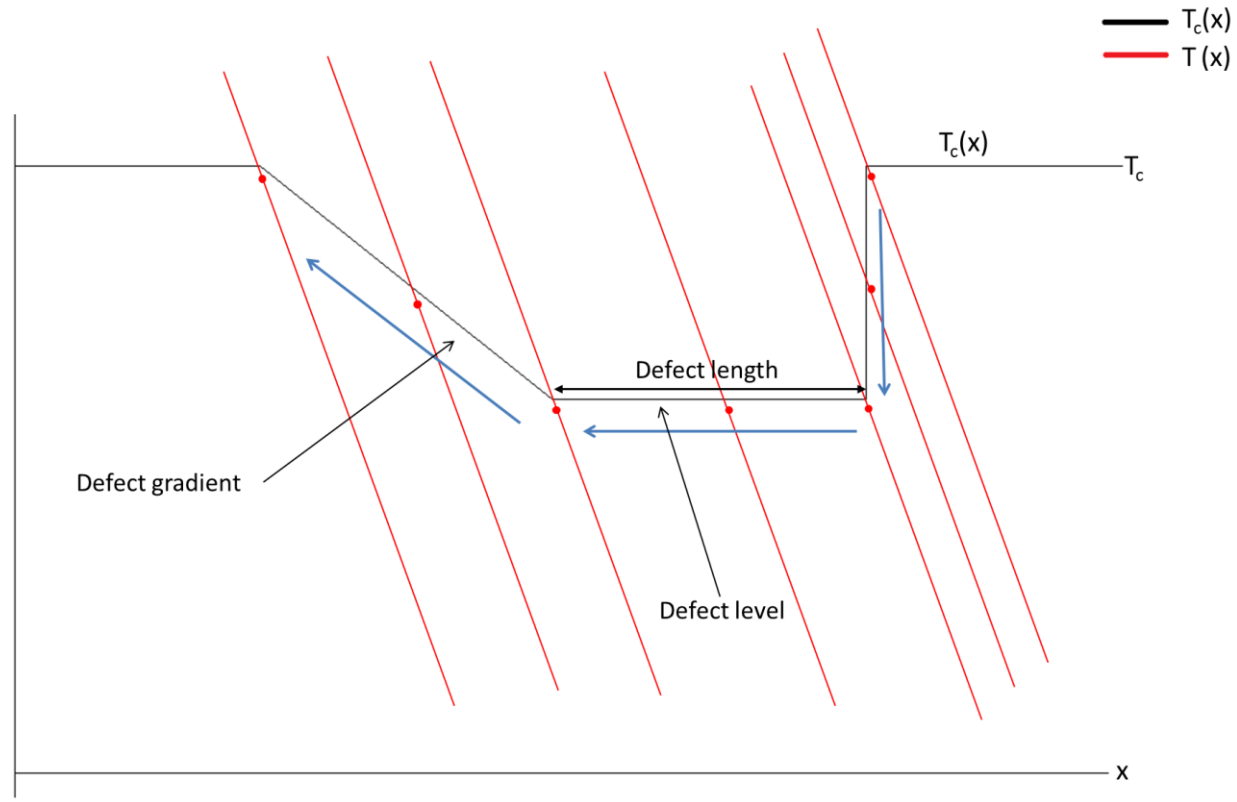

Figure 4.20 critical temperature profile with a defect in it, the black line represents the $T_c(x)$ profile, red lines represent successive T(x) profiles, the red dots indicate the position of T_0, the arrows indicate the way the temperature profile is moving

This is now modelled with the following parameters of: $\mu_0 H=100\mu T$, $\xi_0=20nm$, $\kappa=10$, $T_c=8K$, $T_0=7.995K$, the gradient of the magnitude of the wave function b (b=df/du) is 0, $\nabla T=6000K/m$, defect length is approximately 2μm (see Figure 4.20), defect T_c level is 7.98K ($\Delta T_c=0.02$), defect gradient (see Figure 4.20) is 5000K/m. Some of the calculation results are given in Figure 4.21.

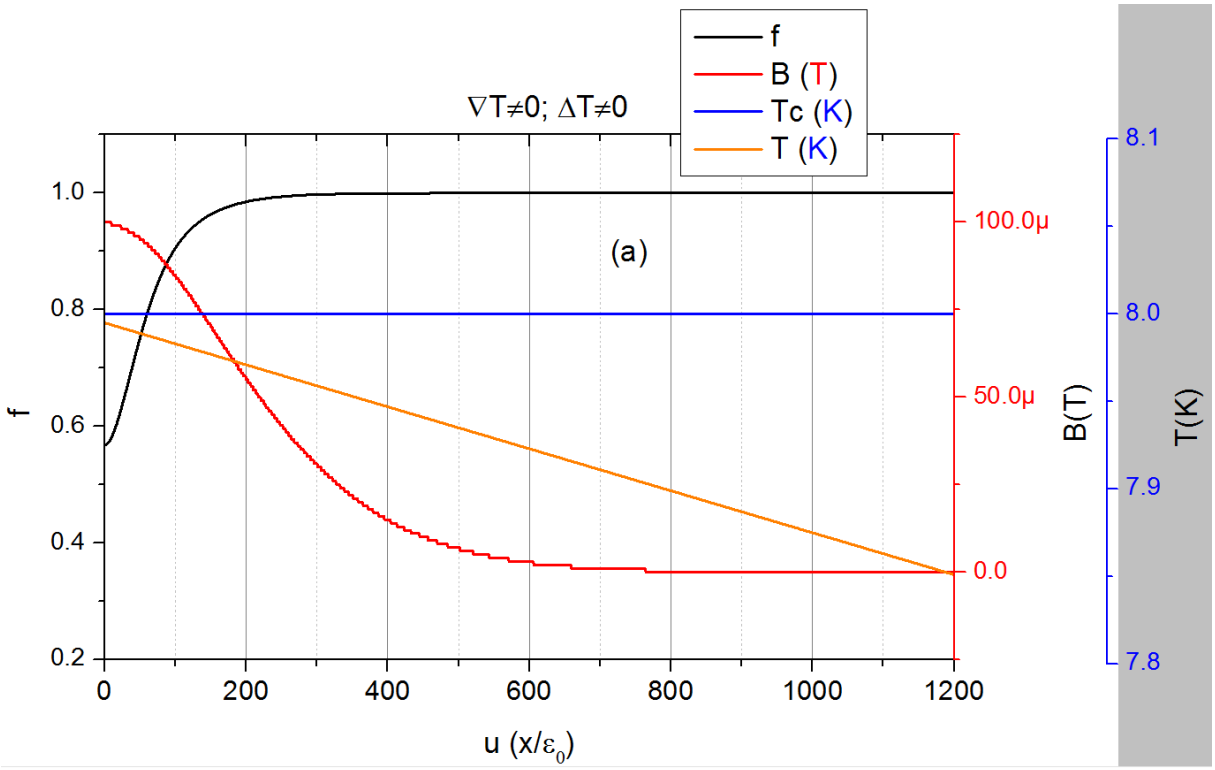

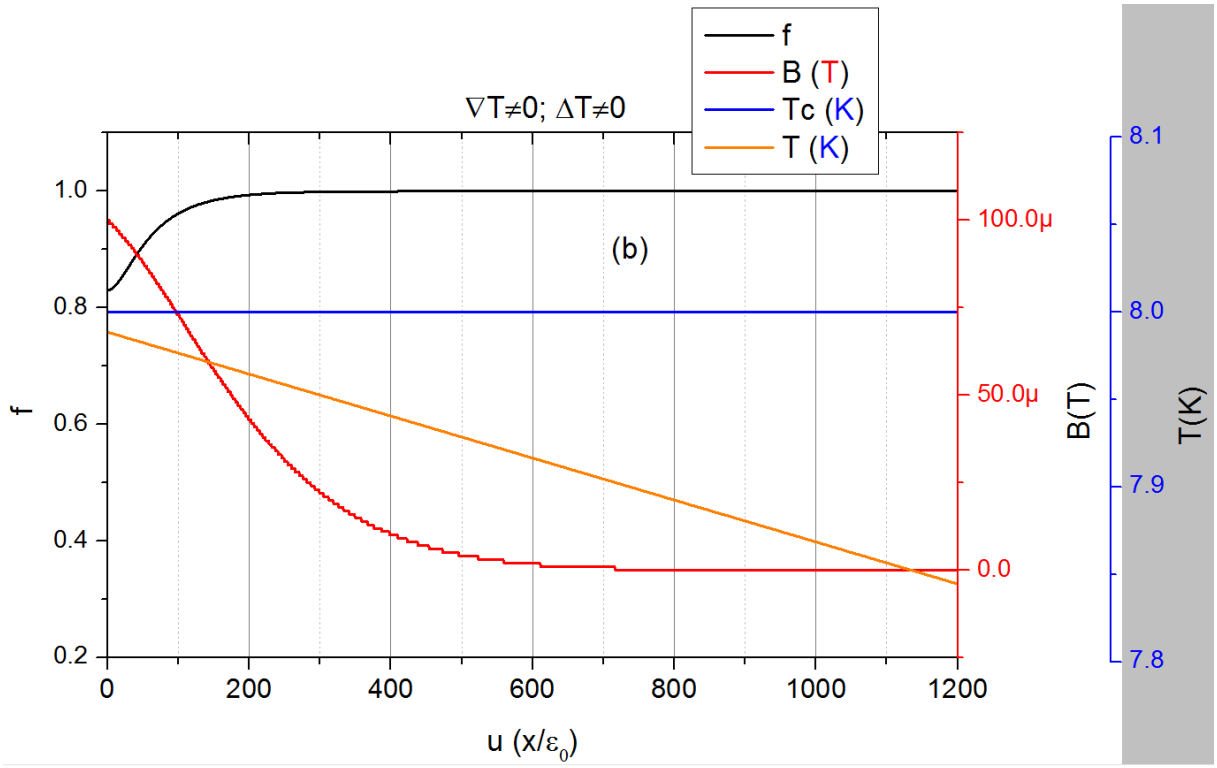
f
B (T)
Tc (K)
T (K)
∇T≠0; ΔT≠0
(b)
f
u (x/ε0)
B(T)
T(K)
100.0μ
50.0μ
0.0
8.1
8.0
7.9
7.8

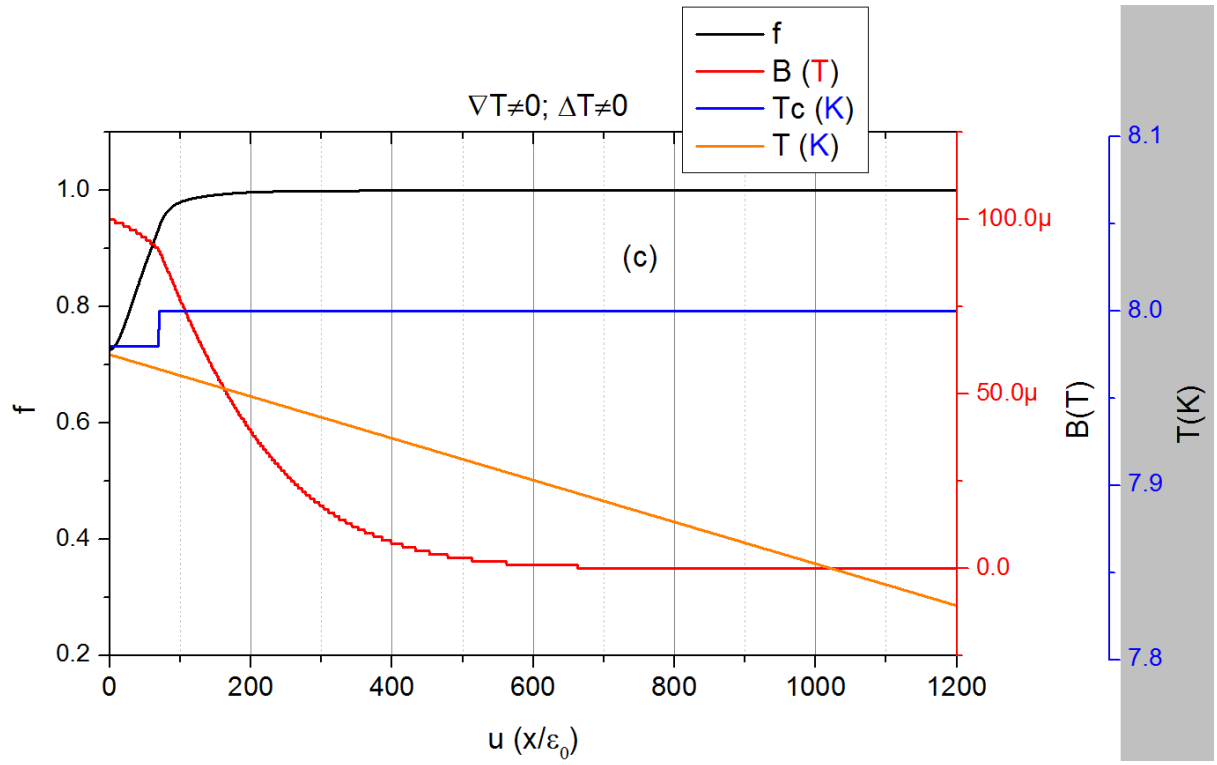
f
B (T)
Tc (K)
T (K)
∇T≠0; ΔT≠0
(c)
f
u (x/ε0)
B(T)
T(K)
100.0μ
50.0μ
0.0
8.1
8.0
7.9
7.8

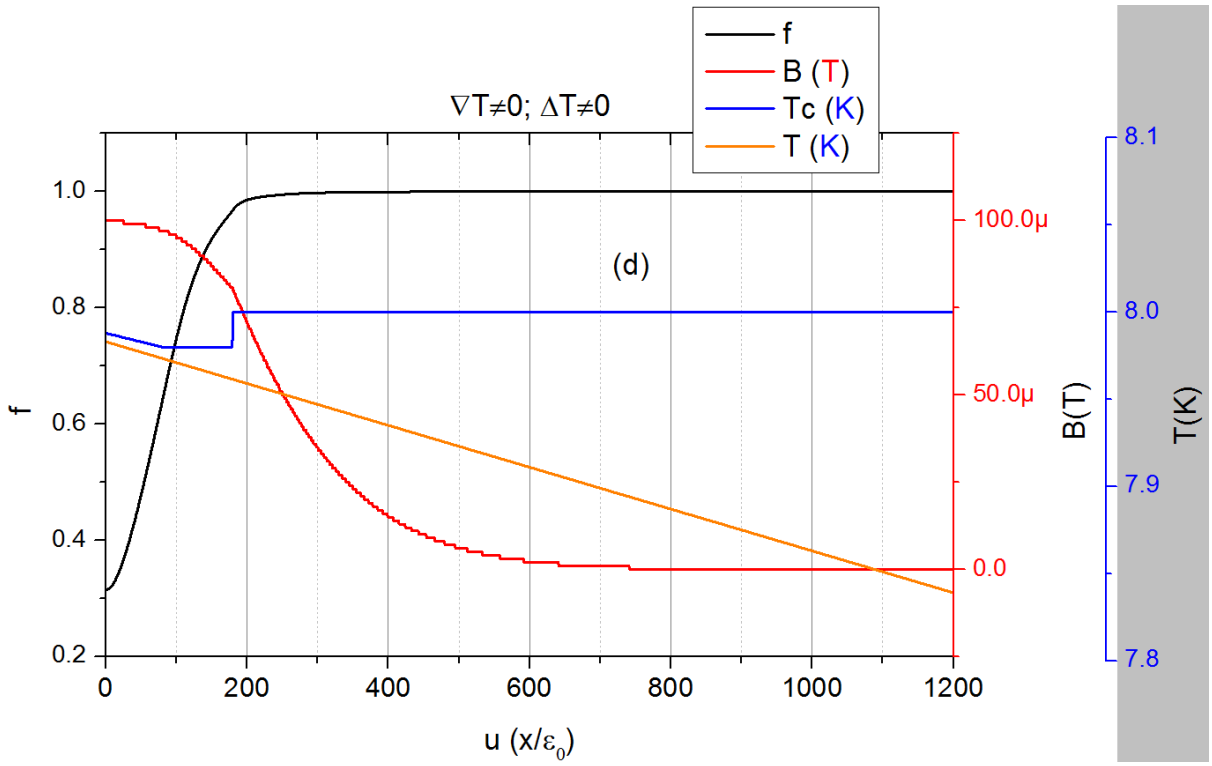
f
B (T)
Tc (K)
T (K)
∇T≠0; ΔT≠0
(d)
f
u (x/ε0)
B(T)
T(K)
100.0μ
50.0μ
0.0
8.1
8.0
7.9
7.8

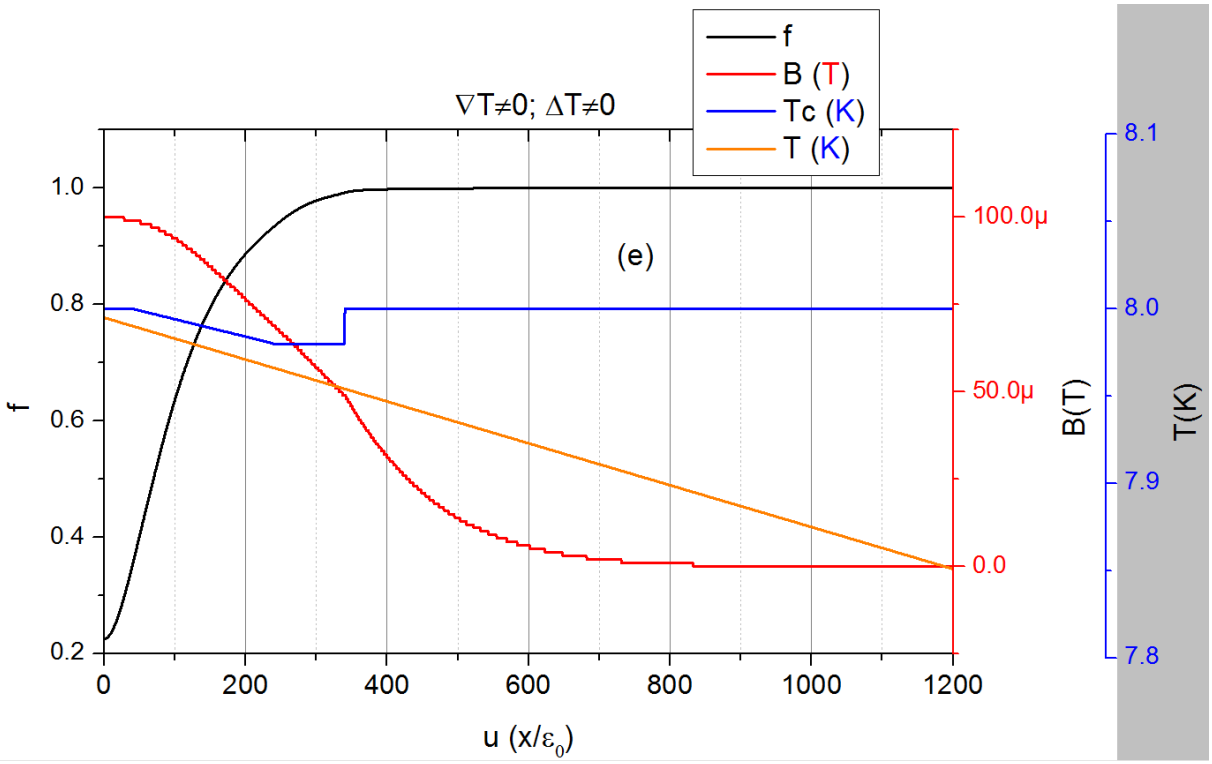
f
B (T)
Tc (K)
T (K)
∇T≠0; ΔT≠0
(e)
f
u (x/ε0)
B(T)
T(K)
100.0μ
50.0μ
0.0
8.1
8.0
7.9
7.8

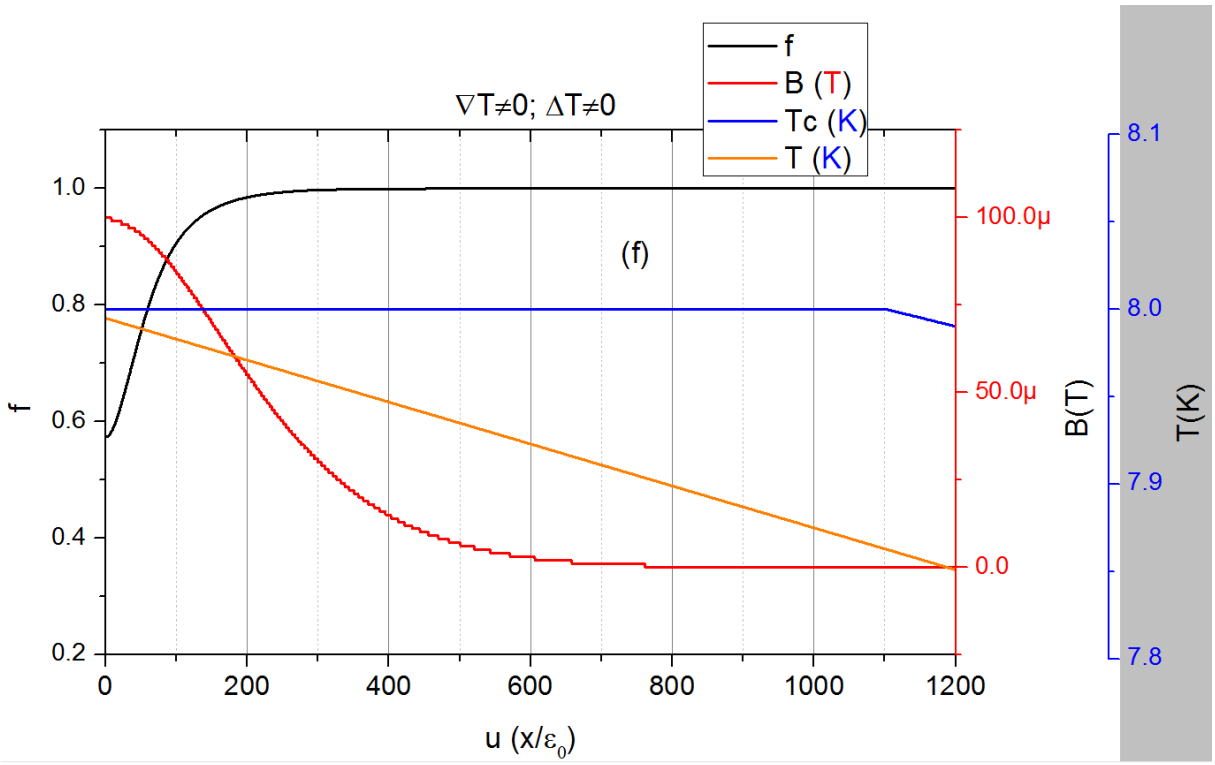

Figure 4.21 result of the GL model with a temperature gradient and a defect in the T_c profile, T_c=8K, B=100μT, T_0=7.98K, ∇T=6000K/m, defect length≈2000nm, defect level=7.98K, defect gradient=5000K/m, κ=10,ξ_0=20nm, a) starting position no defect present, b) halfway through the defect level, c) halfway through the defect length, d) halfway through the defect gradient, e) defect has passed through the interface but still is close to the interface, f) defect has passed through the interface and is deep into the superconductor

In this specific example the new cooling technique does work as can be seen in Figure 4.21(a) to f(f). The effect of the defect on the interface can be observed comparing Figure 4.21(a) with (e): it can be seen that the magnetic field now deeper inside the superconductor at the interface and that the order parameter also stabilizes later. Nevertheless, the f(u) and B(u) profiles qualitatively look the same as in Figure 4.20 (simulation with ΔT_c=0). More importantly, Figure 4.21(f) shows that B goes to zero deep inside the superconductor: no flus is "trapped" inside the defect during cool-down.

However, this is just one choice of starting parameters and, specifically, of the defect shape. If we want to validate the hand-waving argument from paragraph 1.2.4, we should also be able to simulate the opposite scenario (i.e. flux trapping inside the defect) and show that transition between both indeed occurs when $|\nabla T|\frac{\xi}{T_c} \approx \frac{\Delta T_c}{T_c}$.

The model with a defect in the critical temperature was therefore repeated with multiple other starting values and found to converge as long as the defect gradient was smaller than the temperature gradient. But in all cases where the defect gradient was larger than the temperature gradient, the model broke down. This is because the temperature profile then crosses the critical temperature profile as illustrated in Figure 4.22. At certain points, the temperature and the critical temperature are the same values. Due to the factors $\frac{1}{1-\frac{T(u)}{T_c(u)}}$ in equation (26a), an certain terms in the equation diverge in the points. The iteration procedure cannot handle this and crashes, making the model ineffective for this problem.

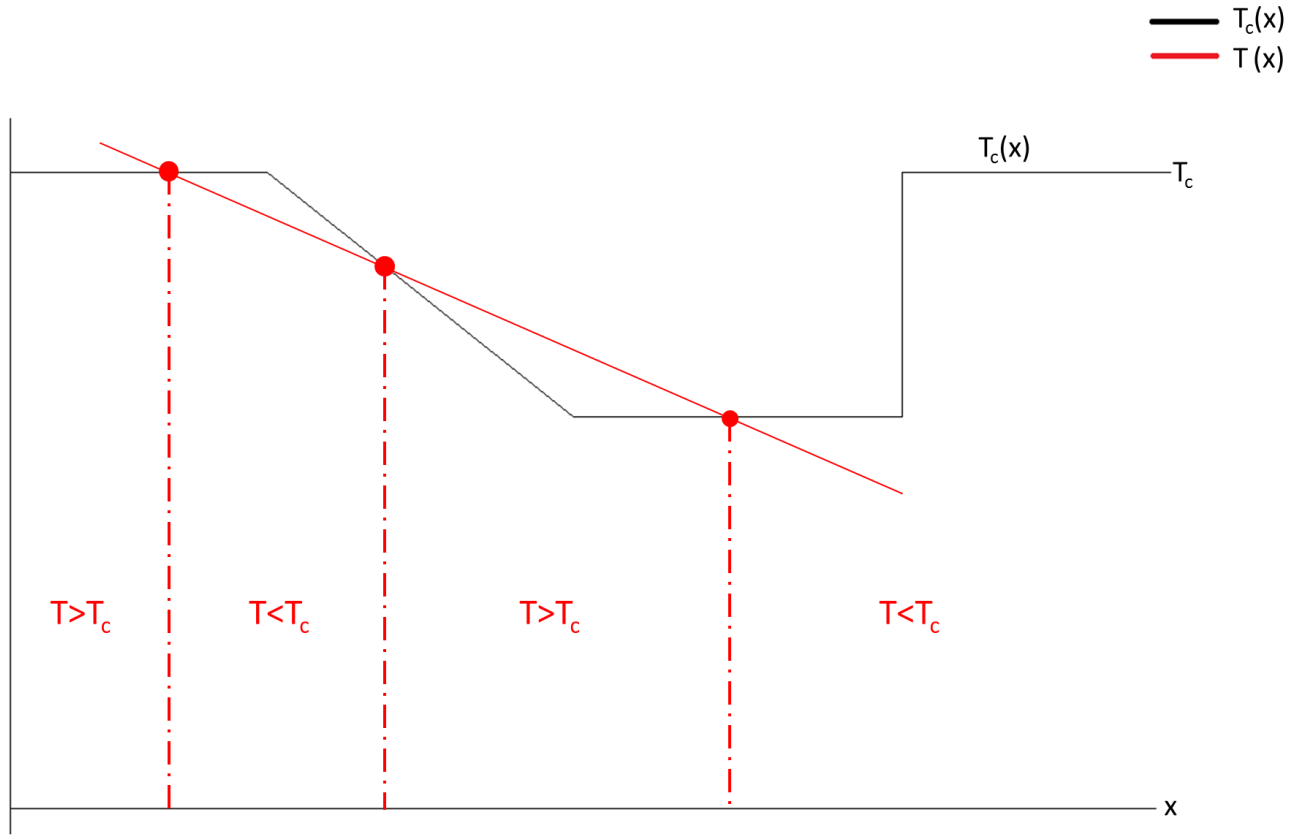

Figure 4.22 temperature gradient smaller then defect gradient, black line $T_c(x)$, red line T(x), red dots indicate the points where an infinite value would occur

Within the remaining time frame of the assignment, no solution was found for this divergence problem, so that these calculations at the writing of this report remain inconclusive regarding the hand-wavy formula.

5 Discussion and conclusions

From the experimental results obtained with the simple double-walled CryoPerm shield, it is concluded that shield remanence has a significant effect on the shielding factor and that the present FEM model needs some work. More detailed conclusions are:

1) the simple FEM assumption "$B_{\parallel} = 0$ outside the μ-metal interface" yields model predictions which are in reasonable agreement with the measured data down to field values of ~0.1μT;
2) with the demagnetization procedure followed in this assignment (gradual decrease of an AC 'demagnetizing' field to a final amplitude of ~0.4A/m), remanent fields are of the order of ~0.1μT. subsequent field excursions to a ~0.1mT level causes on observably increase in the remanent magnetisation;
3) the remanence of the μ-metal shield is readily modelled analytically as straight forward surface currents. The layout of these currents does seem to show some correlation with the presence of a weld in the shield;
4) eddy current shielding in this metal becomes significant at frequencies above ~1Hz.

This leads to the general recommendations that if the CryoPerm shield is used in the Athena mission, it should preferably be made without a weld and that problems may arise with remanence of the shield if a high magnetic field is applied. Ideally, the FEM model needs to be improved to incorporate a hysteretic M(H) relation if different shaped CryoPerm shields. Finally, as "magnetically soft" μ-metal as possible should be used, i.e. a metal with as low as possible coercivity.

From the data on the Nb shield it is concluded that remanence can also here be a problem and that the "magnetic insulation" FEM boundary conditions ($B_{\perp} = 0$) are not perfect:

1) the model and the measurement results for the attenuation as function of height and orientation match up reasonably well. Differences between both are assumed to be due to imperfect modelling of the gap between the two parts of the shield. This gap needs to be taken smaller but this turns out to be difficult to model with reasonable FEM grids;
2) with increasing frequency, the attenuation increases and a phase difference appears between the applied field and the attenuated one measured inside the superconducting shield. this observation is reminiscent of the normal eddy currents and seems to indicate that for frequencies above ~10Hz a two-fluid model might be necessary to predict AC shielding factors correctly;
3) both 'geometric' and 'microscopic' flux trapping during cool-down are observed. The former effect was clearly demonstrated, even when this shield has only one aperture (unless the gap between the top cylinder and bottom 'cover' plays a role, which was not checked further). The latter effect (vortex trapping) was observed as deviations of the order of ~0.1μT between the predicted orientation dependence and the data. It should be remarked however, that also here a role of the "gap" cannot be excluded.

This leads to the general conclusion that for the Athena mission the Nb shield needs to be in zero field when cooled down, since geometric flux trapping may cause big problems, but also vortex trapping might cause a local remanence in the range of ~100nT.

Finally, we comment on the GL model for the new in-field cool-down technique. From this model it is concluded that the controlled field-cool technique will indeed work as long as the gradient $\frac{dT_c}{dx}$ of the defect is smaller than the overall temperature gradient ∇T. However, a new model should be made to check what happens when the gradient of the defect is larger than the temperature gradient, since the present approach leads to divergence problems.

However, the present model does indicate that also the 'shape' of the defect is important. The hand-waving argument from the introduction says nothing of this shape of the defect, which appears to be an important parameter in the GL modelling here. So the earlier formula (equation (13)) is not complete and might need to be refined.

Apart from a more robust Ginzburg Landau calculation and a more refined hand-waving approach, it is also strongly recommended that the controlled in-field cooling technique should be tested experimentally to compare to the models made here.

Reference

[1] K.D. Irwin, G.C. Hilton, "*Transition-Edge Sensors*", in "Cryogenic Particle Detection", Springer Link, 2005

[2] D.J. Griffiths, "*Introduction to electrodynamics*", third edition, Pearson Benjamin Cummings, 2008

[3] J.M.D. Coey, "*Magnetism and magnetic materials*", Cambridge university Press, 2009

[4] A. Moldovanu, H. Chiriac, C. Ioan, E. Moldovanu, M. Lozovan, V. Apetrei, "*Functional study of a system of magnetic multilayer shields*", International Journal of Applied Electromagnetic and Mechanics **9** (4), pp. 421-425, 1998

[5] J.F. Hoburg, "*Principles of Quasistatic Magnetic Shielding with Cylindrical and Spherical Shields*", IEEE Transactions on Electromagnetic Compatibility **37** (4), pp. 574-579, 1995

[6] H.P. Quach, T.C.P. Chui, "*Low temperature magnetic properties of Metglas 2714A and its potential use as core material for EMI filters*", Cryogenics **44**, pp. 445-449, 2004

[7] C.P. Poole, "*Superconductivity*", Academic Press, 1995

[8] D.R. Tilley, J. Tilley, "*Superfluidity and superconductivity*", Van Nostrand Reinhold, 1974

[9] M.A. Taber, D.O. Murray, J.M. Lockhart, D.J. Frank, D. Donegan, "*Production of ultralow magnetic fields for gravity probe B (GP-B)*", Advances in Cryo. Eng. **39**, pp. 161-170 (1993)

[10] Q. Geng, H. Minami, K. Chihara, J. Yuyama, E. Goto, "*Sweeping of trapped flux in superconducting films by a micro-heat-flushing method*", Journal of Applied Physics **72** (6) , pp. 2411-2417, 1992

[11] J.R. Clem, "*Zero-quantum superconducting magnetic shielding apparatus and method*", IEEE Transactions on Magnetics **19** (3), pp. 1278-1281, 1983

[12] M. Dhalle, private communication

[13] J.D. Jackson, "*classical Electrodynamics*", Wiley, 1999

[14] J.R. Claycomb, J.H. Miller, Jr., "*Superconducting magnetic shields for SQUID applications*", Review of Scientific Instruments **70** (12), pp. 4562-4568 , 1990

[15] B.V. Vasil'ev, V.K. Ignatovich, E.V. Kolycheva, "*Shielding of weak magnetic fields by superconducting shells*", Sov Phys Tech Phys **23** (9), pp. 1100-1103, 1978

[16] J.N. Reddy, "An Introduction to the Finite Element Method", McGraw-Hill, 1984

[17] P. De Gennes, "*Superconductivity in metals and alloys*", Addison-Wesley Publishing, 1989

[18] B.M. Ayyub, R.H. McCuen, "*Numerical methods for engineers*", Prentice-Hall, 1996

[19] J.H. Ferziger, "*Numerical methods for engineering application*", John Wiley & Sons, 1998

[20] H.J.M. ter Brake, R. Houneker, H. Rogalla, "*New results in active noise compensation for magnetically shielded rooms*", Measurement Science and Technology **4** (12), pp. 1370-1375, 1993

[21] P. Ripka, "*Review of fluxgate sensors*", Sensors and actuators A **33** (3), pp. 129-141, 1992

[22] H.W. Weber, E. Seidl, C. Laa, E. Schachinger, M. Prohammer, A. Junod, D. Eckert, "*Anisotropy effects in superconducting niobium*", Physical Review B **44** (14), pp. 7585-7600, 1991

[23] M. Tinkman, "*Introduction to superconductivity*", second edition, McGraw-Hill, 1996

Appendix A: the magnetic field of an axially magnetized cylinder at z = 0

Here an analytical model for magnetic field inside and outside a magnetized cylinder in cylindrical coordinates is made.
This model is developed in cylindrical coordinates and in the horizontal symmetry plane, so that the vector potential **A** has only a z component. This means that $\boldsymbol{A}(r,\theta,z=0)=A_z(r,\theta)$. Implementing this into the vector potential equation (2) gives:

$$\boldsymbol{B}(r,\theta,z=0)=\nabla\times\mathbf{A}=\frac{1}{r}\frac{dA_z}{d\theta}\hat{r}-\frac{dA_z}{dr}\hat{\theta} \tag{A1}$$

This indicates that here there is no z component in the **B** field or z dependence in the centre of the shield. And using one of the Maxwell equations $\mu_0\boldsymbol{J}=\nabla\times\boldsymbol{B}$ (1a). Realizing that there is no current inside or outside the cylinder (so **J**=0 inside and outside the shield) gives:

$$\mu_0\boldsymbol{J}(r,\theta,z=0)=\nabla\times\boldsymbol{B}=\frac{1}{r}\left[\frac{d(rB_\theta)}{dr}-\frac{dB_r}{d\theta}\right]\hat{z}=0\ (inside\ or\ outside\ the\ shield) \tag{A2}$$

Now these two results are combined:

$$\rightarrow\frac{1}{r}\left[\frac{d(rB_\theta)}{dr}-\frac{dB_r}{d\theta}\right]=B_\theta+r\frac{dB_\theta}{dr}-\frac{dB_r}{d\theta}=-\frac{dA_z}{dr}-r\frac{d^2A_z}{dr^2}-\frac{1}{r}\frac{d^2A_z}{d\theta^2}=0 \tag{A3}$$

Now the separation of variables method is implemented ($A_z(r,\theta)=R(r)\Theta(\theta)$):

$$\rightarrow -R'\Theta-rR''\Theta-\frac{1}{r}\mathrm{R}\Theta''=0 \tag{A4}$$

Now multiplying the entire equation by $\frac{-r}{R\Theta}$:

$$\rightarrow r\frac{R'}{R}+r^2\frac{R''}{R}+\frac{\Theta''}{\Theta}=0 \tag{A5}$$

A separation constant of k is applied:

$$\rightarrow r\frac{R'}{R}+r^2\frac{R''}{R}=-\frac{\Theta''}{\Theta}=k^2 \tag{A6}$$

With this separation constant R and Θ can be written out separately:

$$\rightarrow r^2R''+rR'-k^2R \tag{A7a}$$

$$\rightarrow\Theta''+k^2\Theta \tag{A7b}$$

Luckily these differential equations (ODEs) have standard solutions, which are:

$$\Theta_{k=0}=A_0\theta+B_0\quad and\quad \Theta_{k\neq0}=A_k\cos[k(\theta-\varphi_k)] \tag{A8a}$$

$$\mathrm{R}_{k=0}=C_0\ln r+D_0\quad and\quad \mathrm{R}_{k\neq0}=C_kr^k+D_kr^{-k} \tag{A8b}$$

Now a general solution for A_z is made:

$$A_z(r,\theta)=(A_0\theta+B_0)(C_0\ln r+D_0)+\sum_{k=1}^{\infty}A_k\left(C_kr^k+D_kr^{-k}\right)\cos[k(\theta-\varphi_k)] \tag{A9}$$

With this and equation (2) a general solution for **B** is determined:

$$B_r(r,\theta,z=0) = \frac{A_0}{r}(C_0 \ln r + D_0) - \frac{1}{r}\sum_{k=1}^{\infty} A_k k\left(C_k r^k + D_k r^{-k}\right)\sin[k(\theta-\varphi_k)] \qquad \text{(A10a)}$$

$$B_\theta(r,\theta,z=0) = -(A_0\theta + B_0)\frac{C_0}{r} - \sum_{k=1}^{\infty} A_k\left(kC_k r^{k-1} - kD_k r^{-(k+1)}\right)\cos[k(\theta-\varphi_k)] \qquad \text{(A10b)}$$

Now these equations can be simplified using the definitions of $E_0 = -A_0C_0, F_0 = -A_0D_0, G_0 = -C_0B_0, E_k = -A_kkC_k, F_k = -A_kkD_k$, which leads to the final result of:

$$B_r(r,\theta,z=0) = \frac{-1}{r}(E_0 \ln r + F_0) + \sum_{k=1}^{\infty}\left(E_k r^{k-1} + F_k r^{-(k+1)}\right)\sin[k(\theta-\varphi_k)] \qquad \text{(19a)}$$

$$B_\theta(r,\theta,z=0) = (E_0\theta + G_0)\frac{1}{r} + \sum_{k=1}^{\infty}\left(E_k r^{k-1} - F_k r^{-(k+1)}\right)\cos[k(\theta-\varphi_k)] \qquad \text{(19b)}$$

Appendix B: quadrupole/dipole model current distribution on shield

Here the current distribution for a thin walled cylinder caused by remanence is determined.
First equations (19) are taken.

$$B_r(r,\theta,z=0) = \frac{-1}{r}(E_0 \ln r + F_0) + \sum_{k=1}^{\infty}\left(E_k r^{k-1} + F_k r^{-(k+1)}\right)\sin[k(\theta-\varphi_k)] \tag{19a}$$

$$B_\theta(r,\theta,z=0) = (E_0\theta + G_0)\frac{1}{r} + \sum_{k=1}^{\infty}\left(E_k r^{k-1} - F_k r^{-(k+1)}\right)\cos[k(\theta-\varphi_k)] \tag{19b}$$

In case of the shield a few boundary conditions need to be applied. The first one is that inside the shield the solution needs to remain finite when r→0, so this means that inside the shield E_0=F_0=G_0= 0 and F_k = 0 for all k:

$$B_{ri}(r,\theta,z=0) = \sum_{k=1}^{\infty} E_k r^{k-1}\sin[k(\theta-\varphi_k)] \tag{B1a}$$

$$B_{\theta i}(r,\theta,z=0) = \sum_{k=1}^{\infty} E_k r^{k-1}\cos[k(\theta-\varphi_k)] \tag{B1b}$$

The second boundary condition is that outside the shield at r→∞ the solution must also remain finite, so this means that outside the shield E_k = 0 for all k:

$$B_{ro}(r,\theta,z=0) = \frac{-1}{r}(E_0 \ln r + F_0) + \sum_{k=1}^{\infty} F_k r^{-(k+1)}\sin[k(\theta-\varphi_k)] \tag{B2a}$$

$$B_{\theta o}(r,\theta,z=0) = (E_0\theta + G_0)\frac{1}{r} - \sum_{k=1}^{\infty} F_k r^{-(k+1)}\cos[k(\theta-\varphi_k)] \tag{B2b}$$

From the measurements the radial field is taken at a distance of r=R_h. This results is in the form of a dipole and quadrupole combination, so the results will have an output like this:

$$B_{rfit}(r=R_h,\theta,z=0) = A_1\sin(\theta-\varphi_1) + A_2\sin[2(\theta-\varphi_2)] \tag{B3}$$

This can be implemented in the previous solution for inside the shield. This gives $E_1 = A_1, E_2 = \frac{A_2}{R_h}$ and E_k = 0 for k>2:

$$B_{ri}(r,\theta,z=0) = A_1\sin(\theta-\varphi_1) + A_2\frac{r}{R_h}\sin[2(\theta-\varphi_2)] \tag{B4a}$$

$$B_{\theta i}(r,\theta,z=0) = A_1\cos(\theta-\varphi_1) + A_2\frac{r}{R_h}\cos[2(\theta-\varphi_2)] \tag{B4b}$$

For this model the assumption is made that the shield is a thin-walled cylinder with radius r=R_s. With this assumption the equations for the inside of the shield can be connected to the equations for the outside of the shield. For the equations for the outside of the shield it results in $E_0 = F_0 = 0, F_1 = A_1 R_s^2, F_2 = A_2\frac{R_s^4}{R_h}$ and F_k= 0 for k>2:

$$B_{ro}(r,\theta,z=0) = A_1\left(\frac{R_s}{r}\right)^2\sin(\theta-\varphi_1) + A_2\frac{R_s}{R_h}\left(\frac{R_s}{r}\right)^3\sin[2(\theta-\varphi_2)] \tag{B5a}$$

$$B_{\theta o}(r,\theta,z=0) = \frac{G_0}{r} - A_1\left(\frac{R_s}{r}\right)^2\cos(\theta-\varphi_1) - A_2\frac{R_s}{R_h}\left(\frac{R_s}{r}\right)^3\cos[2(\theta-\varphi_2)] \tag{B5b}$$

Both these results can be combined together with equation (1a) to find the current distribution **J** in the θ-direction on the shield itself.

$$\mu_0 J(z = 0\theta, r = R_s) = \frac{G_0}{R_s} - 2A_1 \cos(\theta - \varphi_1) - 2A_2 \frac{R_s}{R_h} \cos[2(\theta - \varphi_2)] \qquad \text{(B6)}$$

G_0 should be zero else a net current will pass over the shield which is not assumed here, so the final result is:

$$\mu_0 J(\theta) = -2A_1 \cos(\theta - \varphi_1) - 2A_2 \frac{R_s}{R_h} \cos[2(\theta - \varphi_2)] \qquad (29)$$

Appendix C: complete derivation of the Ginzburg Landau energy equation

Here the Helmholtz free energy equation will be used to create the GL equations.
The derivation here is made with help from [8, chapter 6.2, 6.3].
First the Helmholtz free energy equation deep inside a superconductor with homogenous boundary conditions is:

$$F = F_n + a\psi^2 + \frac{1}{2}b\psi^4 \tag{C1}$$

This will be expanded to an expression of the free energy density at point **r**, which is then integrated over the volume to have the total energy. Since ψ depends on the position, a kinetic energy term would be expected in form of $E_k = \frac{1}{2m^*}|\hat{p}\psi|^2$. $\hat{p}$ is the momentum operator ($\hat{p} = -i\hbar\nabla$):

$$f(\boldsymbol{r}) = f_n + a|\psi|^2 + \frac{1}{2}b|\psi|^4 + \frac{\hbar^2}{2m^*}|\nabla\psi|^2 \tag{C2}$$

Also for this model a magnetic field is present. This will add two changes to the equation: first the momentum operator is modified to incorporate the presence of the magnetic field ($\hat{p} = -i\hbar\nabla - e^*\boldsymbol{A}$), Secondly the energy of an applied field will be added ($E_{mag} = \frac{\boldsymbol{B}^2}{2\mu_0} - \frac{\mu_0\boldsymbol{H}_0^2}{2}$):). This results in:

$$f(\boldsymbol{r}) = f_n + a|\psi|^2 + \frac{1}{2}b|\psi|^4 + \frac{1}{2m^*}|(-i\hbar\nabla - e^*\boldsymbol{A})\psi|^2 + \frac{\boldsymbol{B}^2}{2\mu_0} - \frac{\mu_0\boldsymbol{H}_0^2}{2} \tag{20}$$

B is the field created by the super currents and the $\mathbf{B}_0$ is the background field (constant).
Now to get the GL equations, the minimum Helmholtz energy is needed with respect to ψ and **A**. First we consider ψ, by taking the energy equations derivative to ψ. Since ψ is a complex function here it must be derived to either ψ or ψ^*. The one chosen is ψ^* and the derivative is written out below:

$$\frac{d}{d\psi^*}f(\boldsymbol{r}) = \frac{d}{d\psi^*}\left(f_n + a|\psi|^2 + \frac{1}{2}b|\psi|^4 + \frac{1}{2m^*}|(-i\hbar\nabla - e^*\boldsymbol{A})\psi|^2 + \frac{\boldsymbol{B}^2}{2\mu_0} - \frac{\mu_0\boldsymbol{H}_0^2}{2}\right) = 0 \tag{C3}$$

Now all the derivations are taken separately:

$$\rightarrow \frac{d}{d\psi^*}f_n + \frac{d}{d\psi^*}a|\psi|^2 + \frac{d}{d\psi^*}\frac{1}{2}b|\psi|^4 + \frac{d}{d\psi^*}\frac{1}{2m^*}|(-i\hbar\nabla - e^*\boldsymbol{A})\psi|^2 + \frac{d}{d\psi^*}\frac{\boldsymbol{B}^2}{2\mu_0} - \frac{d}{d\psi^*}\frac{\mu_0\boldsymbol{H}_0^2}{2}$$

$$= 0 + a\psi + b|\psi|^2\psi + \frac{1}{2m^*}|(-i\hbar\nabla - e^*\boldsymbol{A})|^2\psi + 0 - 0 \tag{C4}$$

This gives the final result of:

$$a\psi + b|\psi|^2\psi + \frac{1}{2m^*}|(-i\hbar\nabla - e^*\boldsymbol{A})|^2\psi = 0 \tag{21a}$$

Now the energy equation derivative is taken with respect to **A**:

$$\frac{d}{d\boldsymbol{A}} f(\boldsymbol{r}) = \frac{d}{d\boldsymbol{A}}\left(f_n + a|\psi|^2 + \frac{1}{2} b|\psi|^4 + \frac{1}{2m^*}|(-i\hbar\nabla - e^*\boldsymbol{A})\psi|^2 + \frac{\boldsymbol{B}^2}{2\mu_0} - \frac{\mu_0 \boldsymbol{H}_0^2}{2} \right) = 0 \qquad \text{(C5)}$$

Again the derivations are taken separately:

$$\begin{aligned} \rightarrow & \frac{d}{d\boldsymbol{A}} f_n + \frac{d}{d\boldsymbol{A}} a|\psi|^2 + \frac{d}{d\boldsymbol{A}} \frac{1}{2} b|\psi|^4 + \frac{d}{d\boldsymbol{A}} \frac{1}{2m^*}|(-i\hbar\nabla - e^*\boldsymbol{A})\psi|^2 + \frac{d}{d\boldsymbol{A}} \frac{\boldsymbol{B}^2}{2\mu_0} - \frac{d}{d\boldsymbol{A}} \frac{\mu_0 \boldsymbol{H}_0^2}{2} \\ & = 0 + 0 + 0 + \frac{d}{d\boldsymbol{A}}\left[\frac{1}{2m^*}(i\hbar\nabla - e^*\boldsymbol{A})\psi^*(-i\hbar\nabla - e^*\boldsymbol{A})\psi \right] + \frac{\boldsymbol{\nabla} \times \boldsymbol{B}}{\mu_0} - 0 \\ & = \frac{1}{2m^*}[-e^*\psi^*(-i\hbar\nabla - e^*\boldsymbol{A})\psi - e^*\psi(i\hbar\nabla - e^*\boldsymbol{A})\psi^*] + \frac{\boldsymbol{\nabla} \times \boldsymbol{B}}{\mu_0} \end{aligned} \qquad \text{(C6)}$$

Then the relation $\boldsymbol{J} = \frac{\boldsymbol{\nabla} \times \boldsymbol{B}}{\mu_0}$ is used and everything inside the brackets is written out.

$$= -\frac{e^*}{2m^*}[-\psi^* i\hbar\nabla\psi - e^*\boldsymbol{A}|\psi|^2 + \psi i\hbar\nabla\psi^* - e^*\boldsymbol{A}|\psi|^2] + \boldsymbol{J} = 0 \qquad \text{(C7)}$$

This gives the final result of:

$$\boldsymbol{J} = -\frac{e^* i\hbar}{2m^*}[\psi^*\nabla\psi - \psi\nabla\psi^*] - \frac{e^{*2}}{2m^*}\boldsymbol{A}|\psi|^2 \qquad \text{(21b)}$$

Appendix D: Ginzburg Landau equations rewritten with 1-dimensional wave function and vector potential

Here the GL equations for the 1-D wave function and vector potential used in the GL model are derived.
All the work done here is done with help from the books [7,17,23]
The equations and definitions below are the starting point:

$$a\psi + b|\psi|^2\psi + \frac{1}{2m^*}|(-i\hbar\nabla - e^*\boldsymbol{A})|^2\psi = 0 \tag{21a}$$

$$\boldsymbol{J} = -\frac{e^*i\hbar}{2m^*}[\psi^*\nabla\psi - \psi\nabla\psi^*] - \frac{e^{*2}}{2m^*}\boldsymbol{A}|\psi|^2 \tag{21b}$$

Together with the assumptions:

$$\boldsymbol{A} = A_y(x)\hat{y}$$

$$\psi(x,y) = \psi_\infty f(x)e^{i\theta(y)}\ , f = real\ part, \theta = phase, \psi_\infty = constant \tag{D1}$$

$$\mu_0\boldsymbol{J} = \nabla\times\boldsymbol{B} = \nabla\times\nabla\times\boldsymbol{A} \rightarrow \mu_0\boldsymbol{J} = -\nabla^2\boldsymbol{A}(x)$$

And the definitions:

$$\theta = ky, \frac{d^2\theta}{dy^2} = 0, \frac{d\theta}{dy} = k, \psi_\infty^2 = \frac{-a}{b}, \xi^2 = \frac{\hbar^2}{2m^*a}, \lambda^2 = \frac{m^*}{\mu_0 e^{*2}\psi_\infty^2}, \kappa = \frac{\lambda}{\xi}, \phi_0 = \frac{h}{e^*} \tag{D2}$$

The assumptions here are that the vector potential is only x dependent and in the y-direction ($\boldsymbol{A} = A_y(x)\hat{y}$) and the order parameter in the form of $\psi(x,y) = \psi_\infty f(x)e^{i\theta(y)}$ with f the real part of the ψ which is x dependent and θ as the phase which is linearly y dependent (θ=ky). Now the GL equations are written out with these assumptions separately.
First these assumptions are written in the first GL equation (21a):

$$\xrightarrow{(21a)} \frac{1}{2m^*}\left(i\hbar\nabla + e^*A_y(x)\hat{y}\right)^2\psi_\infty f(x)e^{i\theta(y)} + a\psi_\infty f(x)e^{i\theta(y)} + b\left|\psi_\infty f(x)e^{i\theta(y)}\right|^2\psi_\infty f(x)e^{i\theta(y)} = 0 \tag{D3}$$

The $\left(i\hbar\nabla + e^*A_y(x)\hat{y}\right)^2$ term will now written out but since A is only defined in the y direction and A depends only on x a $\nabla\cdot\left(A_y(x)\hat{y}\right) = \frac{dA_y(x)}{dy} = 0$. But ψ depends on y so when the wave function is present $\nabla\cdot\left(A_y(x)\hat{y}\right)$ can be written as $A_y(x)\frac{d}{dy}$. This leads to:

$$\rightarrow \frac{1}{2m^*}\left[-\hbar^2\nabla^2 + 2i\hbar e^*A_y(x)\frac{d}{dy} + \left(e^*A_y(x)\right)^2\right]\psi_\infty f(x)e^{i\theta(y)} + a\psi_\infty f(x)e^{i\theta(y)} + b|\psi_\infty f(x)|^2\psi_\infty f(x)e^{i\theta(y)} \tag{D4}$$

Now the function $\psi_\infty f(x)e^{i\theta(y)}$ is put into the differentiations:

$$= \frac{1}{2m^*}\left[-\hbar^2\nabla^2\left(\psi_\infty f(x)e^{i\theta(y)}\right) + 2i\hbar e^*A_y(x)\frac{d}{dy}\left(\psi_\infty f(x)e^{i\theta(y)}\right) + \left(e^*A_y(x)\right)^2\psi_\infty f(x)e^{i\theta(y)}\right] + a\psi_\infty f(x)e^{i\theta(y)} + b|\psi_\infty f(x)|^2\psi_\infty f(x)e^{i\theta(y)} \tag{D5}$$

The phase θ part of the wave function will have only y derivatives and the real part f will only have x derivatives. So now these functions can be written out:

$$= \frac{1}{2m^*}\left[-\hbar^2\left(e^{i\theta(y)}\frac{d^2\psi_\infty f(x)}{dx^2} + \psi_\infty f(x)\frac{d^2e^{i\theta(y)}}{dy^2}\right) - 2\hbar e^* A_y(x)\psi_\infty f(x)e^{i\theta(y)}\frac{d\theta(y)}{dy} + \left(e^* A_y(x)\right)^2\psi_\infty f(x)e^{i\theta(y)}\right] + a\psi_\infty f(x)e^{i\theta(y)} + b|\psi_\infty f(x)|^2\psi_\infty f(x)e^{i\theta(y)} \quad \text{(D6)}$$

Now the $\frac{d^2e^{i\theta(y)}}{dy^2}$ is written out:

$$= \frac{1}{2m^*}\left\{-\hbar^2\left[\frac{d^2\psi_\infty f(x)}{dx^2} - \psi_\infty f(x)\left(\frac{d\theta(y)}{dy}\right)^2 + i\psi_\infty f(x)\frac{d^2\theta(y)}{dy^2}\right]e^{i\theta(y)} - 2\hbar e^* A_y(x)\psi_\infty f(x)e^{i\theta(y)}\frac{d\theta(y)}{dy} + \left(e^* A_y(x)\right)^2\psi_\infty f(x)e^{i\theta(y)}\right\} + a\psi_\infty f(x)e^{i\theta(y)} + b|\psi_\infty f(x)|^2\psi_\infty f(x)e^{i\theta(y)} = 0 \quad \text{(D7)}$$

The $e^{i\theta(y)}$ parts can be taken out of entire equation which leads to the result below.

$$\rightarrow \frac{1}{2m^*}\left\{-\hbar^2\left[\frac{d^2(\psi_\infty f(x))}{dx^2} - \psi_\infty f(x)\left(\frac{d\theta(y)}{dy}\right)^2 + i\psi_\infty f(x)\frac{d^2\theta(y)}{dy^2}\right] - 2\hbar e^* A_y(x)\psi_\infty f(x)\frac{d\theta(y)}{dy} + \left(e^* A_y(x)\right)^2\psi_\infty f(x)\right\} + a\psi_\infty f(x) + b|\psi_\infty f(x)|^2\psi_\infty f(x) = 0 \quad \text{(D8)}$$

Using the assumptions for the phase ($\theta = ky, \frac{d^2\theta}{dy^2} = 0, \frac{d\theta}{dy} = k$):

$$\rightarrow \frac{1}{2m^*}\left\{-\hbar^2\left[\frac{d^2(\psi_\infty f)}{dx^2} - \psi_\infty f(k)^2 + i\psi_\infty f * 0\right] - 2\hbar e^* A_y\psi_\infty f\mathrm{k} + (e^* A)^2\psi_\infty f\right\} + a\psi_\infty f + b|\psi_\infty f|^2\psi_\infty f$$

$$= -\frac{\hbar^2}{2m^*}\frac{d^2(\psi_\infty f)}{dx^2} + \frac{\psi_\infty}{2m^*}(\hbar k - e^* A)^2 f + a\psi_\infty f + b|\psi_\infty f|^2\psi_\infty f = 0 \quad \text{(D9)}$$

Now the entire equation will be divided by parameter *a*:

$$\rightarrow -\frac{\hbar^2}{2m^* a}\frac{d^2(\psi_\infty f)}{dx^2} + \frac{1}{2m^* a}(\hbar k - e^* A)^2\psi_\infty f + \psi_\infty f + \frac{b}{a}|\psi_\infty f|^2\psi_\infty f \quad \text{(D10)}$$

$\hbar$ needs to be taken out of the brackets:

$$= -\frac{\hbar^2}{2m^* a}\frac{d^2(\psi_\infty f)}{dx^2} + \frac{\hbar^2}{2m^* a}\left(k - \frac{e^*}{\hbar}A\right)^2\psi_\infty f + \psi_\infty f + \frac{b}{a}|\psi_\infty f|^2\psi_\infty f \quad \text{(D11)}$$

Now using the definitions of $\psi_\infty^2 = \frac{-a}{b}, \xi^2 = \frac{\hbar^2}{2m^*|a|}, \phi_0 = \frac{h}{e^*}$ and the fact that the parameter *a* is negative so $|a| = -a$:

$$= \xi^2\frac{d^2(\psi_\infty f)}{dx^2} - \xi^2\left(k - \frac{2\pi}{\phi_0}A\right)^2\psi_\infty f + \psi_\infty f - \psi_\infty f^3 \quad \text{(D12)}$$

Now ξ is put back into the square giving the final result as:

$$\xi^2\frac{d^2(\psi_\infty f)}{dx^2} - \left(\xi k - \frac{2\pi\xi}{\phi_0}A\right)^2\psi_\infty f + \psi_\infty f - \psi_\infty f^3 = 0 \quad \text{(22a)}$$

Now the two assumptions ($\boldsymbol{A} = A_y(x)\hat{y}$ and $\psi(x,y) = \psi_\infty f(x) e^{i\theta(y)}$) are written into the second GL equation (21b).

$$\xrightarrow{21b} J = -\frac{i\hbar e^*}{2m^*}\left[\left(\psi_\infty f(x)e^{i\theta(y)}\right)^* \nabla\left(\psi_\infty f(x)e^{i\theta(y)}\right) - \psi_\infty f(x)e^{i\theta(y)}\nabla\left(\psi_\infty f(x)e^{i\theta(y)}\right)^*\right] - \frac{e^{*2}}{m^*}A_y(x)\left|\psi_\infty f(x)e^{i\theta(y)}\right|^2$$

$$= -\frac{i\hbar e^*}{2m^*}\left[\psi_\infty f(x)e^{-i\theta(y)}\nabla\left(\psi_\infty f(x)e^{i\theta(y)}\right) - \psi_\infty f(x)e^{i\theta(y)}\nabla\left(\psi_\infty f(x)e^{-i\theta(y)}\right)\right] - \frac{e^{*2}}{m^*}A_y(x)\left(\psi_\infty f(x)\right)^2 \quad \text{(D13)}$$

Again the differentiations are written out:

$$= -\frac{i\hbar e^*}{2m^*}\left[(\psi_\infty)^2 f(x)e^{-i\theta(y)}\left(\frac{df(x)}{dx} + if(x)\frac{d\theta(y)}{dy}\right)e^{i\theta(y)} - (\psi_\infty)^2 f(x)e^{i\theta(y)}\left(\frac{df(x)}{dx} - if(x)\frac{d\theta(y)}{dy}\right)e^{-i\theta(y)}\right] - \frac{e^{*2}}{m^*}A_y(x)(\psi_\infty f(x))^2 \quad \text{(D14)}$$

All the $e^{-i\theta(y)}$ and $e^{i\theta(y)}$ terms cancel each other out since $e^{-i\theta(y)} * e^{i\theta(y)} = 1$:

$$= -\frac{i\hbar e^*}{2m^*}\left[(\psi_\infty)^2 f(x)\left(\frac{df(x)}{dx} + if(x)\frac{d\theta(y)}{dy}\right) - (\psi_\infty)^2 f(x)\left(\frac{df(x)}{dx} - if(x)\frac{d\theta(y)}{dy}\right)\right] - \frac{e^{*2}}{m^*}A_y(x)\left(\psi_\infty f(x)\right)^2$$

$$= -\frac{i\hbar e^*}{2m^*}\left\{(\psi_\infty)^2 f(x)\left[\frac{df(x)}{dx} + if(x)\frac{d\theta(y)}{dy} - \frac{df(x)}{dx} + if(x)\frac{d\theta(y)}{dy}\right]\right\} - \frac{e^{*2}}{m^*}A_y(x)\left(\psi_\infty f(x)\right)^2 \quad \text{(D15)}$$

In the equation above it is visible that the $\frac{df(x)}{dx}$ terms will cancel each other out:

$$= -\frac{i\hbar e^*}{2m^*}\left[i(\psi_\infty)^2 f(x)^2\frac{d\theta(y)}{dy} + i(\psi_\infty)^2 f(x)^2\frac{d\theta(y)}{dy}\right] - \frac{e^{*2}}{m^*}A_y(x)(\psi_\infty f(x))^2 \quad \text{(D16)}$$

Now the $\psi_\infty f(x)$ term will be taken out of the brackets:

$$= \left[\frac{\hbar e^*}{2m^*}\left(\frac{d\theta(y)}{dy} + \frac{d\theta(y)}{dy}\right) - \frac{e^{*2}}{m^*}A_y(x)\right]\left(\psi_\infty f(x)\right)^2$$

$$= \left[\frac{\hbar e^*}{m^*}\frac{d\theta(y)}{dy} - \frac{e^{*2}}{m^*}A_y(x)\right]\left(\psi_\infty f(x)\right)^2 \quad \text{(D17)}$$

Using the equation $\mu_0 \boldsymbol{J} = -\nabla^2 \boldsymbol{A}(x)$ and implementing that into the left part of equation (21b) gives:

$$\xrightarrow{\mu_0 \boldsymbol{J} = -\nabla^2 \boldsymbol{A}(x)} -\frac{1}{\mu_0}\frac{d^2 A_y(x)}{dx^2} = \left[\frac{\hbar e^*}{m^*}\frac{d\theta(y)}{dy} - \frac{e^{*2}}{m^*}A_y(x)\right](\psi_\infty f(x))^2$$

$$\rightarrow \frac{d^2 A_y(x)}{dx^2} = \mu_0\left[\frac{e^{*2}}{m^*}A_y(x) - \frac{\hbar e^*}{m^*}\frac{d\theta(y)}{dy}\right](\psi_\infty f(x))^2 \quad \text{(D18)}$$

Again implementing the definition of $\frac{d\theta}{dy} = k$ and then bringing everything to the left side:

$$\rightarrow \frac{d^2 A}{dx^2} + \mu_0\psi_\infty^2\left[\frac{\hbar e^*}{m^*}k - \frac{e^{*2}}{m^*}A\right]f^2 = 0 \quad \text{(D19)}$$

Now getting the e^*, m^* and the $\hbar$ out of the brackets:

$$\rightarrow \frac{d^2 A}{dx^2} + \mu_0\psi_\infty^2\frac{e^*\hbar}{m^*}\left[k - \frac{e^*}{\hbar}A\right]f^2 \quad \text{(D20)}$$

Multiply the f^2 part by $\frac{\xi}{\xi}$:

$$= \frac{d^2A}{dx^2} + \mu_0\psi_\infty^2 \frac{e^*\hbar}{m^*}\frac{\xi}{\xi}\left[k - \frac{e^*}{\hbar}A\right]\left(\psi_\infty f(x)\right)^2 = \frac{d^2A}{dx^2} + \mu_0 \frac{e^*\hbar}{m^*}\frac{1}{\xi}\psi_\infty^2\left[\xi k - \xi\frac{e^*}{\hbar}A\right]f^2 \qquad \text{(D21)}$$

This is then rewritten using definitions of $\lambda^2 = \frac{m^*}{\mu_0 e^{*2}\psi_\infty^2}, \phi_0 = \frac{h}{e^*}$:

$$= \frac{d^2A}{dx^2} + \frac{\hbar}{e^*\lambda^2}\frac{1}{\xi}\left[\xi k - \frac{2\pi\xi}{\phi_0}A\right]f^2 = \frac{d^2A}{dx^2} + \frac{\phi_0}{2\pi\lambda^2}\frac{1}{\xi}\left[\xi k - \frac{2\pi\xi}{\phi_0}A\right]f^2 = 0 \qquad \text{(D22)}$$

Then bringing all the parameters to $\frac{d^2A}{dx^2}$ part:

$$\rightarrow \frac{2\pi\xi\lambda^2}{\phi_0}\frac{d^2A}{dx^2} + \left[\xi k - \frac{\xi}{\phi_0}A\right]f^2 = 0 \qquad \text{(D23)}$$

Finally using the definition $\kappa = \frac{\lambda}{\xi}$, this gives the final result of:

$$\frac{2\pi\xi(\kappa\xi)^2}{\phi_0}\frac{d^2A}{dx^2} + \left[\xi k - \frac{2\pi\xi}{\phi_0}A\right]f^2 = 0 \qquad \text{(22b)}$$

Appendix E: Ginzburg Landau equations with explicit temperature dependence

Here the GL equations are written out with a temperature dependence.
All the work here is done with help from the book [7].
For this model a temperature profile is added to the system. The temperature is taken to be T_0 at x=0 with $T_0<T_c$ and has a negative temperature gradient of $-\nabla T$. This gives a temperature profile of:

$$T(x) = T_0 - \nabla T x \tag{E1}$$

The temperature dependence of parameter *a* is known. This is in the form of:

$$a \propto \left(\frac{T}{T_c} - 1\right) \tag{E2}$$

This form was taken out of the book [7, ch.3]. Since ξ and ψ_{inf} are both depend on parameter *a* they are rewritten as:

$$\xi^2 = \frac{\hbar^2}{2m^*|a|} \propto \frac{1}{1-\frac{T}{T_c}} \tag{E3}$$

$$\psi_\infty^2 = \frac{-a}{b} \propto 1 - \frac{T}{T_c} \tag{E4}$$

To simplify further, the temperature profile (T(x)) is written out into ξ and ψ_{inf} with the definitions $t_0 \equiv \frac{T_0}{T_c}, \tau \equiv \frac{\nabla T}{T_c}\xi_0, u \equiv \frac{x}{\xi_0}$:

$$\xi^2 \propto \frac{1}{1-\frac{T_0-\nabla T x}{T_c}} = \frac{1}{1-\left(\frac{T_0}{T_c}-\frac{\nabla T}{T_c}x\right)} = \frac{1}{1-\frac{T_0}{T_c}+\frac{\nabla T}{T_c}x} = \frac{1}{1-\frac{T_0}{T_c}+\frac{\nabla T}{T_c}\frac{\xi_0}{\xi_0}x} = \frac{1}{1-t_0+\tau u} \tag{E5}$$

$$\psi_\infty^2 \propto 1-\frac{T_0-\nabla T x}{T_c} = 1-\left(\frac{T_0}{T_c}-\frac{\nabla T}{T_c}x\right) = 1-\frac{T_0}{T_c}+\frac{\nabla T}{T_c}x = 1-\frac{T_0}{T_c}+\frac{\nabla T}{T_c}\frac{\xi_0}{\xi_0}x = 1-t_0+\tau u \tag{E6}$$

Now the constant before the temperature dependence is taken to be the value at T=0. This results in:

$$\xi = \frac{\xi_0}{\sqrt{1-t_0+\tau u_0}} \tag{E7}$$

$$\psi_\infty = \psi_{\infty 0}\sqrt{1-t_0+\tau u_0} \tag{E8}$$

Now the GL equations (22a,b) will be rewritten using the new ξ and ψ_∞ which are now x dependent.
First equation (22a) will be rewritten with the new ξ and ψ_{∞}:

$$\xrightarrow{(22,a)} \xi^2\frac{d^2(\psi_\infty f)}{dx^2} - \left(\xi k - \frac{2\pi\xi}{\phi_0}A\right)^2\psi_\infty f + \psi_\infty f - \psi_\infty f^3 = 0 \tag{E9}$$

First $\frac{d^2(\psi_\infty f)}{dx^2}$ is written out:

$$\rightarrow \xi^2\left[\psi_\infty\frac{d^2 f}{dx^2} + 2\frac{d\psi_\infty}{dx}\frac{df}{dx} + \frac{d^2\psi_\infty}{dx^2}f\right] - \left(\xi k - \frac{2\pi\xi}{\phi_0}A\right)^2\psi_\infty f + \psi_\infty f - \psi_\infty f^3 \tag{E10}$$

The x dependent of ψ_{inf} will be written in with $\frac{d\psi_\infty}{dx} = \frac{1}{2}\frac{\psi_{\infty 0}}{\sqrt{1-t_0+\tau u}}\frac{\nabla T}{T_c}$, $\frac{d^2\psi_\infty}{dx^2} = -\frac{1}{4}\frac{\psi_{\infty 0}}{(1-t_0+\tau u)^{\frac{3}{2}}}\left(\frac{\nabla T}{T_c}\right)^2$:

$$
\begin{aligned}
&= \xi^2\left[\psi_{\infty 0}\sqrt{1-t_0+\tau u}\frac{d^2f}{dx^2} + 2\frac{1}{2}\frac{\psi_{\infty 0}}{\sqrt{1-t_0+\tau u}}\frac{\nabla T}{T_c}\frac{df}{dx} - \frac{1}{4}\frac{\psi_{\infty 0}}{(1-t_0+\tau u)^{\frac{3}{2}}}\left(\frac{\nabla T}{T_c}\right)^2 f\right] \\
&\quad - \left(\xi k - \frac{2\pi\xi}{\phi_0}A\right)^2 \psi_{\infty 0}\sqrt{1-t_0+\tau u}f + \psi_{\infty 0}\sqrt{1-t_0+\tau u}f \\
&\quad - \psi_{\infty 0}\sqrt{1-t_0+\tau u}f^3
\end{aligned}
\tag{E11}
$$

Now $\psi_{\infty 0}\sqrt{1-t_0+\tau u}$ is taken out of the brackets:

$$
\begin{aligned}
&= \xi^2\psi_{\infty 0}\sqrt{1-t_0+\tau u}\left[\frac{d^2f}{dx^2} + \frac{1}{1-t_0+\tau u}\frac{\nabla T}{T_c}\frac{df}{dx} - \frac{1}{4}\frac{1}{(1-t_0+\tau u)^2}\left(\frac{\nabla T}{T_c}\right)^2 f\right] \\
&\quad - \left(\xi k - \frac{2\pi\xi}{\phi_0}A\right)^2 \psi_{\infty 0}\sqrt{1-t_0+\tau u}f + \psi_{\infty 0}\sqrt{1-t_0+\tau u}f \\
&\quad - \psi_{\infty 0}\sqrt{1-t_0+\tau u}f^3
\end{aligned}
\tag{E12}
$$

and everything is divided by $\psi_{\infty 0}\sqrt{1-t_0+\tau u}$:

$$
= \xi^2\left[\frac{d^2f}{dx^2} + \frac{1}{1-t_0+\tau u}\frac{\nabla T}{T_c}\frac{df}{dx} - \frac{1}{4}\frac{1}{(1-t_0+\tau u)^2}\left(\frac{\nabla T}{T_c}\right)^2 f\right] - \left(\xi k - \frac{2\pi\xi}{\phi_0}A\right)^2 f + f - f^3 = 0 \tag{E13}
$$

Now the x dependence of $\xi = \frac{\xi_0}{\sqrt{1-t_0+\tau u}}$ will be written in:

$$
\begin{aligned}
&\rightarrow \left(\frac{\xi_0}{\sqrt{1-t_0+\tau u}}\right)^2\left[\frac{d^2f}{dx^2} + \frac{1}{1-t_0+\tau u}\frac{\nabla T}{T_c}\frac{df}{dx} - \frac{1}{4}\frac{1}{(1-t_0+\tau u)^2}\left(\frac{\nabla T}{T_c}\right)^2 f\right] \\
&\quad - \left(\frac{\xi_0}{\sqrt{1-t_0+\tau u}}k - \frac{2\pi}{\phi_0}\frac{\xi_0}{\sqrt{1-t_0+\tau u}}A\right)^2 f + f - f^3
\end{aligned}
\tag{E14}
$$

$\frac{1}{\sqrt{1-t_0+\tau u}}$ is taken out of the brackets:

$$
\begin{aligned}
&= \left(\frac{\xi_0}{\sqrt{1-t_0+\tau u}}\right)^2\left[\frac{d^2f}{dx^2} + \frac{1}{1-t_0+\tau u}\frac{\nabla T}{T_c}\frac{df}{dx} - \frac{1}{4}\frac{1}{(1-t_0+\tau u)^2}\left(\frac{\nabla T}{T_c}\right)^2 f\right] \\
&\quad - \left(\frac{1}{\sqrt{1-t_0+\tau u}}\right)^2\left(\xi_0 k - \frac{2\pi}{\phi_0}\xi_0 A\right)^2 f + f - f^3 \\
&= \frac{{\xi_0}^2}{1-t_0+\tau u}\left[\frac{d^2f}{dx^2} + \frac{1}{1-t_0+\tau u}\frac{\nabla T}{T_c}\frac{df}{dx} - \frac{1}{4}\frac{1}{(1-t_0+\tau u)^2}\left(\frac{\nabla T}{T_c}\right)^2 f\right] \\
&\quad - \frac{1}{1-t_0+\tau u}\left(\xi_0 k - \frac{2\pi}{\phi_0}\xi_0 A\right)^2 f + f - f^3 = 0
\end{aligned}
\tag{E15}
$$

Now everything is multiplied by $1 - t_0 + \tau u$:

$$\begin{aligned}\rightarrow {\xi_0}^2\left[\frac{d^2f}{dx^2} + \frac{1}{1-t_0+\tau u}\,\frac{\nabla T}{T_c}\frac{df}{dx} - \frac{1}{4}\frac{1}{(1-t_0+\tau u)^2}\left(\frac{\nabla T}{T_c}\right)^2 f\right] - \left(\xi_0 k - \frac{2\pi}{\phi_0}\xi_0 A\right)^2 f \\ + (1-t_0+\tau u)f - (1-t_0+\tau u)f^3 = 0\end{aligned}$$

$$\begin{aligned}\rightarrow {\xi_0}^2\frac{d^2f}{dx^2} - \left(\xi_0 k - \frac{2\pi}{\phi_0}\xi_0 A\right)^2 f + {\xi_0}^2\frac{1}{1-t_0+\tau u}\,\frac{\nabla T}{T_c}\frac{df}{dx} \\ - {\xi_0}^2 f\frac{1}{4}\frac{1}{(1-t_0+\tau u)^2}\left(\frac{\nabla T}{T_c}\right)^2 + (1-t_0+\tau u)(f-f^3) = 0\end{aligned} \tag{E16}$$

Then the definition $\tau = \frac{\nabla T}{T_c}\xi_0$ is implemented:

$$\begin{aligned}\rightarrow {\xi_0}^2\frac{d^2f}{dx^2} - \left(\xi_0 k - \frac{2\pi}{\phi_0}\xi_0 A\right)^2 f + \xi_0\frac{\tau}{1-t_0+\tau u}\,\frac{df}{dx} - f\frac{1}{4}\frac{(\tau)^2}{(1-t_0+\tau u)^2} \\ + (1-t_0+\tau u)(f-f^3) = 0\end{aligned} \tag{E17}$$

Now rewriting it as the old part with T_b=0 and $\nabla T = 0$ plus the part with τ and part with t_0:

$$\begin{aligned}{\xi_0}^2\frac{d^2f}{dx^2} - \left(\xi_0 k - \frac{2\pi}{\phi_0}\xi_0 A\right)^2 f + f - f^3 \\ + \tau\left[\xi_0\frac{1}{1-t_0+\tau u_0}\,\frac{df}{dx} - f\frac{1}{4}\frac{\tau}{(1-t_0+\tau u_0)^2} + u_0 f - u_0 f^3\right] - t_0[f-f^3] = 0\end{aligned} \tag{25a}$$

Also implementing the dimensionless variables $u \equiv \frac{x}{\xi_0}$, $\alpha_0 \equiv \xi_0 k - \frac{2\pi\xi_0}{\phi_0}A$ gives the final result of:

$$\begin{aligned}\frac{d^2f}{du^2} - {\alpha_0}^2 f + f - f^3 + \tau\left[\frac{1}{1-t_0+\tau u}\,\frac{df}{du} - f\frac{1}{4}\frac{\tau}{(1-t_0+\tau u)^2} + uf - uf^3\right] \\ - t_0[f-f^3] = 0\end{aligned} \tag{26a}$$

Now the same is done for equation (22,b):

$$\xrightarrow{(22,b)} \frac{2\pi\xi(\kappa\xi)^2}{\phi_0}\frac{d^2A}{dx^2} + \left[\xi k - \frac{2\pi\xi}{\phi_0}A\right]f^2 = 0 \qquad \text{(E18)}$$

First the x dependent form ξ is written in:

$$\rightarrow \frac{2\pi\kappa^2}{\phi_0}\left(\frac{\xi_0}{\sqrt{1-t_0+\tau u}}\right)^3\frac{d^2A}{dx^2} + \left[\frac{\xi_0}{\sqrt{1-t_0+\tau u}}k - \frac{2\pi}{\phi_0}\frac{\xi_0}{\sqrt{1-t_0+\tau u}}A\right]f^2 \qquad \text{(E19)}$$

Now $\frac{1}{\sqrt{1-t_0+\tau u}}$ is taken out of the brackets:

$$= \frac{2\pi\kappa^2}{\phi_0}\left(\frac{\xi_0}{\sqrt{1-t_0+\tau u}}\right)^3\frac{d^2A}{dx^2} + \frac{1}{\sqrt{1-t_0+\tau u}}\left[\xi_0 k - \frac{2\pi\xi_0}{\phi_0}A\right]f^2 = 0 \qquad \text{(E20)}$$

The entire function is multiplied by $\sqrt{1-t_0+\tau u}$:

$$\rightarrow \sqrt{1-t_0+\tau u}\left\{\frac{2\pi\kappa^2}{\phi_0}\left(\frac{\xi_0}{\sqrt{1-t_0+\tau u}}\right)^3\frac{d^2A}{dx^2} + \frac{1}{\sqrt{1-t_0+\tau u}}\left[\xi_0 k - \frac{2\pi\xi_0}{\phi_0}A\right]f^2\right\} = 0$$

$$\rightarrow \frac{2\pi\kappa^2{\xi_0}^3}{\phi_0}\left(\frac{1}{\sqrt{1-t_0+\tau u}}\right)^2\frac{d^2A}{dx^2} + \left[\xi_0 k - \frac{2\pi\xi_0}{\phi_0}A\right]f^2$$

$$= \frac{2\pi\kappa^2{\xi_0}^3}{\phi_0}\frac{1}{1-t_0+\tau u}\frac{d^2A}{dx^2} + \left[\xi_0 k - \frac{2\pi\xi_0}{\phi_0}A\right]f^2 \qquad \text{(E21)}$$

This is multiplied by $1 - t_0 + \tau u$:

$$= \frac{2\pi\kappa^2{\xi_0}^3}{\phi_0}\frac{d^2A}{dx^2} + [1-t_0+\tau u]\left[\xi_0 k - \frac{2\pi\xi_0}{\phi_0}A\right]f^2 = 0 \qquad \text{(E22)}$$

Now again rewriting it as the old part with T_0=0 and $\nabla T = 0$ plus the part with τ and part with t_0:

$$\frac{2\pi\kappa^2{\xi_0}^3}{\phi_0}\frac{d^2A}{dx^2} + \left[\xi_0 k - \frac{2\pi\xi_0}{\phi_0}A\right]f^2 + \tau u_0\left[\xi_0 k - \frac{2\pi\xi_0}{\phi_0}A\right]f^2 - t_0\left[\xi_0 k - \frac{2\pi\xi_0}{\phi_0}A\right]f^2 = 0 \qquad \text{(25b)}$$

Implementing the dimensionless variables $u \equiv \frac{x}{\xi_0}, \alpha_0 \equiv \xi_0 k - \frac{2\pi\xi_0}{\phi_0}A$ gives the final result of:

$$-\kappa^2\frac{d^2\alpha_0}{du^2} + \alpha_0 f^2 + \tau u\alpha_0 f^2 - t_0\alpha_0 f^2 = 0 \qquad \text{(26b)}$$

Appendix F: numerical iteration method to solve the 1D Ginzburg Landau equations

The numerical technique used is of own design and is described here.
First an integral is taken from 0 to ∞ of the derivative of f:

$$\int_0^\infty f'(u')du' = f(\infty) - f(0) \tag{F1}$$

Now either point (0 or ∞) can be changed to variable u and the theory will still apply. In this cause f(∞) (f(∞)=1) is known so 0 is changed into u. This results in:

$$f(u) = f(\infty) - \int_u^\infty f'(u')du' = 1 - \int_u^\infty f'(u')du' \tag{F2}$$

The integral is then written numerically:

$$f_i = 1 - \sum_{j=i}^{N} f'_j \Delta u \tag{F3}$$

The same trick can be applied to the second derivative of f only now f'(0) (f'(0)=b) is known so ∞ is changed into u. This results in:

$$\int_0^\infty f''(u')du' = f'(\infty) - f'(0) \to f'(u) = f'(0) + \int_0^u f''(u')du' \to f'_i = b + \sum_{j=0}^{i} f''_j \Delta u \tag{F4}$$

Since the second derivative of f is known from the first Ginzburg Landau equation (equations (26a)) it will be implemented:

$$\begin{aligned} f_i^{p+1\prime} = b + \sum_{j=0}^{i} \Bigg[& \left(\alpha_j^p\right)^2 f_j^p - f_j^p + \left(f_j^p\right)^3 \\ & - \tau \left[\frac{1}{1 - t_0 + \tau u_j} \frac{df_j^p}{du_j} - f_j^p \frac{1}{4} \frac{\tau}{\left(1 - t_0 + \tau u_j\right)^2} + u_j f_j^p - u_j \left(f_j^p\right)^3 \right] \\ & + t_0 \left\{ f_j^p - \left(f_j^p\right)^3 \right\} \Bigg] \Delta u \end{aligned} \tag{27a}$$

$$f_i^{p+1} = 1 - \sum_{j=i}^{N} f_j^{p+1\prime} \Delta u \tag{27b}$$

With this, a solution f for the GL equation can be found. This is done by implementing an initial starting guess for f (f^p) and using the equations above to calculate a new function for f (f^{p+1}). Only an initial function for f needs to be known. This is taken to have the form of f as seen in Figure 2.6.

Now this same trick will be done for α with the known boundaries of α(∞) (α(∞)=0) and α'(0) (α'(0)=β_0):

$$\int_0^\infty \alpha'(u')du' = \alpha(\infty) - \alpha(0) \to \alpha(u) = \alpha(\infty) - \int_u^\infty \alpha'(u')du' \to \alpha_i = 0 - \sum_{j=i}^{N} \alpha'_j \Delta u \tag{F5}$$

$$\int_0^\infty \alpha''(u')du' = \alpha'(\infty) - \alpha'(0) \to \alpha'(u) = \alpha'(0) + \int_0^u \alpha''(u')du' \to \alpha'_i = \beta_0 + \sum_{j=0}^{i} \alpha''_j \Delta u \tag{F6}$$

Now the second GL equation (equation (26b)) is implemented:

$$\alpha_i^{p+1\prime} = \beta_0 + \frac{1}{\kappa^2}\sum_{j=0}^{i}\left[\alpha_j^p\left(f_j^p\right)^2 + \tau u_j \alpha_j^p\left(f_j^p\right)^2 - t_0\alpha_j^p\left(f_j^p\right)^2\right]\Delta u \tag{28a}$$

$$\alpha_i^{p+1} = -\sum_{j=i}^{N}\alpha_j^{p+1\prime}\Delta u \tag{28b}$$

Again the form of the initial function for α can be found in Figure 2.6.